Wind Estimation and Control of Unmanned Aerial Vehicles with Application to Forest Fire Surveillance

Zhewen Xing

A Thesis
in The Department
of
Mechanical, Industrial and Aerospace Engineering

Presented in Partial Fulfillment of the Requirements
for the Degree of
Doctor of Philosophy (Mechanical Engineering) at
Concordia University
Montréal, Québec, Canada

February 2023

CONCORDIA UNIVERSITY

SCHOOL OF GRADUATE STUDIES

This is to certify that the thesis prepared
By: **Zhewen Xing**
Entitled: **Wind Estimation and Control of Unmanned Aerial Vehicles with Application to Forest Fire Surveillance**

and submitted in partial fulfillment of the requirements for the degree of

Doctor of Philosophy (Mechanical Engineering)

complies with the regulations of this University and meets the accepted standards with respect to originality and quality.
Signed by the Final Examining Committee:

Dr. Andrea Schiffauerova	Chair
Dr. Yang Shi	External Examiner
Dr. Jun Yan	Examiner
Dr. Subhash Rakheja	Examiner
Dr. Wen-Fang Xie	Examiner
Dr. Youmin Zhang	Co-supervisor
Dr. Chun-Yi Su	Co-supervisor

Approved by
Dr. Muthukumaran Packirisamy, Graduate Program Director

January 9, 2023
Date of Defense

Dr. Mourad Debbabi, Dean, Gina Cody School of Engineering and Computer Science

Abstract

Wind Estimation and Control of Unmanned Aerial Vehicles with Application to Forest Fire Surveillance

Zhewen Xing, Ph.D.

Concordia University, 2023

In recent years, there has been an increasing interest in the application of unmanned aerial vehicles in forest fire monitoring and detection systems. Armed with unmanned aerial vehicles (UAVs), firefighters on the ground can get a bird's-eye view of the terrain, respond to forest fires quickly, distribute resources, and ultimately save lives and properties. In practice, wind behaviors have significant impacts on both the performance of UAV and forest fire situations. However, current wind measurement and estimation relies on data gathered from ground weather stations that are often located several kilometers away from the forest fire regions. As a result, it is challenging to maintain the performance and assess the forest fire situations properly with the obtained wind information.

This thesis investigates the problems of the wind estimation and control of unmanned aerial vehicles with application to forest fire surveillance. To develop UAVs as remote wind sensing platforms, a two-stage particle filter-based approach is proposed to estimate winds from quadrotor motion. Based on the estimated wind information, an active wind rejection control strategy is designed to maintain the performance of a quadrotor UAV in the presence of unknown winds. Then, the active wind rejection control strategy is developed for the formation control of multiple UAVs to ensure their cooperative tracking capability. Finally, based on the wind data and fire observations collected by UAVs, a forest fire monitoring scheme is designed to accurately estimate the situation of wind-affected forest fires.

Acknowledgments

This thesis is submitted in partial fulfillment of the requirements for the degree of philosophy doctor at Concordia University under the financial support of Chinese Scholarship Council and Concordia University. The presented research has been conducted under the supervision of Prof. Youmin Zhang and Prof. Chun-Yi Su at the Department of Mechanical, Industrial & Aerospace Engineering, Concordia University.

First of all, I would like to express my sincere gratitude and appreciation to my supervisors, Prof. Youmin Zhang and Prof. Chun-Yi Su for their kind advice, ongoing support, and encouragement throughout my doctoral study. My research would likely progress slowly and unsatisfactorily without their persistent support, wonderful assistance, and insightful guidance. Their passion, meticulosity, diligence and wisdom always inspire me and these are the great gifts for me to take into my life.

Second, I would like to express my gratitude to all of the research team members and collaborators who supported me much throughout my doctoral studies. It is my great pleasure to do research and share ideas with them and learn from them.

Last but not least, I would like to send my deepest gratitude and appreciation to my parents for love, understanding, consistent support, and countless sacrifices, which have played an indispensable role in my life. It can never be enough for me to thank them.

Contents

List of Figures ix

List of Tables xiii

Nomenclature and Acronyms xiv

1 Introduction 1

- 1.1 Background . . . 1
  - 1.1.1 Guidance, Navigation and Control of UAV . . . 1
  - 1.1.2 Role of UAV in Fighting Forest Fire . . . 3
- 1.2 Review of Related Works . . . 5
  - 1.2.1 Wind Measurement and Estimation Approaches for UAVs . . . 5
  - 1.2.2 Control of UAVs Against Wind Disturbances . . . 8
  - 1.2.3 Forest Fire Monitoring Approaches . . . 10
- 1.3 Objectives of This Thesis . . . 12
- 1.4 Contributions of This Thesis . . . 12
- 1.5 Organization of This Thesis . . . 14

2 Preliminaries 16

- 2.1 Quadrotor UAV Model . . . 16
  - 2.1.1 Newton-Euler Dynamic Model . . . 18

2.1.2 Wind Effects on Quadrotor UAV 21

2.1.3 Simplified Dynamic Model 23

2.2 Forest Fire Spread Model 25

2.2.1 One-dimensional Rothermel Model 25

2.2.2 Extension to Two-dimensional Surfaces 26

2.3 Wind Models 28

2.3.1 Constant Wind 28

2.3.2 Wind Gust 29

2.3.3 Wind Turbulence 29

2.3.4 Log Wind Profile 30

2.4 Summary 31

3 Two-Stage Particle Filter-based Wind Estimation from Quadrotor Motion 32

3.1 Problem Formulation 32

3.2 General Particle Filter 34

3.3 Wind Estimation Framework 36

3.4 Two-Stage Particle Filter-based Wind Estimation 38

3.4.1 Discrete-Time Model of a Quadrotor UAV 38

3.4.2 Two-Stage Particle Filter Design 39

3.5 Simulation Results 44

3.5.1 Estimation of Constant Wind from Quadrotor Motion 45

3.5.2 Estimation of Wind Gust from Quadrotor Motion 46

3.5.3 Estimation of Wind Turbulence from Quadrotor Motion 51

3.6 Summary 53

4 Active Wind Rejection Control of Quadrotor UAVs 54

4.1 Problem Formulation 54

4.2 Sliding Mode Control 55

4.3 Active Wind Rejection Control of a Quadrotor UAV 57

4.3.1 Outer-loop Control 58

4.3.2 Inner-loop Control 65

4.4 Active Wind Rejection Cooperative Control of Multiple Quadrotor UAVs . 68

4.4.1 Basic Graph Theory 69

4.4.2 Cooperative Controller Design 70

4.5 Simulation Results 73

4.5.1 Control of a Single Quadrotor UAV in the Presence of Wind 74

4.5.2 Formation Control of Multiple Quadrotor UAVs in the Presence of Wind 84

4.6 Summary 92

5 Forest Fire Monitoring with a System of UAVs under Effect of Wind 94

5.1 Problem Formulation 94

5.2 Wind-affected Forest Fire Monitoring Strategy Design 95

5.2.1 Local Wind Field Reconstruction 96

5.2.2 Optimal Wind Sensing Locations 99

5.2.3 Forest Fire Monitoring Scheme Based on Ensemble Kalman Filter . 101

5.3 Simulation Results 104

5.3.1 Forest Fire Monitoring with Regional Wind Field Estimation 105

5.3.2 Forest Fire Monitoring with Specific Focus on the Fire Front 109

5.4 Summary 112

6 Conclusions and Future Works 113

6.1 Conclusions 113

6.2 Future Works 114

Bibliography **116**

List of Figures

Figure 1.1 General structure of UAV guidance, navigation and control system [1] 2

Figure 1.2 Forest area burned and number of forest fire in Canada, 2012-2022 [2] 3

Figure 1.3 Role of UAV in three stages of fighting forest fires 4

Figure 2.1 Reference frames and the quadrotor UAV configuration 16

Figure 2.2 Maneuver schemes of a quadrotor UAV 17

Figure 2.3 Wind triangle relationship between quadrotor ground speed vector, airspeed vector and wind vector 21

Figure 2.4 Elliptical fire spread model 27

Figure 3.1 Framework of the proposed TSPF scheme for the state and wind estimation from quadrotor motion 36

Figure 3.2 Structure of the two-stage particle filter 40

Figure 3.3 Estimation results of a constant wind of $[3,\ 4,\ 0]^T\ \mathrm{m/s}$ from a quadrotor UAV in hover 47

Figure 3.4 Estimation results of a slowly-changing wind gust from a quadrotor UAV in hover 49

Figure 3.5 Estimation results of a quickly-changing wind gust from a quadrotor UAV in hover 50

Figure 3.6 Estimation results of a $[3,\ 4,\ 0]^T\ \mathrm{m/s}$ mean Dryden turbulence with $\sigma_{u,v,w} = [1.54,\ 1.54,\ 0.97]^T$ from a quadrotor UAV in hover 52

Figure 4.1 Framework of the proposed wind rejection control strategy of a quadrotor UAV 57
Figure 4.2 Framework of the proposed wind rejection cooperative control strategy of multiple quadrotor UAVs 69
Figure 4.3 Generated continuous wind 75
Figure 4.4 Hovering performances of a quadrotor UAV under the continuous wind 76
Figure 4.5 Thrusts of a quadrotor UAV for hovering under the continuous wind 76
Figure 4.6 Wind and drag coefficient estimation of a quadrotor UAV for hovering under the continuous wind 77
Figure 4.7 Generated wind gust 78
Figure 4.8 Hovering performances of a quadrotor UAV under the gust wind . . 79
Figure 4.9 Thrusts of a quadrotor UAV for hovering under the gust wind 79
Figure 4.10 Wind and drag coefficient estimation of a quadrotor UAV for hovering under the gust wind 80
Figure 4.11 Performance of the proposed adaptive drag coefficient control under the gust wind 81
Figure 4.12 Trajectory tracking performances of a quadrotor UAV under the continuous wind 82
Figure 4.13 Thrusts of a quadrotor UAV for trajectory tracking under the continuous wind 83
Figure 4.14 Wind and drag coefficient estimation of a quadrotor UAV for trajectory tracking under the continuous wind 83
Figure 4.15 Trajectory tracking errors of a quadrotor UAV under the continuous wind 84
Figure 4.16 Communication network of quadrotor UAVs 85

Figure 4.17 Generated wind gusts acting on multiple quadrotor UAVs 86
Figure 4.18 x positions of multiple quadrotor UAVs under the wind gusts 87
Figure 4.19 y positions of multiple quadrotor UAVs under the wind gusts 87
Figure 4.20 z positions of multiple quadrotor UAVs under the wind gusts 88
Figure 4.21 Adaptive wind effect compensation inputs under the wind gusts . . . 88
Figure 4.22 Thrusts of the active wind rejection formation control under the wind gusts 89
Figure 4.23 Generated continuous winds acting on multiple quadrotor UAVs . . 90
Figure 4.24 x positions of multiple quadrotor UAVs under the continuous winds 90
Figure 4.25 y positions of multiple quadrotor UAVs under the continuous winds . 91
Figure 4.26 z positions of multiple quadrotor UAVs under the continuous winds . 91
Figure 4.27 Adaptive wind effect compensation inputs under the continuous winds 92
Figure 4.28 Thrusts of the active wind rejection formation control under the continuous winds 93
Figure 5.1 Framework of the proposed forest fire monitoring strategy 95
Figure 5.2 Framework of the GPR-based wind field reconstruction approach . . 97
Figure 5.3 Illustration of forest fire spread in the self-defined wind field 105
Figure 5.4 Actual wind field with target locations 106
Figure 5.5 Predicted mean wind field with different numbers of wind measurements 106
Figure 5.6 Prediction of forest fire spread at $t = 60\,\mathrm{s}$ 107
Figure 5.7 Estimation of forest fire spread with EnKF at $t = 60\,\mathrm{s}$ 108
Figure 5.8 Comparison of forest fire spread prediction and estimation 108
Figure 5.9 Wind field and forest fire estimation with specific focus on the fire front at $t = 0\,\mathrm{s}$ 109

Figure 5.10 Wind field and forest fire estimation with specific focus on the fire front at $t = 20\,\mathrm{s}$ 109
Figure 5.11 Wind field and forest fire estimation with specific focus on the fire front at $t = 40\,\mathrm{s}$ 110
Figure 5.12 Wind field and forest fire estimation with specific focus on the fire front at $t = 60\,\mathrm{s}$ 110
Figure 5.13 Comparison of forest fire estimation with regional wind field and specific focus on the fire front 111

List of Tables

Table 2.1 Parameters of the quadrotor dynamic model 24
Table 2.2 Variance of process noise 24
Table 2.3 Variance of measurement noise 24
Table 2.4 Parameters of the fire spread model 26
Table 3.1 Comparison of MAE and RMSE for constant wind estimation from a quadrotor UAV in hover 46
Table 3.2 Wind gust scenarios in the simulation 48
Table 3.3 Comparison of MAE and RMSE for a $[3,\ 4,\ 0]^T\ \mathrm{m/s}$ mean Dryden turbulence estimation from a quadrotor UAV in hover 51
Table 3.4 Comparison of MAE and RMSE for a $[3,\ 4,\ 0]^T\ \mathrm{m/s}$ mean Dryden turbulence estimation from a quadrotor UAV in hover under different SNRs 53
Table 4.1 Parameters of the active wind rejection controller 74

Acronyms and Nomenclature

Acronyms

EnKF	Ensemble Kalman filter
GNC	Guidance, navigation and control
GP	Gaussian process
GPR	Gaussian process regression
GPS	Global positioning system
IMU	Inertial measurement unit
LSTM	Long short-term memory
NTSMC	Nonsingular terminal sliding mode control
QUAV	Quadrotor unmanned aerial vehicle
SMC	Sliding mode control
SPE	State and parameter estimation
TSPF	Two-stage particle filter
UAV	Unmanned aerial vehicle

WT	Wind triangle

Nomenclature

β	Packing ratio of the fuel bed
$\boldsymbol{\xi}$	Wind vector
$\boldsymbol{\xi}^f$	Wind vector induced the fire spread
$\boldsymbol{V}_a$	Airspeed vector of QUAV
$\boldsymbol{V}_g$	Ground speed vector of QUAV
$\boldsymbol{V}_w$	Wind speed vector of QUAV
$\boldsymbol{x}$	State vector of QUAV
$\boldsymbol{x}^f$	State vector of forest fire
$\boldsymbol{z}$	Measurement vector of QUAV
$\boldsymbol{z}^f$	Observation vector of forest fire
$\dot{x}$	Linear velocity of QUAV along x_g-axis
$\dot{y}$	Linear velocity of QUAV along y_g-axis
$\dot{z}$	Linear velocity of QUAV along z_g-axis
$\hat{\boldsymbol{\xi}}$	Estimated wind vector
$\hat{\boldsymbol{x}}$	Estimated state vector of QUAV
ϕ	Roll angle of QUAV
Φ_w	Wind coefficient

ψ	Yaw angle of QUAV
σ	Surface area-to-volume ratio
τ_ϕ	Roll moment of QUAV
τ_ψ	Yaw moment of QUAV
τ_θ	Pitch moment of QUAV
θ	Pitch angle of QUAV
φ_w	Azimuth angle of wind direction
ξ_x	Wind component along x_g-axis
ξ_y	Wind component along y_g-axis
ξ_z	Wind component along z_g-axis
C_{dxy}	Lateral drag coefficient
C_{dz}	Vertical drag coefficient
F_z	Throttle of QUAV
F_{dx}	Drag force along x_g-axis
F_{dy}	Drag force along y_g-axis
F_{dz}	Drag force along z_g-axis
h_f	Fuel height
I_x	Inertial moment of QUAV along x_b-axis
I_x	Inertial moment of QUAV along z_b-axis

I_y	Inertial moment of QUAV along y_b-axis
k_m	Thrust-to-moment coefficient
l	Arm length of QUAV
m	Mass of QUAV
p	Angular velocity of QUAV along x_b-axis
q	Angular velocity of QUAV along y_b-axis
R	Fire spread rate
r	Angular velocity of QUAV along z_b-axis
R_0	No-wind, no-slope fire spread rate
T_i	Thrust of rotor i
u	Linear velocity of QUAV along x_b-axis
U_0	Wind speed at altitude of $6.1\,\mathrm{m}$ above the vegetation top
U_f	Mid-flame wind speed
v	Linear velocity of QUAV along y_b-axis
w	Linear velocity of QUAV along z_b-axis
x	Position of QUAV along x_g-axis
y	Position of QUAV along y_g-axis
z	Position of QUAV along z_g-axis

Chapter 1

Introduction

1.1 Background

1.1.1 Guidance, Navigation and Control of UAV

Unmanned aerial vehicle techniques have seen explosive growth over the past few decades. UAVs are classified based on weight, flying height, wing type, endurance and range, which support wide varieties of applications. These applications cover a large number of fields, such as forest fire monitoring, aerial photography, payload delivery, agriculture, infrastructure inspection, policing and surveillance. The reliability and safety of UAVs are increasingly required for these practical applications because UAVs are often used to execute specific tasks in complex and hazardous environments.

For the autonomous operation of UAVs, *guidance, navigation and control* are three essential components that constitute the general structure of the UAV system, as demonstrated in Fig. 1.1. These subsystems are devoted to the safe, reliable, and efficient performance of the whole UAV system. The functions of these three subsystems are briefly discussed as follows.

(1) *Guidance subsystem* is responsible for the generation of desired trajectories for the

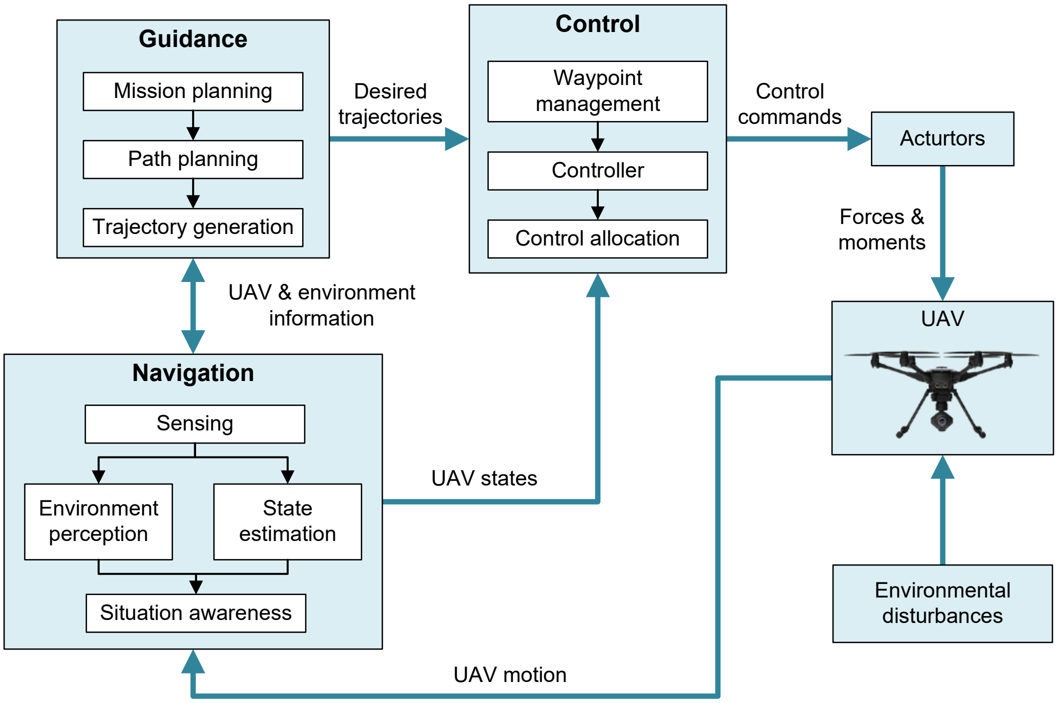

Figure 1.1: General structure of UAV guidance, navigation and control system [1]

control subsystem based on the information of UAV and environment obtained from the navigation subsystem. To accomplish assigned tasks with the considerations of targets, environment, operators, UAV cooperation, available power, etc., optimal trajectories, as well as desired changes of velocities and attitudes to follow those paths, are generated for the UAV in this subsystem.

(2) *Navigation subsystem* is responsible for the identification of current UAV states and its surrounding environment information for the guidance and control subsystems. UAV states, including position, velocity, attitude, and angular velocity can be measured or estimated with onboard sensors such as the GPS and IMU modules. In addition, the environment perception is an important aspect. For example, changes of wind speed and direction can be measured from wind sensors or estimated from UAV motion.

(3) *Control subsystem* is responsible for the determination of control commands to stabilize the vehicle and track the desired trajectories generated by the guidance subsystem. To accomplish the trajectory tracking control of a UAV, a set of waypoints are extracted from the desired trajectories. The designed controller yields appropriate control commands and allocates them to each control surface of the UAV, including the thrust, rudder, elevator, aileron, etc., to traverse all waypoints.

	Area burned	Number of fires
2012	1,928,138	7,337
2013	3,798,229	5,900
2014	4,607,677	4,883
2015	3,969,536	6,773
2016	1,400,627	5,026
2017	3,456,768	5,305
2018	2,266,587	6,845
2019	1,838,960	4,258
2020	229,271	3,928
2021	4,299,453	6,525
2022	1,093,888	3,110

1.1.2 Role of UAV in Fighting Forest Fire

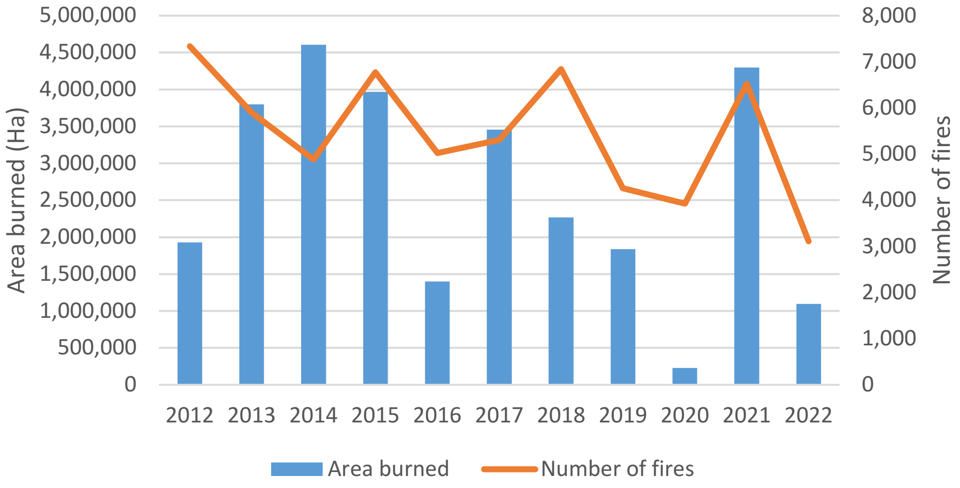

Figure 1.2: Forest area burned and number of forest fire in Canada, 2012-2022 [2]

Over the past few decades, increasing global temperatures and more prolonged and severe droughts have contributed to the favorable conditions of forest fires [3, 4]. These forest fires resulted in irreparable environmental damages and unquantifiable economic losses, which had detrimental impacts on ecosystem services, public health, and economic activities. Fig. 1.2 shows a statistic result of burned forest area and the number of forest fires in Canada from 2012 to 2022 (to date). In Canada, about 7300 forest fires have occurred and burned about 2.5 million hectares of forests annually over the last 25 years [5]. In addition, recent extreme forest fires in Brazil, Australia, and California in USA have once again attracted public attention to the issue of forest fires.

Autonomous UAVs are playing an important role in fighting forest fires due to their low cost and high flexibility. UAVs can be deployed to improve the situation awareness by the ground team and share important data with the air and ground crews that can help ground teams detect potential risks and put out the fire rapidly. Fig. 1.3 indicates the role of UAV in three stages of fighting forest fires.

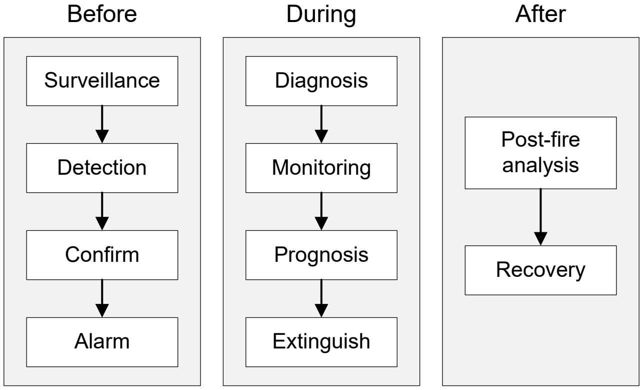

Figure 1.3: Role of UAV in three stages of fighting forest fires

(1) *Before*: UAVs can be deployed to minimize the cause of forest fires for prevention. Patrolling high-risk regions of potential fires by ground crews is usually dangerous, time-consuming, and inefficient because of inadequate infrastructures and rough terrains. Fixed-wing UAVs can traverse a long distance to continuously observe over a large area of forest in order to find the potential occurrences of fires, while rotary-wing UAVs can quickly provide close site-detection to confirm these hot spots. When occurrences of these fires are confirmed, UAVs can quickly alert the ground team about the emergence of forest fires.

(2) *During*: UAVs can be applied for a fast response to forest fires in order to minimize adverse consequences. UAVs can locate fire sources and diagnose the extent of fire in the air when thick smoke makes it nearly impossible for visual cameras to see the

source and scope of the growing fires from the ground, continuously monitor theses fires and its surroundings with onboard cameras and other sensors, and predict the speed and direction of forest fire propagation in real time. Furthermore, with commands from the ground center, UAVs can assist in fire suppression by spreading fire suppression liquid to extinguish the fire or dropping ignition spheres at the desired locations to intentionally set small fires under set conditions to clear vegetation that could become fuel in the future.

(3) *After*: UAVs can be used to evaluate damage and risks of forest fires. By mapping with UAVs, the ground team can obtain a full view of the terrain situations before and after the forest fire for the post-fire analysis. These information can be useful for the recovery over the terrains. In addition, UAVs can help crews find the unextinguished fires to warn firefighters operating away from the potential dangers.

1.2 Review of Related Works

Evidence suggests that wind behavior is one of the most important factors that has great impacts on the performance of UAVs and the propagation of forest fires. A considerable amount of research have been well studied on wind measurement and estimation approaches for UAVs, control of UAVs against wind disturbances, and forest fire monitoring approaches.

1.2.1 Wind Measurement and Estimation Approaches for UAVs

Wind measurement and estimation approaches have been widely developed on the UAV platforms. Especially, fixed-wing UAVs benefit from their relatively high endurance and the ability to traverse long distances to capture wind data in a broad range of areas with more specific sensors, although the forward-flight nature makes it impossible for continuous wind data collection at fixed point locations. In addition, rotary-wing UAVs, in particular multirotor UAVs, are increasingly used for in-situ wind measurements in low-altitude environments, due to their hovering capability and easy maneuverability. UAV-based wind measurement and estimation approaches can be applied to remotely collect wind data in many fields. For example, UAVs can be deployed over the forest fire region to collect wind data for the forest fire monitoring and fighting tasks.

To obtain wind data with UAVs, the most effective way is to measure wind speed and direction via the anemometers carried by the UAV platforms. The available wind sensors include but are not limited to the multi-hole pressure probe [6, 7, 8, 9, 10, 11, 12], the Pitot tube [13, 14, 15, 9, 16], the ultrasonic anemometer [17, 18, 19, 20, 21], and the hot-wire anemometer [22]. Reliable wind data can be produced by those chosen anemometers during flight, although additional wind sensors may reduce the battery life and increase the total expense.

However, in the case of no wind sensor or in the presence of wind sensor faults, indirect approaches can be adopted to estimate wind data from UAV motion without additional wind sensors. In general, there are two main types of indirect wind estimation approaches, namely model-based approaches and data-driven approaches.

Model-based approaches are proposed based on the dynamic model of a UAV with the consideration of wind effects acting on the UAV motion. The model-based approaches involve but are not limited to those based on state estimation, parameter identification, and disturbance observer. In [23], three approaches are compared for wind estimation based on three quadrotor models, i.e., the kinematic particle model, the dynamic particle model, and the rigid-body model. Each model is linearized about the hover equilibrium to enable the wind estimation using a state observer. The linear Kalman filter [24, 25], the extended Kalman filter [26, 27] and the unscented Kalman filter [28] are the most commonly used optimal state observers for wind estimation on a UAV. In [29], three time-varying parameter estimation algorithms are proposed for the wind estimation of a quadrotor based on the adaptive observers. In [30], a multi-objective optimization algorithm is used to estimate wind and identify aircraft model parameter. However, model-based approaches should be applied with accurate models of UAVs. To apply these approaches for UAVs, large amounts of effort should be invested to the mathematical model of aircraft dynamics.

Depending on previously observed data, data-driven approaches estimate or infer wind vectors by matching the similar patterns in the history. The data-driven approaches can characterize a static relationship between the wind vector and UAV states (or control responses) only from historical data. The relationships can be obtained by using data processing methods, such as the least-squares fitting method, the artificial intelligence method, etc. In [31], the oncoming flow velocity and direction can be determined from the bijective contour figure of oncoming flow vector and the required power of each rotor. In [32], a static relationship between the wind vector and Euler angles of a quadrotor UAV is obtained through wind tunnel tests. Based on previous work, the relationship function is corrected by adding the acceleration term in [33]. Artificial intelligence methods such as a long short-term memory (LSTM) neural network method is used in [34] to estimate wind vectors for a quadrotor UAV from the position and attitude measurements. Data-driven methods can be applied without understanding the complex dynamic model of a quadrotor UAV under wind effects. However, the real applications of data-driven methods face challenges of defining dataset to generate the mapping functions for wind estimation, solving overfitting issues and so on.

1.2.2 Control of UAVs Against Wind Disturbances

Wind behaviors have unavoidable impacts on the performances of UAVs in outdoor tasks, such as employing UAVs for the forest fire detection, monitoring, and fighting. External wind disturbances generate unexpected forces and moments acting on the UAV that will degrade the performance of the vehicle. In particular, small-scale UAVs are more sensitive to those external disturbances due to their low inertia and small size. Therefore, control of UAVs against wind disturbances should be investigated to ensure their performance of tracking desired trajectories and stability in the presence of unknown wind disturbances.

In recent years, lots of effort has been invested in developing the control strategies of UAVs under wind disturbances. One of the most efficient strategies is to design a robust controller to attenuate wind effects. In [35], two robust nonlinear sliding mode controllers are designed under wind perturbations. A switching model predictive attitude control is adopted based on a piecewise affine (PWA) model of the quadrotor's attitude dynamics against wind gust disturbances [36]. The $\mathcal{L}_1$ backstepping trajectory tracking control is adopted to allow for the fast adaption to rapidly changing system uncertainties and wind disturbances with the guaranteed robustness [37]. In [38], a robust nonlinear dynamic inversion attitude controller is proposed in the presence of model uncertainties and external disturbances of wind gusts, aerodynamic interactions with nearby structures, and ground effects, while a feedback position controller is used to handle the lateral and vertical transitions. In [39], the finite frequency H_∞ control is used for the attitude stabilization, while the PID-based H_∞ loop shaping control is used for the linear motion in the presence of wind disturbance. An acceleration feedback enhanced H_∞ control is adopted against wind disturbance in [40]. However, robust control methods have a high degree of conservativeness for the external disturbances defined by a norm bounded variable [41].

To improve the performance of UAV system against wind disturbances, unknown wind effects acting on the UAV dynamics are usually estimated to be rejected. To achieve this purpose, disturbance estimation and rejection techniques are developed, such as disturbance-observer-based control, active disturbance rejection control, embedded model control and composite hierarchical anti-disturbance control. Authors in [42] propose a detailed review of disturbance observer. In [43], a high-gain residual observer is implemented in an embedded robust attitude control of a quadrotor UAV for online estimation and compensation of wind gust disturbances. In [44], a multiple observers based anti-disturbance control is applied for a quadrotor UAV, where a composite disturbance observer together with an extended state observer are used in the position loop to mitigate the payload and wind disturbances and an extended state observer is used in the attitude loop to reject model uncertainties and wind disturbances. In [45], an attitude control for a UAV quadrotor is developed in the framework of active disturbance rejection control and embedded model control to estimate and reject the disturbances. In view of the idea of composite hierarchical anti-disturbance control, an adaptive composite disturbance rejection control is developed, containing active disturbance rejection control and disturbance observer, for attitude control of the agricultural quadrotor UAV [46]. In addition, the deep-learning-based control approaches have become increasingly attractive in recent years. To increase the robustness of the proposed control scheme, the deep-learning-based approach is adopted to learn the unknown aerodynamics of the UAV. In [47], a deep-learning-based trajectory tracking controller is developed to learn to quickly adapt to rapidly-changing wind conditions. To this end, the domain adversarially invariant meta-learning algorithm is developed for the offline learning of the common aerodynamic representation, while a composite adaption law is used to update wind-specific linear coefficients.

The sliding mode control schemes have been well studied for UAVs to solve the position and attitude tracking problems, due to its inherent robustness to model uncertainties and external disturbances. In [48], an adaptive fault tolerant control based on a multivariable integral terminal sliding mode control is developed in the presence of parametric uncertainties and actuator faults. An adaptive super-twisting sliding mode control is adopted for a quadrotor UAV to track a desired trajectory under gust winds [49]. An adaptive PID-based sliding mode control is offered for a quadrotor in the existence of external perturbations with unknown bounds [50]. In [51], the position and attitude control of a quadrotor UAV is realized by an optimized fuzzy-based sliding mode control. Based on the nonsingular terminal sliding mode control, the fault tolerant control for a quadrotor UAV is proposed with the consideration of model uncertainties and wind disturbances [52]. In [53], an adaptive nonsingular fast terminal sliding mode control is adopted to stabilize the attitude of a quadrotor, while a robust backstepping sliding mode control is used to follow the prescribed path.

1.2.3 Forest Fire Monitoring Approaches

In order to accurately monitor the situation of forest fires, the fire spread behavior has been studied. The fire environment, which incorporates the effects of weather, fuel, and topography, determines the propagation process of forest fires. To describe the characteristics of propagating forest fires, fire spread models are developed, such as the Rothermel model [54] and the Canadian Forest Fire Behavior Prediction system [55]. A review of wildland surface fire spread modelling is proposed in [56, 57, 58]. However, these predictive models are sensitive to the model input data, which are readily known to induce fire behaviors, such as the wind condition, fuel distribution, and slope steepness. When no accurate measurements or observations of these input data are provided, the estimation of forest fire spread must be produced with inevitable errors.

Among these factors, the wind condition plays an important role in driving the forest fire propagation and also for effective fire fighting using UAVs. As a result, many efforts have been made for the better understanding of wind effects on the spread of forest fires and the estimation of wind conditions for forest fire monitoring. The interaction of wind and fire is studied in [59]. In [60], authors provide an analysis of wildfire propagation in the presence of low-level environmental vertical wind shear through four comparative grassfire numerical simulations. In [61], the wildfire dynamics in wind-driven conditions is predicted using an inverse modelling approach. Considering the interaction between fire and wind, the spread rate of forest fire is predicted using UAV images and an LSTM model in [62]. In [63], a wireless sensor network is deployed to sense wind conditions at ground level to improve the prediction of wind-affected wildfire spread.

In recent years, to detect and monitor forest fires more quickly and accurately, UAVs are widely used in forest firefighting missions. UAVs can take the roles of firefighters when flying into the region of forest fires to monitor these flames with effective forest fire detection [64, 65, 66] and estimation techniques [67, 68]. With observations of the fires that are gathered via onboard sensors on the UAV platforms, firefighters can quickly obtain accurate information about the current status of forest fires from a distance and also use UAVs for firefighting, avoiding the threats of unexpected fire conditions to crews' lives. Therefore, the application of UAVs provides a promising and safety solution for the fast-response forest fire monitoring and fighting mission.

A large variety of data assimilation methods have been developed to estimate the condition of a propagating forest fire based on fire front observations. The Kalman filter is the most commonly used data assimilation method for the forest fire monitoring mission [68]. However, the major drawback of the standard Kalman filter is that it works with the assumption of linear Gaussian fire spread model. To overcome this limitation, extensions of the Kalman filter or other sequential Monte Carlo filtering methods have been proposed, for example, the extended Kalman filter [69], the unscented Kalman filter [69], the ensemble Kalman filter [70, 71, 72], and the particle filter [73, 74].

1.3 Objectives of This Thesis

The review of related works indicates the importance of accurate wind estimation for assuring the performance of UAVs and assessing the status of propagating forest fires in the presence of unknown winds. This thesis aims to estimate wind vectors from quadrotor motion and use the estimated wind information to maintain the performance of UAVs and provide accurate assessments of the wind-affected forest fires under unknown wind environments. In particular, this thesis is organized with the following objectives:

(1) Design and develop an online wind estimation approach that can extract wind information from quadrotor motion without additional wind sensors.

(2) Design and develop an active wind rejection control strategy for a quadrotor UAV to maintain its performance against unknown wind disturbances.

(3) Develop and implement the active wind rejection control scheme for multiple UAVs to improve their cooperative tracking performance in the unknown wind environments.

(4) Design and develop a UAV-based forest fire monitoring approach to obtain an accurate assessment of wind-affected forest fires.

1.4 Contributions of This Thesis

This thesis research contributes to the indirect wind estimation approach for a UAV without additional wind sensors, the active wind-rejection control scheme to increase the safety and reliability of UAVs against wind disturbances, and the UAV-based forest fire surveillance strategy to produce accurate assessments of wind-driven forest fires in unknown wind environments.

The main contributions of this thesis are summarized as follows:

(1) A particle filter-based approach is proposed to estimate wind vectors in the case of no additional flow sensors. Based on the nonlinear dynamics of a quadrotor UAV with wind effects, this approach can provide accurate state and wind estimation from quadrotor motion and reduce the influences of process and measurement noises.

(2) A two-stage particle filter framework is developed to increase the computational efficiency of the state and wind estimation for a quadrotor UAV. As a feature of the two-stage procedure, the subfilters in the second stage can produce wind estimation in parallel based on the state particles obtained from the first stage, improving the operational efficiency of the overall filter.

(3) An active wind rejection control based on adaptive nonsingular terminal sliding mode control is adopted for a quadrotor UAV to ensure its tracking performance in the presence of unknown wind disturbances. The external wind disturbances can be compensated for, depending on the explicit wind estimation obtained from the two-stage particle filter. In addition, an adaptive nonsingular terminal sliding mode control is adopted to guarantee the robustness, considering estimation errors and model uncertainties.

(4) An active wind rejection distributed formation control is further developed for multiple quadrotor UAVs in order to improve their cooperative tracking performance in the presence of wind disturbances.

(5) A Gaussian process regression-based wind field reconstruction approach is proposed using the wind data collected by UAVs in order to provide midflame wind prediction for the assessment of forest fire spread condition. To obtain the maximum amount of wind information about the forest front locations, the maximum mutual information method is applied to provide optimal wind sensing locations for UAVs.

(6) An ensemble Kalman filtering approach is developed for monitoring wind-affected

forest fires based on wind measurements and fire front observations with UAVs. Based on the reconstructed wind field, the wind input data can be sampled from a multivariate Gaussian distribution which consider the forest front locations.

1.5 Organization of This Thesis

This thesis is presented in six chapters including this chapter of introduction, the rest of which are organized as follows:

Chapter 2 provides several preliminary knowledge that will be used in this thesis. It starts with the dynamic model of a quadrotor UAV, considering wind effects acting on the UAV dynamics. Next, the equations of forest fire spread are obtained based on the popular Rothermel model, which can represent wind-affected fire spread on two-dimensional surfaces. Last, four wind models are given, including the constant wind, wind gust, wind turbulence, and log wind profile.

Chapter 3 proposes a two-stage particle filter-based wind estimation approach to extract wind information from quadrotor motion. Considering the increasingly refined dynamic model of a quadrotor, the particle filtering method is applied to address the problem of state and wind estimation with strong nonlinear and non-Gaussian characteristics. To further improve the computational efficiency of the particle filter, two-stage framework is adopted.

Chapter 4 presents an active wind rejection control of quadrotor UAVs based on the adaptive nonsingular terminal sliding mode control to improve their performances in the presence of winds. Based on the explicit wind estimation obtained from the proposed two-stage particle filter, an active wind rejection control is developed by compensating for the unexpected wind effects acting on the quadrotor UAV. The proposed control strategy can guarantee the finite-time convergence and avoid the singularity problem by using nonsingular terminal sliding mode control method. Furthermore, to ensure the cooperative tracking performance of multiple UAVs in the presence of unknown wind disturbances, the active wind rejection control scheme is implemented for the formation control of multiple quadrotor UAVs.

Chapter 5 develops a UAV-based forest fire monitoring approach to accurately assess the status of propagating forest fires induced by winds. To accurately monitor the propagation of forest fires, UAVs are deployed to collect the wind measurements and fire front observations for the assessment of status of wind-affected forest fires. The Gaussian process regression method is adopted to reconstruct the wind field over the fire region and the wind sensing locations are optimized by the maximum mutual information method. With the collected data, the fire front locations are estimated in an ensemble Kalman filter framework.

Chapter 6 draws some conclusions of these research works and summarizes several predominant ideas for the future developments of the thesis's outcomes.

Chapter 2

Preliminaries

2.1 Quadrotor UAV Model

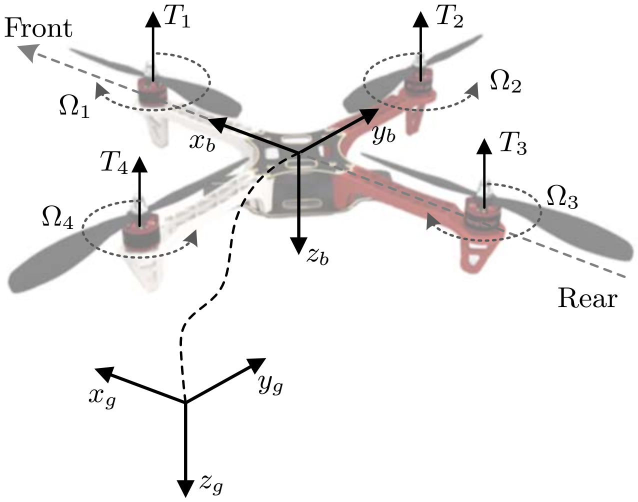

Figure 2.1: Reference frames and the quadrotor UAV configuration

The typical configuration and the reference frame of a quadrotor UAV are shown in Fig. 2.1. Its propulsion system is composed of four symmetrically configured rotors with propellers. Rotors 1 and 3 are arranged to rotate in the clockwise direction, while rotors 2 and 4 are arranged to rotate in the counter-clockwise direction. A quadrotor UAV is defined as an underactuated mechanical system, because it has six degrees of freedom but only four independently controlled actuators to generate force or moments to maneuver.

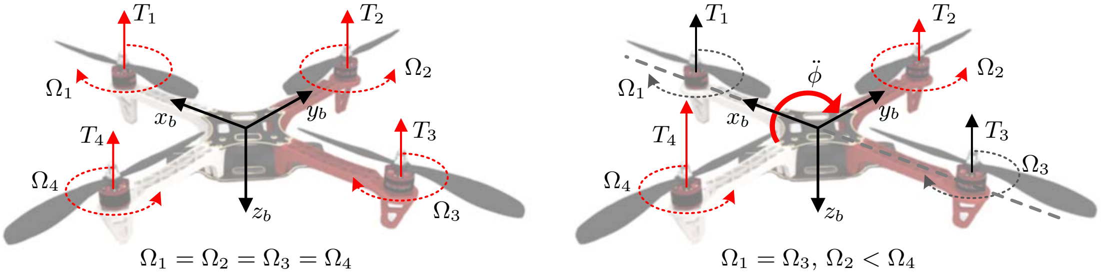

(a) Throttle maneuver

(b) Roll maneuver

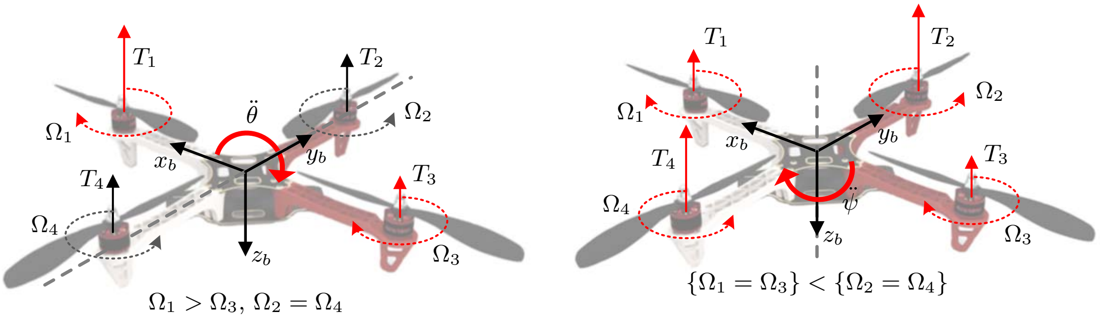

(c) Pitch maneuver

(d) Yaw maneuver

Figure 2.2: Maneuver schemes of a quadrotor UAV

The vehicle motion depends on the force and moment generated by the rotors' spin. Thrust and moment increase in direct relation to rotor rotation speed. The maneuver schemes of a quadrotor UAV are shown in Fig. 2.2. The throttle, roll, pitch, and yaw maneuvers are four basic maneuvers that allow a quadrotor UAV to arrive at a certain position. The throttle maneuver is achieved by equally increasing (or decreasing) all the rotation speeds of all rotors. In this case, all rotors are required to produce equal thrusts without generating any rotational moment. The roll maneuver is obtained by increasing (or decreasing) the rotation speed of rotor 4 while decreasing (or increasing) the rotation speed of rotor 2. In this case, due to the generation of roll moments generated by rotors 2 and 4, the vehicle can be rotate around the x_b-axis. Likewise, the quadrotor UAV can rotate around the y_b-axis, because of the pitch moment generated by rotors 1 and 3. The yaw maneuver is obtained by equally increasing (or decreasing) the rotation speed of rotors

2 and 4, while equally decreasing (or increasing) the rotation speed of rotors 1 and 3. In this case, the yaw angle is induced by mismatching the balance of thrusts of the rotor pairs rotating in the clockwise and counter-clockwise directions.

2.1.1 Newton-Euler Dynamic Model

The Newton-Euler dynamic model can be used to describe the translational and rotational motions of a quadrotor UAV. The body-fixed coordinate system and the earth-fixed coordinate system are illustrated in Fig. 2.1. The body-fixed coordinate system is a right-hand coordinate system attached to the rigid body of the vehicle, where the axis origin coincides with the center of mass of the quadrotor and x_b-axis, y_b-axis and z_b-axis point towards the front, right and down directions, respectively. The earth-fixed coordinate system is the inertial right-hand reference frame, where x_g-axis, y_g-axis and z_g-axis point towards the north, east and down directions, respectively.

To describe the dynamic model of a quadrotor UAV, the following assumptions are taken:

- The quadrotor mechanical design is symmetrical.
- The quadrotor body is rigid.

In the body-fixed coordinate system, the equations to describe the quadrotor motion are given by [75, 12, 23]

$$\begin{aligned} m\dot{\boldsymbol{v}} + m\boldsymbol{\omega} \times \boldsymbol{v} &= \boldsymbol{F} \\ \boldsymbol{I}\dot{\boldsymbol{\omega}} + \boldsymbol{\omega} \times \boldsymbol{I}\boldsymbol{\omega} &= \boldsymbol{M} \end{aligned} \tag{2.1}$$

where m is the mass, $\boldsymbol{I}$ is the inertia matrix, $\boldsymbol{v} = [u,\, v,\, w]^T$ represents the linear velocity vector, $\boldsymbol{\omega} = [p,\, q,\, r]^T$ represents the angular velocity vector, $\boldsymbol{F}$ denotes the external force vector, and $\boldsymbol{M}$ denotes the external moment vector.

Based on the assumption of symmetrical body, the inertia matrix is written as

$$\boldsymbol{I} = \begin{bmatrix} I_x & & \\ & I_y & \\ & & I_z \end{bmatrix} \tag{2.2}$$

where I_x is the inertia moment along the x_b-axis, I_y is the inertia moment along the y_b-axis, and I_z is the inertia moment along the z_b-axis.

To determine the trajectory of a quadrotor UAV in the earth-fixed coordinate system, the ground speed of quadrotor should be expressed according to the linear velocity in the body-fixed coordinate system. Let $\boldsymbol{P} = [x,\ y,\ z]^T$ denote the position vector of a quadrotor UAV, $\boldsymbol{V}_g = [\dot{x},\ \dot{y},\ \dot{z}]^T$ denote the ground speed vector, and $\boldsymbol{\Theta} = [\phi,\ \theta,\ \psi]^T$ denote the Euler angle vector, where ϕ, θ and ψ are the roll, pitch and yaw angles. The ground speed vector of the aircraft can be expressed as

$$\boldsymbol{V}_g = \mathbf{R}\boldsymbol{v} \tag{2.3}$$

where $\mathbf{R}$ is the rotation matrix, which transfers free vectors from the body-fixed coordinate system to the earth-fixed coordinate system with the yaw-pitch-roll rotation sequence [75, 12, 23]:

$$\mathbf{R} = \begin{bmatrix} \cos\theta\cos\psi & \sin\phi\sin\theta\cos\psi - \cos\phi\sin\psi & \cos\phi\sin\theta\cos\psi + \sin\phi\sin\psi \\ \cos\theta\sin\psi & \sin\phi\sin\theta\sin\psi + \cos\phi\cos\psi & \cos\phi\sin\theta\sin\psi - \sin\phi\cos\psi \\ -\sin\theta & \sin\phi\cos\theta & \cos\phi\cos\theta \end{bmatrix} \tag{2.4}$$

Similarly, the Euler angle derivatives can be obtained according to the angular velocities in the body-fixed coordinate system

$$\dot{\boldsymbol{\Theta}} = \mathbf{L}\boldsymbol{\omega} \tag{2.5}$$

where the transfer matrix is written as [75, 12, 23]

$$\mathbf{L} = \begin{bmatrix} 1 & \sin\phi\tan\theta & \cos\phi\tan\theta \\ 0 & \cos\phi & -\sin\phi \\ 0 & \sin\phi\sec\theta & \cos\phi\sec\theta \end{bmatrix} \tag{2.6}$$

The external forces and moments acting on the quadrotor body are comprised of several forces and moments [75, 12, 23]:

$$\begin{aligned} \boldsymbol{F} &= \boldsymbol{F}_g + \boldsymbol{F}_d + \boldsymbol{F}_c + \boldsymbol{F}_\delta \\ \boldsymbol{M} &= \boldsymbol{M}_d + \boldsymbol{M}_c + \boldsymbol{M}_\delta \end{aligned} \tag{2.7}$$

where $\boldsymbol{F}_g$ represents the gravity force vector in the body-fixed coordinate system, $\boldsymbol{F}_d$ and $\boldsymbol{M}_d$ represent the drag force and moment vectors caused by relative air speed, $\boldsymbol{F}_c$ and $\boldsymbol{M}_c$ represent the control force and moment vectors induced by the propulsion system, and $\boldsymbol{F}_\delta$ and $\boldsymbol{M}_\delta$ represent the perturbation force and moment vectors.

The control forces and moments of the quadrotor UAV are generated by four rotors of the propulsion system. As aforementioned, the maneuvers of a quadrotor UAV are accomplished with the control of four independent rotors. Mathematically, according to the quadrotor configuration shown in Fig. 2.1, the control force and moment vectors can be written as

$$\boldsymbol{F}_c = \begin{bmatrix} 0 \\ 0 \\ -F_z \end{bmatrix}, \quad \boldsymbol{M}_c = \begin{bmatrix} \tau_\phi \\ \tau_\theta \\ \tau_\psi \end{bmatrix} \tag{2.8}$$

with

$$\begin{bmatrix} F_z \\ \tau_\phi \\ \tau_\theta \\ \tau_\psi \end{bmatrix} = \begin{bmatrix} 1 & 1 & 1 & 1 \\ 0 & -l & 0 & l \\ l & 0 & -l & 0 \\ -k_m & k_m & -k_m & k_m \end{bmatrix} \begin{bmatrix} T_1 \\ T_2 \\ T_3 \\ T_4 \end{bmatrix} \tag{2.9}$$

where T_i denotes the thrust of rotor i with $i = 1, \cdots, 4$, l is the arm length, and k_m is the thrust-to-moment coefficient.

2.1.2 Wind Effects on Quadrotor UAV

The relative airspeed plays an important role to generate drag forces and moments acting on a quadrotor UAV [76, 29]. When a quadrotor has low aerodynamic profile and moves at low translational velocities in a no-wind environment, these aerodynamic effects on the quadrotor body or rotors are usually neglected. However, drag forces and moments are nonnegligible to affect the performance of aircraft, when the quadrotor suffers from the natural winds.

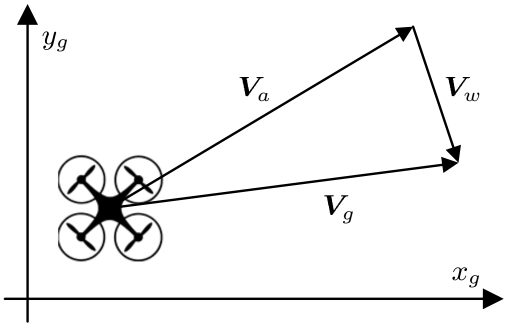

Figure 2.3: Wind triangle relationship between quadrotor ground speed vector, airspeed vector and wind vector

The wind triangle relationship basically encapsulates the vector relationship between the ground speed vector $\boldsymbol{V}_g$, the airspeed vector $\boldsymbol{V}_a$ and the wind speed vector $\boldsymbol{V}_w$, as illustrated in Fig. 2.3. The existence of wind speed vector results in the difference between the ground speed vector and airspeed vector. In the case of no wind, the airspeed vector is equal to the ground speed vector.

In general, the ground speed of the aircraft can be provided by the onboard GPS or IMU, while the airspeed can be measured via onboard airspeed sensors, such as Pitot tube. Subsequently, the wind vector acting on the aircraft can be determined by the difference between measurements of ground speed and airspeed. However, when airspeed sensors fault or lack, for example, airspeed sensors equipped on a quadrotor UAV are vulnerable to the downwash flow induced by rotors, the wind vector can be estimated from quadrotor motion.

This thesis mainly focuses on the wind effects that lead to the position drift of a quadrotor UAV. Given the quadrotor ground speed vector and wind vector, one can calculate the airspeed vector to generate the drag forces. The drag forces generated by wind effect can be approximated as [75, 23, 34]

$$
\begin{aligned}
F_{dx} &= C_{dxy}(\xi_x - \dot{x})\sqrt{(\xi_x - \dot{x})^2 + (\xi_y - \dot{y})^2} \\
F_{dy} &= C_{dxy}(\xi_y - \dot{y})\sqrt{(\xi_x - \dot{x})^2 + (\xi_y - \dot{y})^2} \\
F_{dz} &= C_{dz}(\xi_z - \dot{z})
\end{aligned}
\tag{2.10}
$$

where F_{dx}, F_{dy} and F_{dz} are the three components of the drag force vector, C_{dxy} and C_{dz} are the lateral and vertical drag coefficients, and ξ_x, ξ_y and ξ_z are the three components of the wind vector in the earth-fixed coordinate system. It is noted that lateral and vertical drag forces are separated. The vertical component of the airspeed contributes no lateral drag force, while the lateral component of the airspeed contributes no vertical drag force. The lateral component of the drag force is modeled by the standard aerodynamic effect equation. Different from the lateral component of the drag force, the vertical component of the drag force can be understood as a propulsive damping effect.

2.1.3 Simplified Dynamic Model

Considering the wind effects acting on the quadrotor UAV, the dynamic model of a quadrotor UAV is given by Eqs. (2.1)-(2.10), which involve the most typical elements to describe the quadrotor motion. Two coordinate systems are used to describe the transnational and rotational motion of the vehicle. For the convenience of the fast digital simulation, the dynamic model of a quadrotor needs to be simplified.

With the assumption of the low amplitude of angular motion, the approximations of $\boldsymbol{V}_g \approx \boldsymbol{v}$ and $\dot{\boldsymbol{\Theta}} \approx \boldsymbol{\omega}$ can be obtained. Therefore, the quadrotor dynamic model can be simplified as

$$\begin{aligned}
\ddot{x} =& -\frac{(\cos\phi\sin\theta\cos\psi + \sin\phi\sin\psi)F_z}{m} \\
&+ \frac{C_{dxy}(\xi_x - \dot{x})\sqrt{(\xi_x - \dot{x})^2 + (\xi_y - \dot{y})^2}}{m} + \frac{d_x}{m} \\
\ddot{y} =& -\frac{(\cos\phi\sin\theta\sin\psi - \sin\phi\cos\psi)F_z}{m} \\
&+ \frac{C_{dxy}(\xi_y - \dot{y})\sqrt{(\xi_x - \dot{x})^2 + (\xi_y - \dot{y})^2}}{m} + \frac{d_y}{m} \\
\ddot{z} =& -\frac{(\cos\phi\cos\theta)F_z}{m} + g + \frac{C_{dz}(\xi_z - \dot{z})}{m} + \frac{d_z}{m} \\
\ddot{\phi} =& \frac{I_y - I_z}{I_x}\dot{\theta}\dot{\psi} + \frac{\tau_\phi}{I_x} + \frac{d_\phi}{I_x} \\
\ddot{\theta} =& \frac{I_z - I_x}{I_y}\dot{\phi}\dot{\psi} + \frac{\tau_\theta}{I_y} + \frac{d_\theta}{I_y} \\
\ddot{\psi} =& \frac{I_x - I_y}{I_z}\dot{\phi}\dot{\theta} + \frac{\tau_\psi}{I_z} + \frac{d_\psi}{I_z}
\end{aligned} \tag{2.11}$$

where d_i for $i \in \{x,\, y,\, z,\, \phi,\, \theta,\, \psi\}$ represents the lumped disturbances. Parameters of a quadrotor dynamic model are listed in Table 2.1.

To be closer to the real model of a quadrotor model, the states of the quadrotor UAV are polluted with zero-mean Gaussian noises. The variances of the process and measurement noises are listed in Tables 2.2 and 2.3, respectively.

Table 2.1: Parameters of the quadrotor dynamic model

Symbol	Parameter	Value	Unit
m	Mass of quadrotor	1.5	kg
g	Gravity	9.8	$\mathrm{N/kg}$
I_x	Inertial moment along x_b-axis	0.03	$\mathrm{kg}\cdot\mathrm{m}^2$
I_y	Inertial moment along y_b-axis	0.03	$\mathrm{kg}\cdot\mathrm{m}^2$
I_z	Inertial moment along z_b-axis	0.05	$\mathrm{kg}\cdot\mathrm{m}^2$
C_{dxy}	Lateral drag coefficient	0.3	-
C_{dz}	Vertical drag coefficient	0.5	-
l	Arm length	0.4	m
k_m	Thrust-to-moment coefficient	0.1	-

Table 2.2: Variance of process noise

Error source	Symbol	Variance	Unit
Position	x, y, z	1×10^{-6}	$(\mathrm{m})^2$
Linear velocity	$\dot{x}, \dot{y}, \dot{z}$	1×10^{-6}	$(\mathrm{m/s})^2$
Attitude	ϕ, θ, ψ	1×10^{-12}	$(\mathrm{rad})^2$
Angular velocity	$\dot{\phi}, \dot{\theta}, \dot{\psi}$	1×10^{-12}	$(\mathrm{rad/s})^2$

Table 2.3: Variance of measurement noise

Error source	Symbol	Variance	Unit
Position	x, y, z	1×10^{-4}	$(\mathrm{m})^2$
Linear velocity	$\dot{x}, \dot{y}, \dot{z}$	1×10^{-4}	$(\mathrm{m/s})^2$
Attitude	ϕ, θ, ψ	1×10^{-4}	$(\mathrm{rad})^2$
Angular velocity	$\dot{\phi}, \dot{\theta}, \dot{\psi}$	1×10^{-4}	$(\mathrm{rad/s})^2$

2.2 Forest Fire Spread Model

2.2.1 One-dimensional Rothermel Model

The Rothermel model [54, 77] is one of the widely used fire spread model, which determine the rate of fire spread as a function of the local environmental factors such as wind, topography, vegetation properties, etc. The no-wind, no-slope rate of spread is given by [54, 77, 78, 79, 80]

$$R_0 = \frac{I_R \xi_{pf}}{\rho_b \varepsilon_h Q_{ig}} \tag{2.12}$$

where I_R is the reaction intensity, ξ_{pf} is the propagating flux ratio, ρ_b is the bulk density, ε_h is the effective heating factor, and Q_{ig} is the heat of preignition.

Considering wind effects on the fire propagation, the rate of spread should be corrected by the wind coefficient [54, 77, 78, 79, 80]

$$R = R_0(1 + \Phi_w) \tag{2.13}$$

The wind coefficient derived from the experimental data is calculated as [54, 77, 78, 79, 80]

$$\Phi_w = C(3.281U_f)^B(\frac{\beta}{\beta_{op}})^{-E} \tag{2.14}$$

with

$$\begin{aligned} B &= 0.15988\sigma^{0.54} \\ C &= 7.47\exp(-0.8711\sigma^{0.55}) \\ E &= 0.715\exp(-0.01094\sigma) \\ \beta_{op} &= 0.20395\sigma^{-0.8189} \end{aligned} \tag{2.15}$$

where U_f denotes the mid-flame wind speed, β represents the packing ratio of the fuel bed, and σ is surface area-to-volume ratio. The mid-flame wind can be calculated by [81]

$$U_f = U_0 \frac{1.83}{\ln\left(\frac{6.1+0.36h_f}{0.13h_f}\right)} \tag{2.16}$$

where U_0 is the wind vector at altitude of $6.1\,\mathrm{m}$ above the vegetation top and h_f is the fuel height.

Table 2.4 gives the parameters of fire spread model, which are adopted in the following simulations.

Table 2.4: Parameters of the fire spread model

Symbol	Parameter	Value	Unit
R_0	No-wind, no-slope rate of spread	1	$\mathrm{m/s}$
β	Packing ratio of the fuel bed	0.002	-
σ	Surface area-to-volume ratio	4000	$/\mathrm{m}$
h_f	Fuel height	1.5	m

2.2.2 Extension to Two-dimensional Surfaces

The Rothermel model describes the one-dimensional fire spread, but the wind effects contribute differently to the fire spread in different conditions. For example, the wind contribution is maximum when the wind blows in the direction of fire spread. On the contrary, the wind contribution is minimum and negative when the wind blows opposite to the direction of fire spread. Thus, the fire spread should be modeled in the horizontal plane in order to account for the wind effects on the propagation of fire fronts. For this purpose, the elliptical fire spread model [82, 83] extends the two-dimensional fire propagation configurations based on the Rothermel model.

Fig. 2.4 shows the geometry of the elliptical fire spread model. According to the Huygens principle, this model assumes that every point on the fire front spreads following

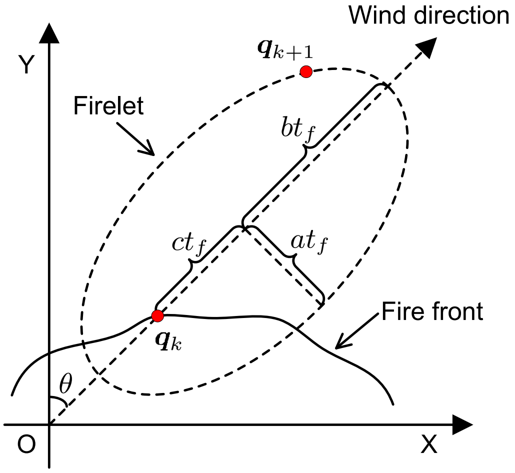

Figure 2.4: Elliptical fire spread model

an elliptical geometry. Let $\boldsymbol{q}_k$ denote a point on the fire front at time instant t_k and $\boldsymbol{q}_{k+1}$ denote a point on the fire front at time instant t_{k+1} where t_f is the time interval to spread the fire point. The spread rates of the ellipse is calculated as [54, 77, 78, 79, 80]

$$\begin{aligned} a &= \frac{b}{LB} \\ b &= \frac{1}{2}(R + \frac{R}{HB}) \\ c &= b - \frac{R}{HB} \end{aligned} \tag{2.17}$$

where a is the velocity with respect to the semi-minor axis, b is the velocity with respect to the semi-major axis, c is the velocity between the ignition point and the center of the ellipse, LB denotes the length-to-breadth ratio, and HB denotes the heading-to-backing fire spread rate ratio. The LB and HB are determined by [54, 77, 78, 79, 80]

$$\begin{aligned} LB &= 0.936e^{0.2566U_f} + 0.461e^{-0.1548U_f} - 0.397, \\ HB &= \frac{LB + \sqrt{LB^2 - 1}}{LB - \sqrt{LB^2 - 1}}. \end{aligned} \tag{2.18}$$

The spread rates of the fire point in the X- and Y-directions are computed as [82, 83]

$$\begin{aligned}\dot{q}_x =& D[a^2 \cos\varphi_w(x_s \sin\varphi_w + y_s \cos\varphi_w) - b^2 \sin\varphi_w(x_s \cos\varphi_w \\ &- y_s \sin\varphi_w)] + c \sin\varphi_w \\ \dot{q}_y =& D[-a^2 \sin\varphi_w(x_s \sin\varphi_w + y_s \cos\varphi_w) - b^2 \cos\varphi_w(x_s \cos\varphi_w \\ &- y_s \sin\varphi_w)] + c \cos\varphi_w \\ D =& [a^2(x_s \sin\varphi_w + y_s \cos\varphi_w)^2 + b^2(x_s \cos\varphi_w - y_s \sin\varphi_w)^2]^{-\frac{1}{2}}\end{aligned} \tag{2.19}$$

where φ_w is the azimuth angle of wind direction and $\boldsymbol{n}_s = [x_s,\, y_s]^T$ is the vector normal to the fire front.

2.3 Wind Models

2.3.1 Constant Wind

The constant wind model is a general wind model to approximate the wind situation in nature. It can provide statistic values of the average winds speed with temporal and spatial variations in three directions. Normally, the constant wind model is applied as a basis to provide a more effective simulation environment by incorporating with other kinds of winds. The model of constant wind can be written as

$$V_w = V_{wc}(x,\, y,\, z,\, t) \tag{2.20}$$

2.3.2 Wind Gust

The discrete 1-cosine wind gust model [84, 85] can represent the gust feature over time or in space. The wind gust in a temporal form can be written as

$$V_w = \begin{cases} 0 & t < t_{gs} \\ \frac{V_{gm}}{2}(1 - \cos\frac{2\pi(t-t_{gs})}{t_g}) & t_{gs} \leq t \leq t_{gs} + t_g \\ 0 & t > t_{gs} + t_g \end{cases} \tag{2.21}$$

where V_{gm} is the maximum gust velocity, t_{gs} is the starting time of wind gust, and t_g is the gust endurance time. The wind gust model is used to describe a sudden change of wind velocities. In general, the variation of wind gust speed between the peaks and average wind is greater than $4.5\,\mathrm{m/s}$ in a short time interval.

2.3.3 Wind Turbulence

The popular Dryden turbulence model is employed to generate a continuous turbulence. The model describes the characteristics of the turbulence flows in three directions by the spectral functions [86]

$$\begin{aligned} \Phi_u(\Omega) &= \sigma_u^2 \frac{2L_u}{\pi} \frac{1}{1 + (L_u\Omega)^2} \\ \Phi_v(\Omega) &= \sigma_v^2 \frac{L_v}{\pi} \frac{1 + 3(L_v\Omega)^2}{(1 + (L_v\Omega)^2)^2} \\ \Phi_w(\Omega) &= \sigma_w^2 \frac{L_w}{\pi} \frac{1 + 3(L_w\Omega)^2}{(1 + (L_w\Omega)^2)^2} \end{aligned} \tag{2.22}$$

where Φ_u, Φ_v, and Φ_w are the component spectral functions in three directions, σ_u, σ_v, and σ_w are the turbulence intensities, and L_u, L_v, and L_w are the turbulence scale lengths. At low altitudes, the turbulence intensities and scale lengths are given as

$$\begin{aligned}\sigma_w &= 0.1W_{20}\\ \sigma_u &= \frac{\sigma_w}{(0.177+0.000823h)^{0.4}}\\ \sigma_v &= \frac{\sigma_w}{(0.177+0.000823h)^{0.4}}\end{aligned} \tag{2.23}$$

$$\begin{aligned}L_w &= h\\ L_u &= \frac{h}{(0.177+0.000823h)^{1.2}}\\ L_v &= \frac{h}{(0.177+0.000823h)^{1.2}}\end{aligned} \tag{2.24}$$

where W_{20} denotes the wind speed at the altitude of $6\ \mathrm{m}$ and h denotes the height of aircraft.

2.3.4 Log Wind Profile

The log wind profile is used to describe the relationship between wind speeds at different heights. At lower altitudes, the wind profile of the atmospheric boundary layer is logarithmic [81].

$$V_w(h) = \frac{U_*}{\kappa}\ln\left(\frac{h-d_0}{z_0}\right) \tag{2.25}$$

where $V_w(h)$ is the wind speed at the altitude h above the ground, U_* is the friction velocity, $\kappa = 0.4$ is the Von Kármán constant, d_0 is the zero plane displacement and z_0 is the surface roughness.

In order to estimate the mean wind speed at the altitude of h_2 based on that at the altitude of h_1, the calculation is given by

$$V_w(h_2) = V_w(h_1)\frac{\ln\left(\frac{h_2-d_0}{z_0}\right)}{\ln\left(\frac{h_1-d_0}{z_0}\right)} \tag{2.26}$$

Values of d_0 and z_0 are related to the fuel height h_f as $d_0 = 0.64h_f$ and $z_0 = 0.13h_f$. The wind speed at the altitude of h above the vegetation top is given by

$$V_w(h + h_f) = \frac{U_*}{\kappa} \ln\left(\frac{h + 0.36h_f}{0.13h_f}\right) \tag{2.27}$$

The relationship between the midflame wind speed and the wind speed at the height of h above the vegetation top is given by

$$U_f = V_w(h + h_f) \frac{1.83}{\ln\left(\frac{h+0.36h_f}{0.13h_f}\right)} \tag{2.28}$$

2.4 Summary

This chapter presents the preliminaries of this thesis, including the dynamic model of a quadrotor UAV, forest fire spread model, and wind models. First, the Newton-Euler dynamic model is used to describe the translational and rotational motions of a quadrotor UAV. In the dynamic model, the wind effects acting on the aircraft are also considered. Second, the Rothermel model is used to describe the one-dimensional fire spread and extended to the two-dimensional fire spread according to the Huygen's principle. Third, the constant wind, the wind gust, the wind turbulence, and the log wind profile are introduced.

Chapter 3

Two-Stage Particle Filter-based Wind Estimation from Quadrotor Motion

3.1 Problem Formulation

This chapter investigates the problem of wind estimation for a quadrotor UAV without the need of additional wind sensors or in the case when wind sensors are faulty, where the wind information is important toward certain time- and safety-critical applications such as forest fire monitoring and fighting using unmanned aerial vehicles. The wind vectors are the time-varying parameters of the quadrotor dynamic model. A two-stage particle filter algorithm is proposed to estimate wind vectors from quadrotor motion.

The Kalman filter approach is widely used to solve the state and parameter estimation (SPE) problems, whereas it gradually loses efficiency in the wind estimation, due to the increasingly refined models with strong nonlinear and non-Gaussian characteristics. To overcome this issue, this chapter resorts to the particle filter which is good at solving the SPE problems of the nonlinear and non-Gaussian systems [87]. The particle filter can approximate the posterior distributions of the UAV states and wind vectors by sampling particles without the restrictive assumptions on the quadrotor model. With a perfect understanding of the quadrotor dynamic model, the particle filter can effectively reduce the impacts of the process and measurement noises on the states and wind estimation.

To improve the efficiency of particle filter in high dimensions, the particle filtering process is executed in a two-stage framework. To estimate states and wind parameters for a quadrotor UAV, a natural solution is to redefine an augmented state vector for the standard particle filter approach, comprised of the vehicke states and wind parameters. However, this solution suffers from the challenge of particle samplings caused by the dimension growth of the augmented state. By adopting the proposed two-stage framework, this problem can be mitigated as the sampling processes of UAV states and wind vectors are divided into two stages of the particle filter. As a result, the computational efficiency can be improved since the resampling process of wind vectors in the second-stage particle filter can be executed in parallel. The two-stage framework has been widely used with the Kalman filter in the actuator fault detection and diagnosis of a quadrotor UAV [88, 89].

Up to now, few works have been conducted on developing a two-stage particle filter for the state and wind estimation from quadrotor motion. In [90], a two-stage particle filter is used to estimate the non-Gaussian state with fading measurements. Motivated by the work in [90], this chapter adopts the two-stage particle filter to estimate the unknown wind vectors from quadrotor motion. This chapter extends the two-stage particle filter (TSPF) to solve the problem of state and wind parameter estimation based on the nonlinear dynamic model of a quadrotor UAV. By using the random walk model to describe the continuous variation of wind vectors, the states of quadrotor and the time-varying wind parameters are simultaneously estimated through the proposed TSPF approach.

3.2 General Particle Filter

To introduce the particle filtering technique, a general nonlinear stochastic system can be described as

$$\begin{aligned} \boldsymbol{x}_k &\sim p(\boldsymbol{x}_k|\boldsymbol{x}_{k-1}) \\ \boldsymbol{z}_k &\sim p(\boldsymbol{z}_k|\boldsymbol{x}_k) \end{aligned} \tag{3.1}$$

where $\boldsymbol{x}_k \in \mathbb{R}^n$ and $\boldsymbol{z}_k \in \mathbb{R}^m$ is the state and observation vectors.

The particle filter makes use of the Bayesian approach to compute or approximate the posterior distribution of the hidden states given the observations. The posterior distribution of the hidden states is denoted as $p(\boldsymbol{x}_k|\boldsymbol{z}_{1:k})$, where $\boldsymbol{z}_{1:k} = \{\boldsymbol{z}_1, \cdots \boldsymbol{z}_k\}$. To overcome the difficulty of obtaining the analytic solution of $p(\boldsymbol{x}_k|\boldsymbol{z}_{1:k})$, the particle filter approximates the posterior distribution with a set of particles. However, there is still a problem of drawing particles from the unknown $p(\boldsymbol{x}_k|\boldsymbol{z}_{1:k})$. To deal with the problem of sampling particles from the posterior distribution, the important sampling technique is adopted. In this way, the particles can be drawn from a proposal importance distribution with proper weights

$$\begin{aligned} \boldsymbol{x}_k^{(i)} &\sim q(\boldsymbol{x}_{0:k}|\boldsymbol{z}_{1:k}) \\ w_k^{(i)} &= \frac{p(\boldsymbol{x}_{0:k}|\boldsymbol{z}_{1:k})}{q(\boldsymbol{x}_{0:k}|\boldsymbol{z}_{1:k})} \end{aligned} \tag{3.2}$$

where $\boldsymbol{x}_k^{(i)}$ represents the particle drawn from the sampling distribution, $w_k^{(i)}$ is the corresponding weights of $\boldsymbol{x}_k^{(i)}$, and $\boldsymbol{x}_{0:k} = \{\boldsymbol{x}_0, \cdots \boldsymbol{x}_k\}$. $q(\boldsymbol{x}_{0:k}|\boldsymbol{z}_{1:k})$ is the proposal distribution of the particle propagation.

Therefore, the posterior distribution $p(\boldsymbol{x}_k|\boldsymbol{z}_{1:k})$ can be approximated as

$$p(\boldsymbol{x}_k|\boldsymbol{z}_{1:k}) \approx \frac{1}{N}\sum_{i=1}^{N} \tilde{w}_k^{(i)}\delta(\boldsymbol{x}_k - \boldsymbol{x}_k^{(i)}) \tag{3.3}$$

where N is the number of particles, $\tilde{w}_k^{(i)} = \frac{w_k^{(i)}}{\sum_{i=1}^{N} w_k^{(i)}}$ is the normalized weight of each particle, and $\delta(\cdot)$ is the Dirac delta measure. With the approximation, the estimate of $\boldsymbol{x}_k$ given $\boldsymbol{z}_{1:k}$ can be obtained by

$$\hat{\boldsymbol{x}}_k \approx \frac{1}{N}\sum_{i=1}^{N}\boldsymbol{x}_k^{(i)} \tag{3.4}$$

To obtain the importance weight of each particle in a recursive fashion, the sequential importance sampling technique is used. The proposal distribution is chosen as

$$q(\boldsymbol{x}_{0:k}|\boldsymbol{z}_{1:k}) = q(\boldsymbol{x}_{0:k-1}|\boldsymbol{z}_{1:k-1})q(\boldsymbol{x}_k|\boldsymbol{x}_{0:k-1},\, \boldsymbol{z}_{1:k}) \tag{3.5}$$

The posterior distribution of $\boldsymbol{x}_k$ can be deduced as

$$p(\boldsymbol{x}_{0:k}|\boldsymbol{z}_{1:k}) = p(\boldsymbol{x}_{0:k-1}|\boldsymbol{z}_{1:k-1})\frac{p(\boldsymbol{z}_k|\boldsymbol{x}_k)p(\boldsymbol{x}_k|\boldsymbol{x}_{k-1})}{p(\boldsymbol{z}_k|\boldsymbol{z}_{1:k-1})} \tag{3.6}$$

As a result, the importance weight can be updated as

$$\begin{aligned} w_k^{(i)} &= \frac{p(\boldsymbol{x}_{0:k}|\boldsymbol{z}_{1:k})}{q(\boldsymbol{x}_{0:k}|\boldsymbol{z}_{1:k})} \\ &\propto w_{k-1}^{(i)}\frac{p(\boldsymbol{z}_k|\boldsymbol{x}_k^{(i)})p(\boldsymbol{x}_k^{(i)}|\boldsymbol{x}_{k-1}^{(i)})}{q(\boldsymbol{x}_k^{(i)}|\boldsymbol{x}_{0:k-1}^{(i)},\, \boldsymbol{z}_{1:k})} \end{aligned} \tag{3.7}$$

If the importance distribution satisfies

$$q(\boldsymbol{x}_k|\boldsymbol{x}_{0:k-1},\, \boldsymbol{z}_{1:k}) = q(\boldsymbol{x}_k|\boldsymbol{x}_{k-1},\, \boldsymbol{z}_k) \tag{3.8}$$

then

$$w_k^{(i)} \propto w_{k-1}^{(i)}\frac{p(\boldsymbol{z}_k|\boldsymbol{x}_k^{(i)})p(\boldsymbol{x}_k^{(i)}|\boldsymbol{x}_{k-1}^{(i)})}{q(\boldsymbol{x}_k^{(i)}|\boldsymbol{x}_{k-1}^{(i)},\, \boldsymbol{z}_k)} \tag{3.9}$$

Ideally, the particles are always propagated with equal weights for the state estimation. However, it is unavoidable that a few particles will have negligible weights after several iterations in a general particle filter procedure. In order to solve the particle degeneracy problem, the resampling technique is adopted for the particle filter. The technique is also referred as sampling importance resampling algorithm. After the resampling procedure, a set of particles with equal weights can be obtained to approximate the posterior distribution. The traditional resampling methods are proposed, including the multinomial resampling, the stratified resampling, the systematic resampling, and the residual resampling. Although the resampling step can prevent the particle from degeneracy, it also has undesired effects. The resampling step will lead to the particle impoverishment since the low-weighted particles are most likely to be removed and many of the offspring particles will be the same. As a result, the diversity of the particles is reduced. This inevitable information damage will increase uncertainty in the random sampling. Moreover, it is rather challenging to operate resampling in parallel, which implies a longer execution time of the particle filter algorithm.

3.3 Wind Estimation Framework

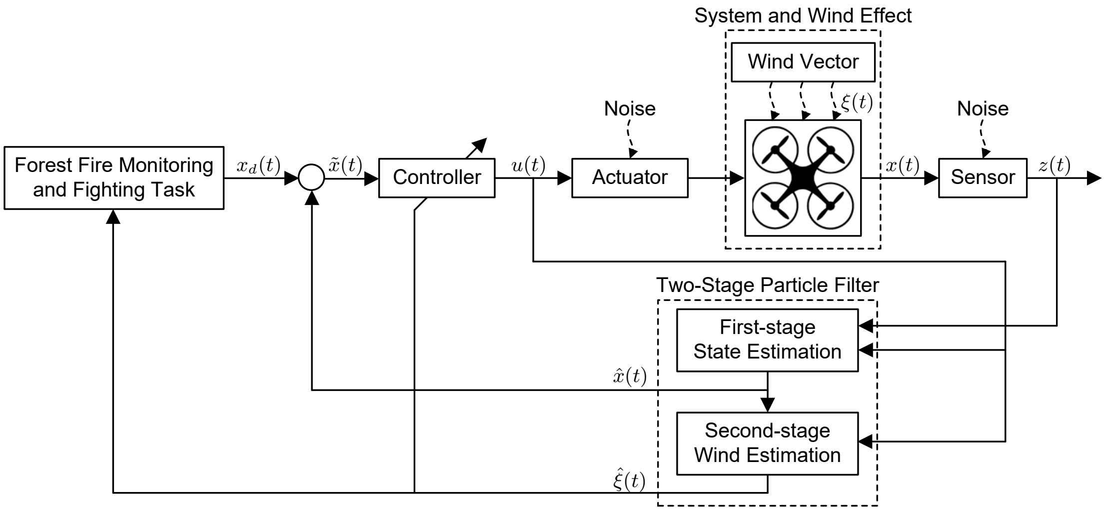

Figure 3.1: Framework of the proposed TSPF scheme for the state and wind estimation from quadrotor motion

The framework of the proposed TSPF scheme for the state and wind estimation from quadrotor motion is demonstrated in Fig. 3.1. The wind vector is estimated as the unknown parameters of the quadrotor UAV system based on the dynamic model with wind effects. Considering the nonlinear and non-Gaussian model, the particle filter algorithm is adopted to estimate the time-varying wind parameters given the control inputs and the quadrotor motion measurements. However, there is no direct relationship between the wind vector and measurements, the particle filter is designed in the two-stage structure, where the first-stage particle filter produces the state estimation from the measurements of UAV motion and the second-stage particle filter estimates wind vectors based on the estimated states. Moreover, the efficiency of the filtering process can be improved by using the cascaded structure as the second-stage filtering can be done in parallel. The particle filter procedure can reduce the influences of the process and measurement noises to provide accurate estimates of states and wind vectors for the vehicle. The estimates can feed back to making decisions to the forest fire monitoring and fighting tasks, for example, the obtained wind information can be used to generate trajectories to reduce the quadrotor power consumption in the forest fire monitoring or to decide the drop location of fire suppression fluid to extinguish fires. In addition, the estimates of quadrotor states and wind vectors can feed back to the controller to improve the performance of quadrotor UAV in the presence of unknown winds.

3.4 Two-Stage Particle Filter-based Wind Estimation

3.4.1 Discrete-Time Model of a Quadrotor UAV

Let $\boldsymbol{\xi}_k$ denote the wind vector, $\boldsymbol{x}_k$ denote the state vector of UAV, $\boldsymbol{u}_k$ denote the control input vector at time instant t_k

$$\begin{aligned} \boldsymbol{\xi}_k &= [\xi_{x,k},\, \xi_{y,k},\, \xi_{z,k}]^T \\ \boldsymbol{x}_k &= [x_k,\, y_k,\, z_k,\, \dot{x}_k,\, \dot{y}_k,\, \dot{z}_k,\, \phi_k,\, \theta_k,\, \psi_k,\, \dot{\phi}_k,\, \dot{\theta}_k,\, \dot{\psi}_k]^T \\ \boldsymbol{u}_k &= [F_{z,k},\, \tau_{\phi,k},\, \tau_{\theta,k},\, \tau_{\psi,k}]^T \end{aligned} \tag{3.10}$$

To facilitate the design of the proposed TSPF scheme, the discrete-time state-space model of a quadrotor UAV with the wind effects can be described as

$$\boldsymbol{x}_k = \mathbf{f}(\boldsymbol{x}_{k-1},\, \boldsymbol{\xi}_k,\, \boldsymbol{u}_k) + \boldsymbol{\omega}_k^x \tag{3.11}$$

where $\mathbf{f}(\cdot)$ is the nonlinear discrete-time state-space equation and $\boldsymbol{\omega}_k^x$ denotes the process noise vector associated with the UAV states. The process noises are used to represent uncertainties of the quadrotor UAV dynamic model. The process noises are assumed as additive uncorrelated Gaussian noises with zero mean and a covariance Q_k^x.

To estimate wind vectors for a quadrotor UAV, the variations of wind velocities in three directions are modeled by random walk processes

$$\boldsymbol{\xi}_k = \boldsymbol{\xi}_{k-1} + \boldsymbol{\omega}_k^\xi \tag{3.12}$$

where $\boldsymbol{\omega}_k^\xi$ denotes the uncorrelated Gaussian noises with zero mean and a covariance Q_k^ξ. The wind variations are assumed to be homogeneous in three directions and have the same variance σ_ξ^2, i.e., $Q_k^\xi = \sigma_\xi^2 \mathrm{I}_3$.

The quadrotor UAV is assumed to be equipped with standard sensor suite to measure its position and attitude information. The standard sensor suite includes an IMU module, a magnetometer, and a GPS receiver. The IMU measures translational acceleration, angular velocity and attitude. The magnetometer provides the orientation. The GPS measures the translational velocity and position. It is assumed that the standard sensor suite can provide measurements of all defined states of the quadrotor UAV. The measurement equation is given by

$$\boldsymbol{z}_k = \mathbf{h}(\boldsymbol{x}_k) + \boldsymbol{v}_k \tag{3.13}$$

where $\mathbf{h}(\cdot)$ is the measurement equation, $\boldsymbol{v}_k$ denotes the associated measurement noise vector. The measurement noise is assumed as additive uncorrelated Gaussian noise with zero mean and a covariance R_k.

In brief, the nonlinear stochastic model of a quadrotor UAV can be described as

$$\begin{aligned} &\boldsymbol{\xi}_k \sim p(\boldsymbol{\xi}_k|\boldsymbol{\xi}_{k-1}) \\ &\boldsymbol{x}_k \sim p(\boldsymbol{x}_k|\boldsymbol{x}_{k-1},\, \boldsymbol{\xi}_k) \\ &\boldsymbol{z}_k \sim p(\boldsymbol{z}_k|\boldsymbol{x}_k) \end{aligned} \tag{3.14}$$

Note that for simplicity of description, the control input $\boldsymbol{u}_k$ is removed, i.e., $p(\boldsymbol{x}_k|\boldsymbol{x}_{k-1},\, \boldsymbol{\xi}_k)$ denotes $p(\boldsymbol{x}_k|\boldsymbol{x}_{k-1},\, \boldsymbol{\xi}_k,\, \boldsymbol{u}_k)$.

3.4.2 Two-Stage Particle Filter Design

Considering the problem of wind estimation from quadrotor motion, i.e., the estimate of $p(\boldsymbol{\xi}_k|\boldsymbol{z}_{1:k})$, the key is to estimate the posterior probability $p(\boldsymbol{\xi}_k|\boldsymbol{z}_{1:k})$, where $\boldsymbol{z}_{1:k} = \{\boldsymbol{z}_1, \cdots, \boldsymbol{z}_k\}$. However, there is no direct relationship between $\boldsymbol{\xi}_k$ and $\boldsymbol{z}_{1:k}$. It can be observed that $\boldsymbol{\xi}_k$ and $\boldsymbol{z}_{1:k}$ are related to $\boldsymbol{x}_{0:k}$. Therefore, $\boldsymbol{x}_{0:k}$ is used as an intermediate variable to build a relationship between $\boldsymbol{\xi}_k$ and $\boldsymbol{z}_{1:k}$ to solve the wind estimation problem.

$$\begin{aligned} p(\boldsymbol{\xi}_k|\boldsymbol{z}_{1:k}) &= \int p(\boldsymbol{\xi}_k,\, \boldsymbol{x}_{0:k}|\boldsymbol{z}_{1:k})\mathrm{d}\boldsymbol{x}_{0:k} \\ &= \int p(\boldsymbol{\xi}_k|\boldsymbol{x}_{0:k},\, \boldsymbol{z}_{1:k})p(\boldsymbol{x}_{0:k}|\boldsymbol{z}_{1:k})\mathrm{d}\boldsymbol{x}_{0:k} \\ &= \int p(\boldsymbol{\xi}_k|\boldsymbol{x}_{0:k})p(\boldsymbol{x}_{0:k}|\boldsymbol{z}_{1:k})\mathrm{d}\boldsymbol{x}_{0:k} \end{aligned} \tag{3.15}$$

In the above equation, the fact is used that $\boldsymbol{\xi}_k$ is independent on $\boldsymbol{z}_{1:k}$ once $\boldsymbol{x}_{0:k}$ is given, i.e., $p(\boldsymbol{\xi}_k|\boldsymbol{x}_{0:k},\, \boldsymbol{z}_{1:k}) = p(\boldsymbol{\xi}_k|\boldsymbol{x}_{0:k})$.

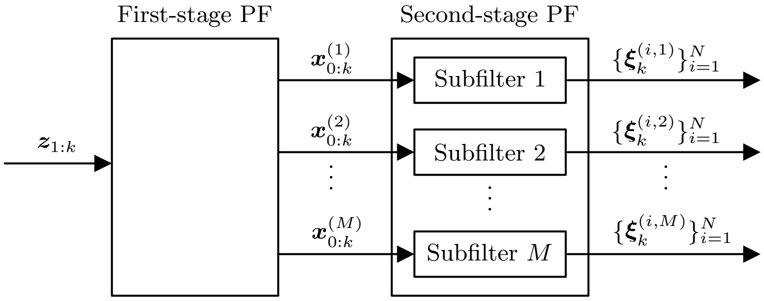

Figure 3.2: Structure of the two-stage particle filter

Fig. 3.2 shows the cascaded structure of the proposed two-stage particle filter, where M stands for the particle number of the first-stage particle filter, and N stands for the particle number of each subfilter in the second-stage particle filter. The first-stage particle filter can obtain a set of equally weighted particles $\{\boldsymbol{x}_{0:k}^{(j)}\}_{j=1}^M$ to approximate $p(\boldsymbol{x}_{0:k}|\boldsymbol{z}_{1:k})$ as

$$p(\boldsymbol{x}_{0:k}|\boldsymbol{z}_{1:k}) \approx \frac{1}{M}\sum_{j=1}^{M}\delta(\boldsymbol{x}_{0:k} - \boldsymbol{x}_{0:k}^{(j)}) \tag{3.16}$$

and the j-th subfilter in the second-stage particle filter can obtain a set of equally weighted particles $\{\boldsymbol{\xi}_k^{(i,j)}\}_{i=1}^N$ to approximate $p(\boldsymbol{\xi}_k|\boldsymbol{x}_{0:k}^{(j)})$ as

$$p(\boldsymbol{\xi}_k|\boldsymbol{x}_{0:k}^{(j)}) \approx \frac{1}{N}\sum_{i=1}^{N}\delta(\boldsymbol{\xi}_k - \boldsymbol{\xi}_k^{(i,j)}) \tag{3.17}$$

where $\delta(\cdot)$ is the Dirac delta mass. Then, $p(\boldsymbol{\xi}_k|\boldsymbol{z}_{1:k})$ can be approximated as

$$\begin{aligned}p(\boldsymbol{\xi}_k|\boldsymbol{z}_{1:k}) &= \int p(\boldsymbol{\xi}_k|\boldsymbol{x}_{0:k})p(\boldsymbol{x}_{0:k}|\boldsymbol{z}_{1:k})\mathrm{d}\boldsymbol{x}_{0:k} \\ &\approx \frac{1}{M}\sum_{j=1}^{M} p(\boldsymbol{\xi}_k|\boldsymbol{x}_{0:k}^{(j)}) \\ &\approx \frac{1}{MN}\sum_{i=1}^{N}\sum_{j=1}^{M}\delta(\boldsymbol{\xi}_k - \boldsymbol{\xi}_k^{(i,j)})\end{aligned} \tag{3.18}$$

To solve the estimating problem in a recursive fashion, $p(\boldsymbol{x}_{0:k}|\boldsymbol{z}_{1:k})$ and $p(\boldsymbol{\xi}_k|\boldsymbol{x}_{0:k}^{(j)})$ should be derived from $p(\boldsymbol{x}_{0:k-1}|\boldsymbol{z}_{1:k-1})$ and $p(\boldsymbol{\xi}_{k-1}|\boldsymbol{x}_{0:k-1}^{(j)})$, respectively.

The iterative calculation of $p(\boldsymbol{x}_{0:k}|\boldsymbol{z}_{1:k})$ can be accomplished by

$$\begin{aligned}p(\boldsymbol{x}_{0:k}|\boldsymbol{z}_{1:k}) &\propto p(\boldsymbol{x}_{0:k},\, \boldsymbol{z}_{k-1}|\boldsymbol{z}_{1:k-1}) \\ &= p(\boldsymbol{z}_k|\boldsymbol{x}_{0:k})p(\boldsymbol{x}_{0:k}|\boldsymbol{z}_{1:k-1}) \\ &= p(\boldsymbol{z}_k|\boldsymbol{x}_{0:k})\int p(\boldsymbol{x}_{0:k},\, \boldsymbol{x}_{0:k-1}|\boldsymbol{z}_{1:k-1})\mathrm{d}\boldsymbol{x}_{0:k-1} \\ &= p(\boldsymbol{z}_k|\boldsymbol{x}_{0:k})\int p(\boldsymbol{x}_{0:k}|\boldsymbol{x}_{0:k-1})p(\boldsymbol{x}_{0:k-1}|\boldsymbol{z}_{1:k-1})\mathrm{d}\boldsymbol{x}_{0:k-1}\end{aligned} \tag{3.19}$$

where the facts that $\boldsymbol{z}_k$ and $\boldsymbol{x}_{0:k}$ are independent on $\boldsymbol{z}_{1:k-1}$ given $\boldsymbol{x}_{0:k}$ and $\boldsymbol{x}_{0:k-1}$ are used, respectively. It is assumed that a set of equally weighted particles $\{\boldsymbol{x}_{0:k-1}^{(j)}\}_{j=1}^{M}$ are obtained at the time $k-1$. Substituting them into the above equation, $p(\boldsymbol{x}_{0:k}|\boldsymbol{z}_{1:k})$ can be approximated as

$$p(\boldsymbol{x}_{0:k}|\boldsymbol{z}_{1:k}) \approx p(\boldsymbol{z}_k|\boldsymbol{x}_{0:k})\frac{1}{M}\sum_{j=1}^{M} p(\boldsymbol{x}_{0:k}|\boldsymbol{x}_{0:k-1}^{(j)}) \tag{3.20}$$

Then, the calculation of $p(\boldsymbol{x}_{0:k}|\boldsymbol{x}_{0:k-1}^{(j)})$ can be given by

$$\begin{aligned}p(\boldsymbol{x}_{0:k}|\boldsymbol{x}_{0:k-1}^{(j)}) &= \int p(\boldsymbol{x}_{0:k},\, \boldsymbol{\xi}_k|\boldsymbol{x}_{0:k-1}^{(j)})\mathrm{d}\boldsymbol{\xi}_k \\ &= \int p(\boldsymbol{x}_{0:k}|\boldsymbol{\xi}_k, \boldsymbol{x}_{0:k-1}^{(j)})p(\boldsymbol{\xi}_k|\boldsymbol{x}_{0:k-1}^{(j)})\mathrm{d}\boldsymbol{\xi}_k\end{aligned} \tag{3.21}$$

It is assumed that $\boldsymbol{x}_{0:k-1}^{(j)}$ and the associated set of equally weighted particles $\{\boldsymbol{\xi}_{k-1}^{(i,j)}\}_{i=1}^{N}$ are given at the time $k-1$, $p(\boldsymbol{\xi}_k|\boldsymbol{x}_{0:k-1}^{(j)})$ can be approximated as

$$\begin{aligned}
p(\boldsymbol{\xi}_k|\boldsymbol{x}_{0:k-1}^{(j)}) &= \int p(\boldsymbol{\xi}_k,\, \boldsymbol{\xi}_{k-1}|\boldsymbol{x}_{0:k-1}^{(j)})\mathrm{d}\boldsymbol{\xi}_{k-1} \\
&= \int p(\boldsymbol{\xi}_k|\boldsymbol{\xi}_{k-1})p(\boldsymbol{\xi}_{k-1}|\boldsymbol{x}_{0:k-1}^{(j)})\mathrm{d}\boldsymbol{\xi}_{k-1} \\
&\approx \int p(\boldsymbol{\xi}_k|\boldsymbol{\xi}_{k-1})\frac{1}{N}\sum_{i=1}^{N}\delta(\boldsymbol{\xi}_{k-1}-\boldsymbol{\xi}_{k-1}^{(i,j)})\mathrm{d}\boldsymbol{\xi}_{k-1} \\
&=\frac{1}{N}\sum_{i=1}^{N}p(\boldsymbol{\xi}_k|\boldsymbol{\xi}_{k-1}^{(i,j)})
\end{aligned} \tag{3.22}$$

If a set of particles $\{\check{\boldsymbol{\xi}}_k^{(i,j)}\}_{i=1}^{N}$ are drawn from $p(\boldsymbol{\xi}_k|\boldsymbol{\xi}_{k-1}^{(i,j)})$, $p(\boldsymbol{\xi}_k|\boldsymbol{x}_{0:k-1}^{(j)})$ can be further approximated as

$$p(\boldsymbol{\xi}_k|\boldsymbol{x}_{0:k-1}^{(j)}) \approx \frac{1}{N}\sum_{i=1}^{N}\delta(\boldsymbol{\xi}_k-\check{\boldsymbol{\xi}}_k^{(i,j)}) \tag{3.23}$$

Substituting Eq. (3.23) into Eq. (3.21), the approximated particle representation of $p(\boldsymbol{x}_{0:k}|\boldsymbol{x}_{0:k-1}^{(j)})$ can be obtained by

$$\begin{aligned}
p(\boldsymbol{x}_{0:k}|\boldsymbol{x}_{0:k-1}^{(j)}) &\approx \int p(\boldsymbol{x}_{0:k}|\boldsymbol{\xi}_k, \boldsymbol{x}_{0:k-1}^{(j)})\frac{1}{N}\sum_{i=1}^{N}\delta(\boldsymbol{\xi}_k-\check{\boldsymbol{\xi}}_k^{(i,j)})\mathrm{d}\boldsymbol{\xi}_k \\
&=\frac{1}{N}\sum_{i=1}^{N}p(\boldsymbol{x}_{0:k}|\check{\boldsymbol{\xi}}_k^{(i,j)}, \boldsymbol{x}_{0:k-1}^{(j)})
\end{aligned} \tag{3.24}$$

Recalling Eq. (3.20), if $\{\check{\boldsymbol{x}}_k^{(j)}\}_{j=1}^{M}$ are drawn from $\frac{1}{N}\sum_{i=1}^{N}p(\boldsymbol{x}_k|\boldsymbol{x}_{k-1}^{(j)}, \check{\boldsymbol{\xi}}_k^{(i,j)})$, $p(\boldsymbol{x}_k|\boldsymbol{z}_{1:k})$ can be approximated as

$$p(\boldsymbol{x}_k|\boldsymbol{z}_{1:k}) \approx \sum_{j=1}^{M}w_{x,k}^{(j)}\delta(\boldsymbol{x}_k-\check{\boldsymbol{x}}_k^{(j)}) \tag{3.25}$$

where the normalized weight is

$$w_{x,k}^{(j)} = \frac{p(\boldsymbol{z}_k|\check{\boldsymbol{x}}_k^{(j)})}{\sum_{m=1}^{M} p(\boldsymbol{z}_k|\check{\boldsymbol{x}}_k^{(m)})} \tag{3.26}$$

Resampling particles with the weights, the equally weighted particles $\{\boldsymbol{x}_k^{(j)}\}_{j=1}^{M}$ can be obtained. Therefore, the approximation of $p(\boldsymbol{x}_{0:k}|\boldsymbol{z}_{1:k})$ satisfies Eq. (3.16).

The iterative calculation of $p(\boldsymbol{\xi}_k|\boldsymbol{x}_{0:k}^{(j)})$ can be accomplished by

$$\begin{aligned} p(\boldsymbol{\xi}_k|\boldsymbol{x}_{0:k}^{(j)}) =& \frac{p(\boldsymbol{x}_k^{(j)}, \boldsymbol{\xi}_k|\boldsymbol{x}_{0:k-1}^{(j)})}{p(\boldsymbol{x}_k^{(j)}|\boldsymbol{x}_{0:k-1}^{(j)})} \\ &\propto p(\boldsymbol{x}_k^{(j)}|\boldsymbol{\xi}_k, \boldsymbol{x}_{0:k-1}^{(j)}) p(\boldsymbol{\xi}_k|\boldsymbol{x}_{0:k-1}^{(j)}) \end{aligned} \tag{3.27}$$

Substituting Eq. (3.23) into the above equation, $p(\boldsymbol{\xi}_k|\boldsymbol{x}_{0:k}^{(j)})$ can be approximated as

$$p(\boldsymbol{\xi}_k|\boldsymbol{x}_{0:k}^{(j)}) \approx \sum_{i=1}^{N} w_{\xi,k}^{(i,j)} \delta(\boldsymbol{\xi}_k - \check{\boldsymbol{\xi}}_k^{(i,j)}) \tag{3.28}$$

where the normalized weight is

$$w_{\xi,k}^{(i,j)} = \frac{p(\boldsymbol{x}_k^{(j)}|\boldsymbol{x}_{k-1}^{(j)}, \check{\boldsymbol{\xi}}_k^{(i,j)})}{\sum_{n=1}^{N} p(\boldsymbol{x}_k^{(j)}|\boldsymbol{x}_{k-1}^{(j)}, \check{\boldsymbol{\xi}}_k^{(n,j)})} \tag{3.29}$$

Resampling particles with the weights, the equally weighted particles $\{\boldsymbol{\xi}_k^{(i,j)}\}_{i=1}^{N}$ can be obtained. Therefore, the approximation of $p(\boldsymbol{\xi}_k|\boldsymbol{x}_{0:k}^{(j)})$ satisfies Eq. (3.17).

Finally, according to Eq. (3.18), the estimate of $\boldsymbol{\xi}_k$ given $\boldsymbol{z}_{1:k}$ can be calculated as

$$\hat{\boldsymbol{\xi}}_k \approx \frac{1}{MN} \sum_{i=1}^{N} \sum_{j=1}^{M} \boldsymbol{\xi}_k^{(i,j)} \tag{3.30}$$

As a byproduct, the estimate of $\boldsymbol{x}_k$ can be calculated as

$$\hat{\boldsymbol{x}}_k \approx \frac{1}{M} \sum_{j=1}^{M} \boldsymbol{x}_k^{(j)} \tag{3.31}$$

To better understand the proposed two-stage particle filter for wind estimation, the pseudo code is given in Algorithm 1.

Algorithm 1: The proposed two-stage particle filter for wind estimation

```
Input: Measurement of UAV state $\boldsymbol{z}_k$
Output: Estimate of wind vector $\hat{\boldsymbol{\xi}}_k$
Initialize state particles $\boldsymbol{x}_0^{(i)} \sim p(\boldsymbol{x}_0)$ and wind vector particles $\boldsymbol{\xi}_0^{(i,j)} \sim p(\boldsymbol{\xi}_0)$;
for $k \leftarrow 1$ to $N_{iterative}$ do
    Sample $\breve{\boldsymbol{\xi}}_k^{(i,j)} \sim p(\boldsymbol{\xi}_k | \boldsymbol{\xi}_{k-1}^{(i,j)})$ ;
    Sample $\{\breve{\boldsymbol{x}}_k^{(j)}\}_{j=1}^{M} \sim \frac{1}{N} \sum_{i=1}^{N} p(\boldsymbol{x}_k | \boldsymbol{x}_{k-1}^{(j)}, \breve{\boldsymbol{\xi}}_k^{(i,j)})$;
    $w_{x,k}^{(j)} \leftarrow \frac{p(\boldsymbol{z}_k | \breve{\boldsymbol{x}}_k^{(j)})}{\sum_{m=1}^{M} p(\boldsymbol{z}_k | \breve{\boldsymbol{x}}_k^{(m)})}$;
    Resample $\{\boldsymbol{x}_k^{(j)}\}_{j=1}^{M}$ from $\{\breve{\boldsymbol{x}}_k^{(j)}\}_{i=1}^{M}$ with weight $\{w_{x,k}^{(j)}\}_{j=1}^{M}$;
    foreach subfilter $j$ do
        Reselect $\{\breve{\boldsymbol{\xi}}_k^{(i,j)}\}_{i=1}^{N}$ according to the resampled $\boldsymbol{x}_k^{(j)}$;
        $w_{\xi,k}^{(i,j)} \leftarrow \frac{p(\boldsymbol{x}_k^{(j)} | \boldsymbol{x}_{k-1}^{(j)}, \breve{\boldsymbol{\xi}}_k^{(i,j)})}{\sum_{n=1}^{N} p(\boldsymbol{x}_k^{(j)} | \boldsymbol{x}_{k-1}^{(j)}, \breve{\boldsymbol{\xi}}_k^{(n,j)})}$;
        Resample $\{\boldsymbol{\xi}_k^{(i,j)}\}_{i=1}^{N}$ from $\{\tilde{\boldsymbol{\xi}}_k^{(i,j)}\}_{i=1}^{N}$ with weight $\{w_{\xi,k}^{(i,j)}\}_{i=1}^{N}$;
    end
    Estimate $\hat{\boldsymbol{\xi}}_k \approx \frac{1}{MN} \sum_{i=1}^{N} \sum_{j=1}^{M} \boldsymbol{\xi}_k^{(i,j)}$
end
```

3.5 Simulation Results

In the simulation, the proposed algorithm is used to estimate states and winds for a quadrotor UAV. The motion of the quadrotor is simulated based on the dynamic model (2.11). The parameters of the model are listed in Table 2.1. The process and measurement noises are listed in Tables 2.2 and 2.3, respectively. The noises are assumed to be constant with time. The random-walk wind model parameter is set as $\sigma_\xi^2 = 0.05\,(\mathrm{m/s})^2$. The particle numbers of the first-stage and second-stage particle filters are set as $M = 500$ and $N = 100$. The simulation time interval is set as $T_s = 0.02\,\mathrm{s}$.

In order to demonstrate the effectiveness and performance of the proposed method, different scenarios of wind conditions have been rendered to the quadrotor UAV as follows:

(1) Estimation of constant wind from quadrotor motion;

(2) Estimation of wind gust from quadrotor motion;

(3) Estimation of wind turbulence from quadrotor motion.

To compare the performances of the proposed two-stage particle filter (TSPF) algorithm and the wind triangle (WT) algorithm, the simulations are conducted to estimate wind vectors from a quadrotor in hover. The wind triangle algorithm [32] depends on the assumption that a quadrotor UAV can quickly adjust its attitude to withstand the wind drag. By using the wind triangle algorithm, the horizontal wind speed and direction for a quadotor UAV are estimated from the measurements of linear velocities and Euler angles.

3.5.1 Estimation of Constant Wind from Quadrotor Motion

To evaluate the performances of the TSPF and WT algorithms for the constant wind estimation, a quadrotor UAV is simulated to hover in a $[3,\ 4,\ 0]^T\ \mathrm{m/s}$ constant wind. The two algorithms are used to extract the wind vectors from quadrotor motion. Fig. 3.3 shows the estimation results of the $[3,\ 4,\ 0]^T\ \mathrm{m/s}$ constant wind from a quadrotor UAV in hover. It can be seen that the wind estimation results provided by the proposed TSPF algorithm are comparable to those provided by the WT algorithm, since the quadrotor UAV is in the steady-state condition after $2\,\mathrm{s}$. The wind rose diagrams of the lateral wind estimation indicate that the proposed TSPF can provide accurate wind speed and direction estimation of the lateral constant wind.

To compare the accuracy of the two algorithms for the constant wind estimation, the mean absolute error (MAE) and root-mean-squared error (RMSE) are calculated for the TSPF and WT algorithms, respectively. The lateral wind vectors are estimated for three different constant wind vectors, including $\boldsymbol{\xi} = [3,\ 4,\ 0]^T\,\mathrm{m/s}$, $\boldsymbol{\xi} = [4,\ -3,\ 0]^T\,\mathrm{m/s}$ and $\boldsymbol{\xi} = [3,\ 4,\ 5]^T\,\mathrm{m/s}$. Table 3.1 gives the comparison of MAE and RMSE for the constant wind estimation from a quadrotor UAV in hover. The proposed TSPF algorithm obtains better wind estimation accuracy than the WT algorithm in all three cases. It should be noted that the WT algorithm results in large errors of the lateral wind estimation when the vertical wind component is nonzero. This is because the wind drag generated by the vertical wind component changes the steady-state condition of the quadrotor UAV which the WT algorithm relies on. The proposed TSPF algorithm can provide a three-dimensional wind estimation and separate the lateral and vertical wind estimation to avoid the impact of vertical wind component on the lateral wind estimation.

Table 3.1: Comparison of MAE and RMSE for constant wind estimation from a quadrotor UAV in hover

$\boldsymbol{\xi}$ (m/s)	$[3,\ 4,\ 0]^T$		$[4,\ -3,\ 0]^T$		$[3,\ 4,\ 5]^T$	
	TSPF	WT	TSPF	WT	TSPF	WT
MAE of $\hat{\xi}_x$ (m/s)	0.1242	0.1222	0.1160	0.1305	0.1190	0.2622
MAE of $\hat{\xi}_y$ (m/s)	0.1151	0.1374	0.1203	0.1292	0.1123	0.3368
RMSE of $\hat{\xi}_x$ (m/s)	0.1548	0.2406	0.1446	0.3099	0.1484	0.3261
RMSE of $\hat{\xi}_y$ (m/s)	0.1440	0.3255	0.1515	0.2497	0.1421	0.4279

3.5.2 Estimation of Wind Gust from Quadrotor Motion

To evaluate the performance of the TSPF and WT algorithms for the wind gust estimation, the quadrotor UAV is simulated to encounter two types of wind gusts, respectively. According to the endurance time, the two types of gust scenarios are the slowly-changing wind gust and quickly-changing wind gust, as listed in Table 3.2. For the slowly-changing

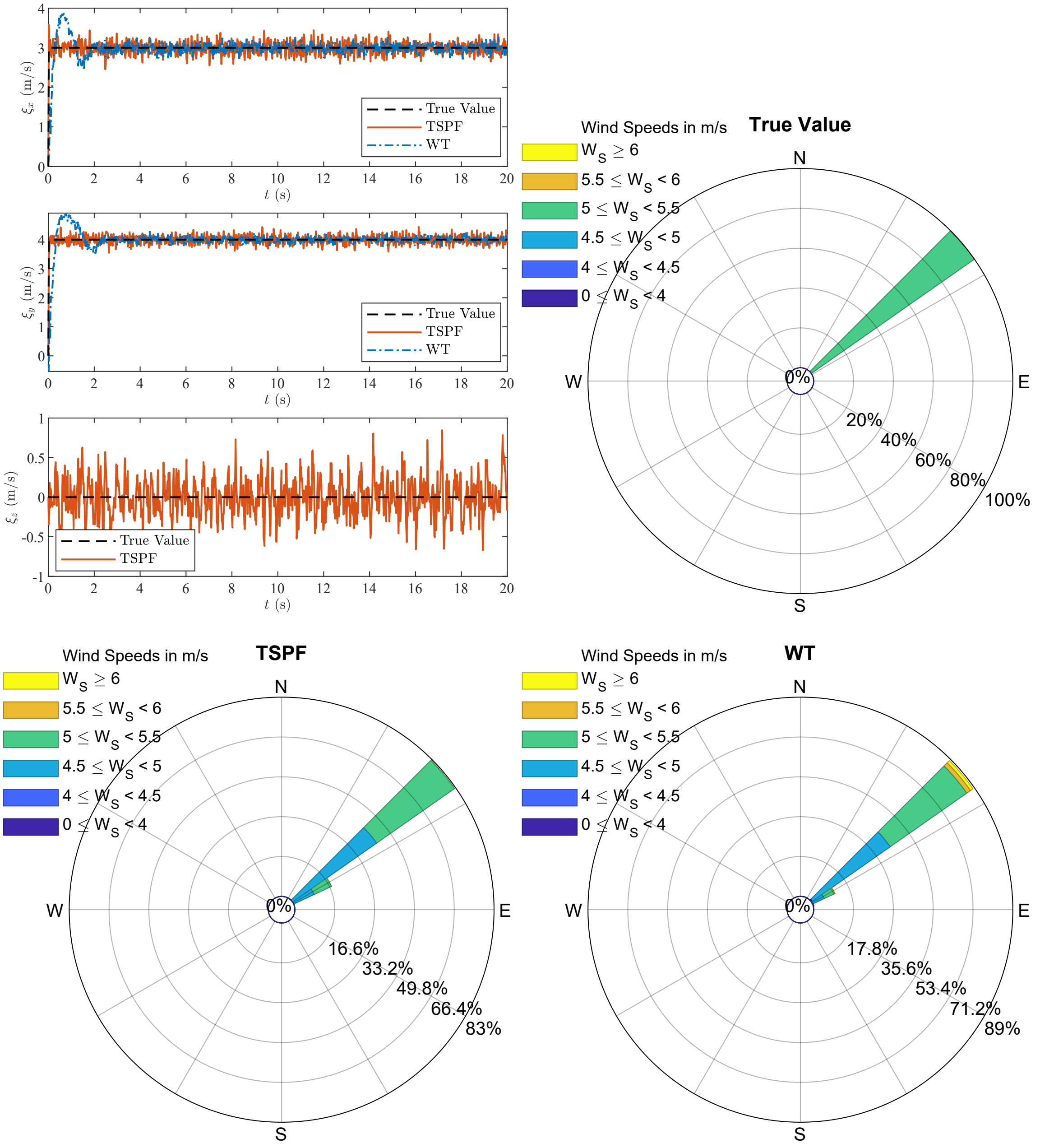

Figure 3.3: Estimation results of a constant wind of $[3,\ 4,\ 0]^T$ m/s from a quadrotor UAV in hover

gust, the endurance time is set as $t_g = 10\,\mathrm{s}$. For the quickly-changing gust, the endurance time is set as $t_g = 4\,\mathrm{s}$. Both wind gusts start at $t_{gs} = 4\,\mathrm{s}$ and have the peak value of $v_{gm} = [4,\ 3,\ 2]^T\ \mathrm{m/s}$.

Fig. 3.4 demonstrates the estimation results of the slowly-changing wind gust from a quadrotor UAV in hover. It can be seen that the proposed TSPF algorithm and the WT algorithm can effectively estimate the slow changes of the wind gust. The wind estimation provided by the two algorithm gradually increase or decrease with the slow changes of the wind gust. For the lateral wind speed and direction estimation, the two algorithms obtain comparable results to the true value.

Fig. 3.5 demonstrates the estimation results of the quickly-changing wind gust from a quadrotor UAV in hover. Although the WT algorithm results in more large errors, the proposed TSPF algorithm can still produce reliable estimation of the quickly-changing wind gust. Because the WT algorithm relies on the assumption that tilt angles directly corresponds to the relatively air speed vector in the steady-state condition, there is a delay in the wind estimation when the controller drastically responds to the sudden changes of the wind gust. Compared with the WT algorithm, the proposed TSPF algorithm can extract winds from the information of quadrotor motion, including the position, attitude and controller inputs.

Table 3.2: Wind gust scenarios in the simulation

Wind gust scenario	v_{gm} (m/s)	t_{gs} (s)	t_g (s)
Slowly-change	$[4,\ 3,\ 2]^T$	4	10
Quickly-change	$[4,\ 3,\ 2]^T$	4	4

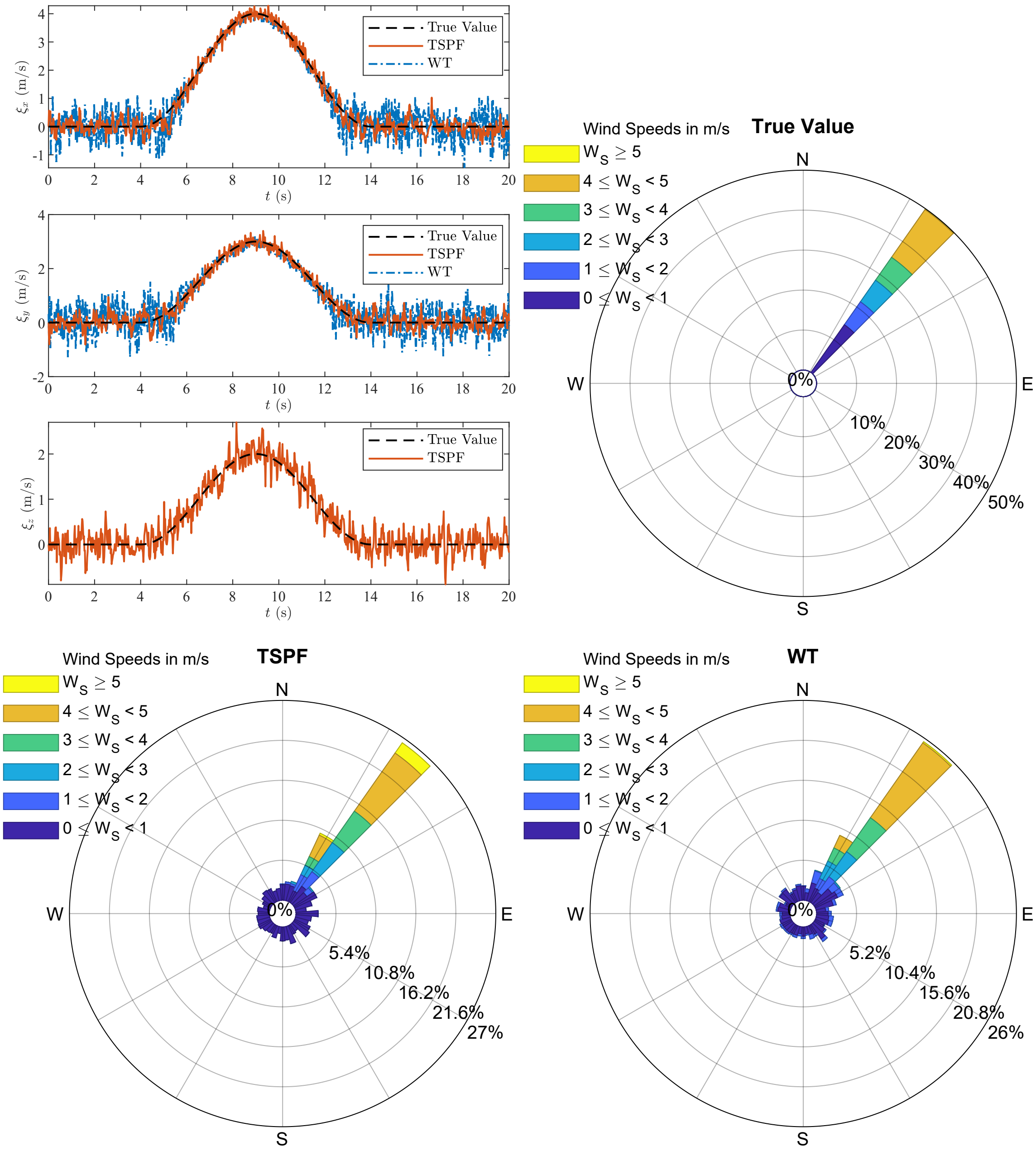

Figure 3.4: Estimation results of a slowly-changing wind gust from a quadrotor UAV in hover

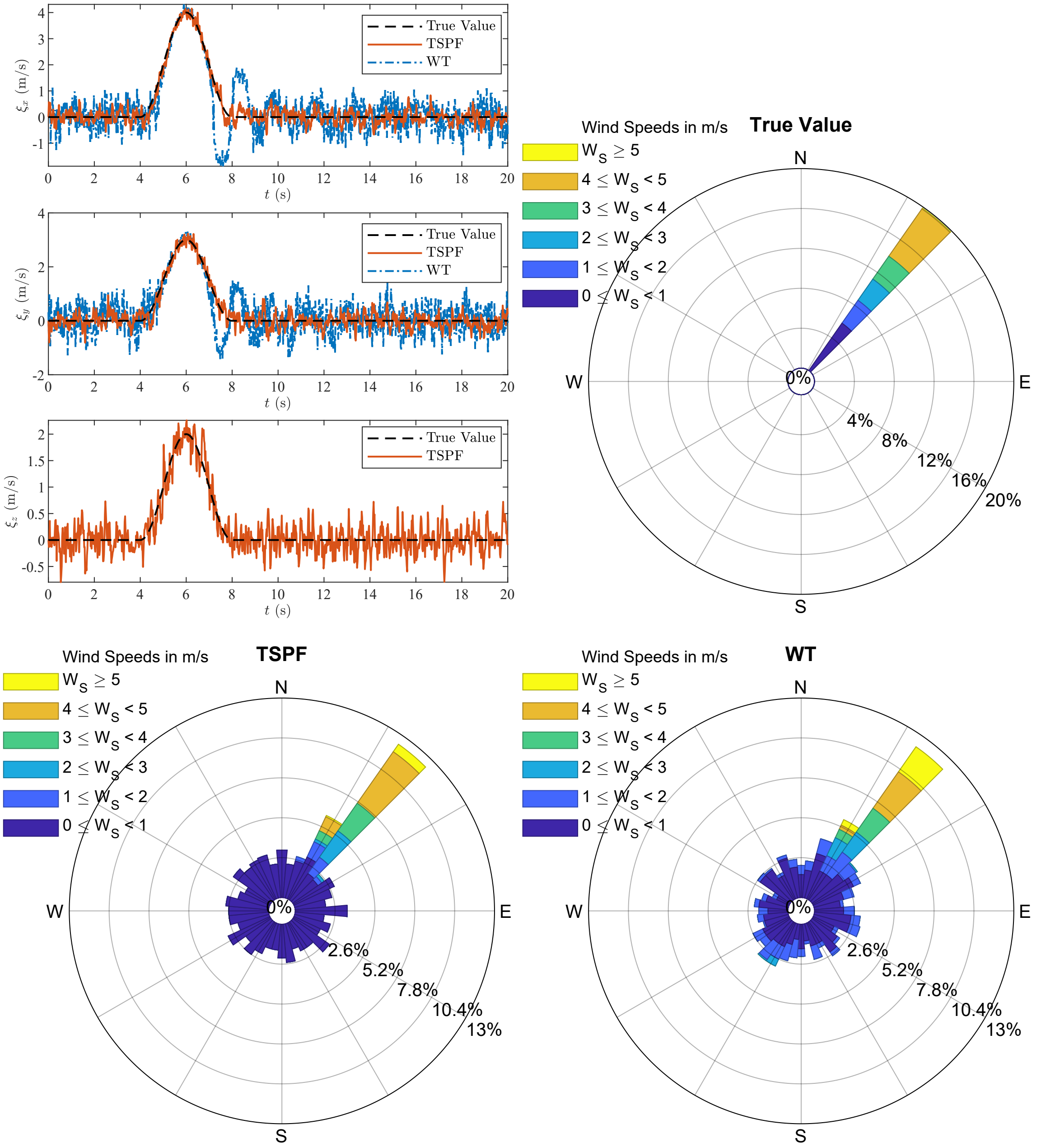

Figure 3.5: Estimation results of a quickly-changing wind gust from a quadrotor UAV in hover

3.5.3 Estimation of Wind Turbulence from Quadrotor Motion

To evaluate the performance of the TSPF and WT algorithms for the wind turbulence estimation, the quadrotor UAV is simulated to hover in a $[3,\ 4,\ 0]^T\,\mathrm{m/s}$ mean wind turbulence with the turbulence intensity of $\sigma_{u,v,w} = [1.54,\ 1.54,\ 0.97]^T$. Fig. 3.6 demonstrates the estimation results of the Dryden turbulence from the quadrotor UAV in hover. It can be seen that the proposed TSPF algorithm can correctly capture the high frequency component of wind turbulence.

To compare the accuracy of the two algorithms for the turbulence estimation, the MAE and RMSE are calculated for the two algorithms. Table 3.3 gives the comparison of MAE and RMSE for the $[3,\ 4,\ 0]^T\,\mathrm{m/s}$ mean Dryden turbulence with different turbulence intensities of $\sigma_{u,v,w} = [0.93,\ 0.93,\ 0.58]^T$, $\sigma_{u,v,w} = [1.24,\ 1.24,\ 0.78]^T$, and $\sigma_{u,v,w} = [1.54,\ 1.54,\ 0.97]^T$. In almost all cases, the TSPF algorithm has lower MAE and RMSE than the WT algorithm. This fact indicates that the proposed TSPF algorithm outperforms the WT algorithm in the wind turbulence estimation.

Table 3.3: Comparison of MAE and RMSE for a $[3,\ 4,\ 0]^T\,\mathrm{m/s}$ mean Dryden turbulence estimation from a quadrotor UAV in hover

$\sigma_{u,v,w}$ (m/s)	$[0.93,\ 0.93,\ 0.58]^T$		$[1.24,\ 1.24,\ 0.78]^T$		$[1.54,\ 1.54,\ 0.97]^T$	
	TSPF	WT	TSPF	WT	TSPF	WT
MAE of $\hat{\xi}_x$ (m/s)	0.1263	0.1337	0.1239	0.1408	0.1264	0.1489
MAE of $\hat{\xi}_y$ (m/s)	0.1170	0.1436	0.1167	0.1479	0.1192	0.1532
RMSE of $\hat{\xi}_x$ (m/s)	0.1634	0.2500	0.1611	0.2551	0.1615	0.2611
RMSE of $\hat{\xi}_y$ (m/s)	0.1518	0.3257	0.1521	0.3269	0.1562	0.3285

To demonstrate the efficiency of the proposed TSPF algorithm to sensor noise, the simulation comparison is conducted to estimate the $[3,\ 4,\ 0]^T\,\mathrm{m/s}$ mean Dryden turbulence under different signal-noise ratio (SNR). The comparisons are given in Table 3.4. The MAE and RMSE are compared under $10\,\mathrm{dB}$, $20\,\mathrm{dB}$ and $30\,\mathrm{dB}$. With the increased power of the noise, the estimation errors of the proposed TSPF algorithm increase smaller than those of

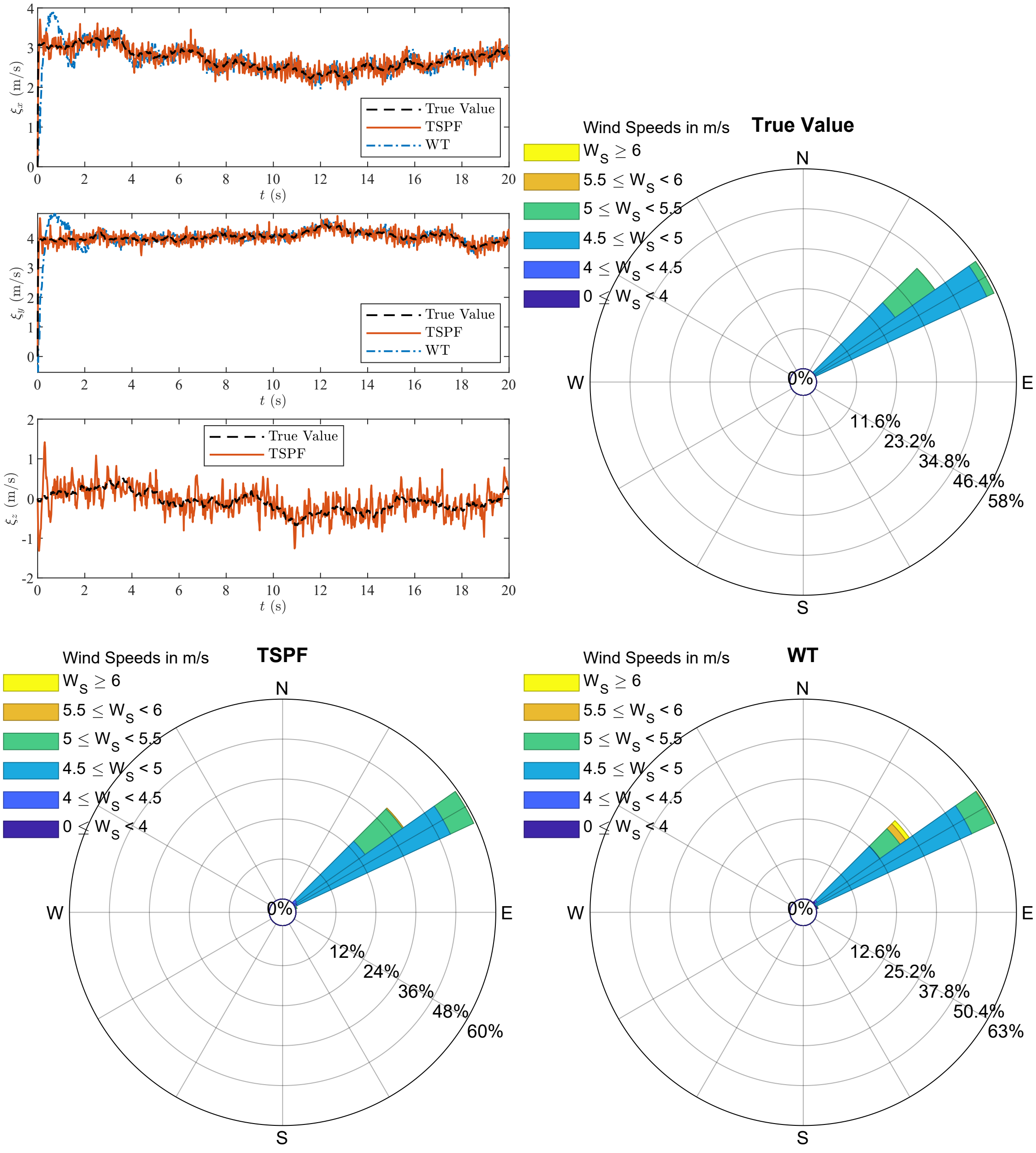

Figure 3.6: Estimation results of a $[3,\ 4,\ 0]^T$ m/s mean Dryden turbulence with $\sigma_{u,v,w} = [1.54,\ 1.54,\ 0.97]^T$ from a quadrotor UAV in hover

the WT algorithm. This indicates that the proposed TSPF algorithm outperforms the WT algorithm in dealing with the sensor noises to estimate the wind vectors from quadrotor motion.

Table 3.4: Comparison of MAE and RMSE for a $[3,\ 4,\ 0]^T$ m/s mean Dryden turbulence estimation from a quadrotor UAV in hover under different SNRs

SNR (dB)	10		20		30	
	TSPF	WT	TSPF	WT	TSPF	WT
MAE of $\hat{\xi}_x$ (m/s)	0.1775	0.6325	0.1390	0.2116	0.1226	0.0963
MAE of $\hat{\xi}_y$ (m/s)	0.1859	0.7498	0.1423	0.2450	0.1292	0.1000
RMSE of $\hat{\xi}_x$ (m/s)	0.2236	0.7981	0.1742	0.2695	0.1570	0.1207
RMSE of $\hat{\xi}_y$ (m/s)	0.2328	0.9739	0.1814	0.3088	0.1662	0.1266

3.6 Summary

This chapter develops a two-stage particle filter-based scheme to estimate wind vectors from quadrotor motion. To build a relationship between wind vectors and motion measurements, the state of quadrotor UAV is introduced as an intermediate variable. By using a cascaded structure, the states of quadrotor UAV are estimated from the motion measurements in the first-stage particle filter, and wind vectors are calculated based on the estimated states in the second-stage particle filter. To evaluate the effectiveness, the proposed wind estimation algorithm is compared with the wind triangle algorithm in estimating constant winds, wind gust, and Dryden turbulences. Simulation results demonstrate the outperformance of the proposed algorithm to extract three dimensional wind vectors from quadrotor motion.

Chapter 4

Active Wind Rejection Control of Quadrotor UAVs

4.1 Problem Formulation

Wind behaviors have considerable impacts on the safety and reliability of UAVs when performing outdoor tasks. The application of UAVs requires the precise and agile control of these vehicles in the presence of strong and unpredictable winds. For example, UAVs, which are employed in forest fire detection, monitoring, and fighting tasks, need to accurately track a planned trajectory to collect fire information across the hazardous fire region against unknown winds. External wind disturbances generate unexpected forces and moments acting on the UAV dynamics that degrade the performance of UAVs and even result in serious accidents if appropriate reactions are not promptly activated to attenuate the wind effects. In particular, quadrotor UAVs are more sensitive to those external disturbances due to their small size. Therefore, the wind rejection control of UAVs required to be investigated to ensure the stability and performance of tracking desired trajectories against wind disturbances.

In most cases, the wind disturbances and modeling uncertainties are generally lumped together and the observer-based control methods are adopted to suppress the total disturbances, relying on the high-frequency and low-latency control. These control methods are proposed based on the deterministic system but are quite sensitive to the stochastic process and measurement noises. Moreover, the precise control of a quadrotor UAV in unknown wind environments requires an accurate and prompt perception of the ambient winds to quickly compensate for the wind effects.

This thesis proposes the control scheme based on the nonsingular terminal sliding mode control [91, 52] to realize the control of quadrotor UAVs in the presence of unknown wind. The proposed control strategy mainly contains the outer-loop control and the inner-loop control. The outer-loop control is developed to track the desired trajectories and attenuate wind effects, while the inner-loop control is developed to stabilize the attitude of the quadrotor UAV. By using the NTSMC, the proposed control strategy can avoid the singularity problem and guarantee the finite-time convergence of the position and attitude of the quadrotor UAV towards the desired trajectories.

Based on the wind estimation produced by the wind estimator, the proposed wind rejection control scheme can actively compensate for wind effects acting on the quadrotor UAVs to maintain UAV performances in the presence of unexpected wind disturbances. Different from the general disturbance observer [42] that lumps together the disturbance and uncertainty, the proposed control scheme mainly focuses on the wind effects and can actively attenuate wind disturbances based on the explicit wind estimation.

4.2 Sliding Mode Control

Sliding mode control is an effective, robust control strategy that is inherently insensitive to parameter variations, model uncertainties, and external disturbances. As a particular kind of variable structure control system, sliding model control is composed of independent structures with different properties and a switching logic between them. The basic idea of sliding mode control is to design an appropriate sliding surface and a control law to force the system states onto this surface in a finite time [92].

To introduce the design of sliding mode control, a nonlinear system is modeled as

$$\dot{x}(t) = f(x,\, u,\, t) \tag{4.1}$$

where $x(t) \in \mathbb{R}^n$ denotes the state vector and $u(t) \in \mathbb{R}^m$ denotes the control vector.

A sliding surface is designed as

$$s(x) = 0 \tag{4.2}$$

where $s(x)$ is the switching function. The switching function usually has the same order as the control vector, i.e., $s(x) \in \mathbb{R}^m$, which is constructed as

$$s(x) = [s_1(x),\, s_2(x),\, \cdots,\, s_m(x)]^T \tag{4.3}$$

The design of the sliding mode surface should assure the stability of the dynamics with some specified performances, such as disturbance rejection and tracking the desired trajectory.

Then, a discontinuous control law $u(t) = [u_1(t),\, u_2(t),\, \cdots,\, u_m(t)]^T$ is designed as

$$u_i(t) = \begin{cases} u_i^+(t) & s_i(x) > 0 \\ u_i^-(t) & s_i(x) < 0 \end{cases} \tag{4.4}$$

where $i = 1, \cdots, m$ and $u_i^+(t) \neq u_i^-(t)$.

The control law is designed to guarantee that the system state trajectory can be driven onto the sliding surface in a finite time and maintained on it for all subsequent time, which is the so-called reachability condition. In case of a single input system, the reachability condition can be summarized as

$$\begin{aligned} \lim_{s\to 0^+} \dot{s} < 0 \\ \lim_{s\to 0^-} \dot{s} > 0 \end{aligned} \tag{4.5}$$

or, equivalently

$$s\dot{s} < 0 \tag{4.6}$$

To ensure that the system state trajectory can reach the sliding surface in a finite time in the face of disturbances, the η-reachability condition [93] is given by

$$s\dot{s} \le -\eta |s| \tag{4.7}$$

where η is a small positive constant.

4.3 Active Wind Rejection Control of a Quadrotor UAV

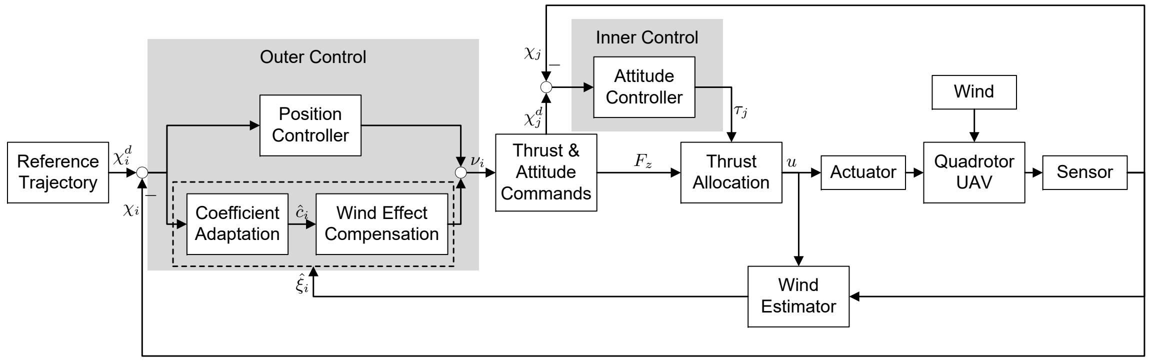

Figure 4.1: Framework of the proposed wind rejection control strategy of a quadrotor UAV

A hierarchical control system is designed for a quadrotor UAV to track the desired trajectories and stabilize the attitude in the presence of wind. The framework of the proposed control strategy is illustrated in Fig. 4.1. The outer-loop control combines the signals of position controller and adaptive wind effect compensation to generate virtual control inputs for the trajectory tracking, while the inner-loop control produces the control torques τ_j for the attitude stabilization. By using the proposed control strategy, the wind disturbance is attenuated via the adaptive wind effect compensation scheme.

4.3.1 Outer-loop Control

The outer-loop control strategy is designed to track the desired trajectories. Consider the translational dynamics of the quadrotor UAV subject to wind disturbances

$$\begin{aligned}\ddot{x} =& -\frac{1}{m}(\cos\phi\sin\theta\cos\psi+\sin\phi\sin\psi)F_z\\ &+\frac{1}{m}C_{dxy}(\xi_x-\dot{x})\sqrt{(\xi_x-\dot{x})^2+(\xi_y-\dot{y})^2}+\frac{d_x}{m}\\ \ddot{y} =& -\frac{1}{m}(\cos\phi\sin\theta\sin\psi-\sin\phi\cos\psi)F_z\\ &+\frac{1}{m}C_{dxy}(\xi_y-\dot{y})\sqrt{(\xi_x-\dot{x})^2+(\xi_y-\dot{y})^2}+\frac{d_y}{m}\\ \ddot{z} =& -\frac{1}{m}(\cos\phi\cos\theta)F_z+g+\frac{1}{m}C_{dz}(\xi_z-\dot{z})+\frac{d_z}{m}\end{aligned} \tag{4.8}$$

where d_i for $i \in \{x,\ y,\ z\}$ represents the lumped disturbance of the translational dynamics which are assumed to be unknown but bounded, i.e., $|d_i| \leq D_i$.

The quadrotor UAV is defined as an underactuated system, because the number of outputs is larger than that of control inputs. To solve this underactuating problem, virtual control inputs are defined as

$$\begin{aligned}\nu_x &= -(\cos\phi\sin\theta\cos\psi+\sin\phi\sin\psi)F_z\\ \nu_y &= -(\cos\phi\sin\theta\sin\psi-\sin\phi\cos\psi)F_z\\ \nu_z &= -(\cos\phi\cos\theta)F_z\end{aligned} \tag{4.9}$$

where ν_i for $i \in \{x,\ y,\ z\}$ denotes the virtual control inputs.

By recalling Eq. (4.8), the control-oriented model can be obtained as

$$\begin{aligned}\dot{\chi}_{i,1} &= \chi_{i,2}\\ \dot{\chi}_{i,2} &= G_i + h_i(\nu_i + c_i f_i + d_i)\end{aligned} \tag{4.10}$$

where

$$\begin{aligned}\chi_{x,1} &= x\\ \chi_{y,1} &= y\\ \chi_{z,1} &= z\end{aligned} \tag{4.11}$$

$$\begin{aligned}\chi_{x,2} &= \dot{x}\\ \chi_{y,2} &= \dot{y}\\ \chi_{z,2} &= \dot{z}\end{aligned} \tag{4.12}$$

$$\begin{aligned}c_x &= c_y = C_{dxy}\\ c_z &= C_{dz}\end{aligned} \tag{4.13}$$

$$\begin{aligned}f_x &= (\xi_x - \dot{x})\sqrt{(\xi_x - \dot{x})^2 + (\xi_y - \dot{y})^2}\\ f_y &= (\xi_y - \dot{y})\sqrt{(\xi_x - \dot{x})^2 + (\xi_y - \dot{y})^2}\\ f_z &= (\xi_z - \dot{z})\end{aligned} \tag{4.14}$$

$$\begin{aligned}G_x &= G_y = 0\\ G_z &= g\end{aligned} \tag{4.15}$$

$$h_x = h_y = h_z = \frac{1}{m} \tag{4.16}$$

Let χ_i^d for $i \in \{x,\, y,\, z\}$ denote the desired trajectory. Then, the tracking error related to position is defined as

$$\tilde{\chi}_i = \chi_{i,1} - \chi_i^d \tag{4.17}$$

and its corresponding derivative is given by

$$\dot{\tilde{\chi}}_i = \dot{\chi}_{i,1} - \dot{\chi}_i^d = \chi_{i,2} - \dot{\chi}_i^d \tag{4.18}$$

By combining Eqs. (4.10) and (4.18), the error dynamics can be obtained as

$$\begin{aligned}\ddot{\tilde{\chi}}_i =&\dot{\chi}_{i,2} - \ddot{\chi}_i^d \\ =&G_i + h_i(\nu_i + c_i f_i + d_i) - \ddot{\chi}_i^d\end{aligned} \tag{4.19}$$

Introduce the following nonsingular terminal sliding-mode surface [91]:

$$s_i = \tilde{\chi}_i + \frac{1}{\beta_i}\dot{\tilde{\chi}}_i^{\frac{p_i}{q_i}} \tag{4.20}$$

where β_i, p_i and q_i are positive design parameters. p_i and q_i are positive odd numbers, which satisfies $1 < \frac{p_i}{q_i} < 2$.

By differentiating Eq. (4.20) with respect to time, the expression can be obtained as

$$\begin{aligned}\dot{s}_i =&\dot{\tilde{\chi}}_i + \frac{1}{\beta_i}\frac{p_i}{q_i}\dot{\tilde{\chi}}_i^{\frac{p_i}{q_i}-1}\ddot{\tilde{\chi}}_i \\ =&\dot{\tilde{\chi}}_i + \frac{1}{\beta_i}\frac{p_i}{q_i}\dot{\tilde{\chi}}_i^{\frac{p_i}{q_i}-1}[G_i + h_i(\nu_i + c_i f_i + d_i) - \ddot{\chi}_i^d]\end{aligned} \tag{4.21}$$

Remark 4.1 *Because p_i and q_i are odd numbers, if $\dot{\tilde{\chi}}_i \neq 0$, then $\dot{\tilde{\chi}}_i^{\frac{p_i}{q_i}-1} > 0$.*

To allow the sliding variable to reach the designated sliding surface and then remain in close proximity to the sliding surface, the position control law can be designed as the following form:

$$\nu_i = \nu_i^{\text{eq}} + \nu_i^{\text{dis}} \tag{4.22}$$

where ν_i^{eq} is the equivalent control part to stabilize the ideal system without uncertainties and disturbances, and ν_i^{dis} is the discontinuous control part to compensating for the perturbations and disturbances.

Without considering the wind effects, the equivalent control part is designed by solving the following equation:

$$\dot{s}_i = \dot{\tilde{\chi}}_i + \frac{1}{\beta_i}\frac{p_i}{q_i}\dot{\tilde{\chi}}_i^{\frac{p_i}{q_i}-1}(G_i + h_i\nu_i - \ddot{\chi}_i^d) = 0 \tag{4.23}$$

where the disturbance term d_i is omitted in this case.

Then, the equivalent control ν_i^{eq} is obtained as

$$\nu_i^{\text{eq}} = -\frac{1}{h_i}(\beta_i\frac{q_i}{p_i}\dot{\tilde{\chi}}_i^{2-\frac{p_i}{q_i}} + G_i - \ddot{\chi}_i^d) \tag{4.24}$$

The discontinuous control part to cope with the perturbations is designed as

$$\nu_i^{\text{dis}} = -\eta_i \text{sign}(s_i) \tag{4.25}$$

where $\eta_i > D_i$ is positive design parameters.

In this way, without considering the wind effects, the outer-loop control law is designed as

$$\nu_i = -\frac{1}{h_i}(\beta_i\frac{q_i}{p_i}\dot{\tilde{\chi}}_i^{2-\frac{p_i}{q_i}} + G_i - \ddot{\chi}_i^d) - \eta_i \text{sign}(s_i) \tag{4.26}$$

With the consideration of wind effects, an adaptive wind compensation is designed to derive the control law. Let $\hat{c}_i$ for $i \in \{x,\, y,\, z\}$ denote the estimate of drag coefficient. The corresponding control law can be designed as

$$\nu_i = -\frac{1}{h_i}(\beta_i\frac{q_i}{p_i}\dot{\tilde{\chi}}_i^{2-\frac{p_i}{q_i}} + G_i - \ddot{\chi}_{i,1}^d) - \eta_i \text{sign}(s_i) - \hat{c}_i f_i \tag{4.27}$$

The corresponding adaptive law to estimate the drag coefficient is given by

$$\dot{\hat{c}}_i = \gamma_i s_i \frac{1}{\beta_i}\frac{p_i}{q_i}\dot{\tilde{\chi}}_i^{\frac{p_i}{q_i}-1} h_i f_i \tag{4.28}$$

Remark 4.2 *In many works, the aerodynamic drag forces are assumed to be bounded so that to handle them via the lumped disturbance. To specify the wind effect acting on the dynamics of the quadrotor UAV, the wind vector is defined as the time-varying parameter of the dynamic model, which can be estimated by the two-stage particle filter. The corresponding control law is developed to attenuate wind effects.*

Selecting the following Lyapunov candidate function:

$$V_P = \frac{1}{2}\sum_{i=x}^{z} s_i^2 + \frac{1}{\gamma_i}\tilde{c}_i^2 \tag{4.29}$$

where $\tilde{c}_i = \hat{c}_i - c_i$ is the estimation error of drag coefficient. The time derivative of the Lyapunov candidate function is obtained as

$$\begin{aligned}\dot{V}_P =& \sum_{i=x}^{z} s_i \dot{s}_i + \frac{1}{\gamma_i}\tilde{c}_i\dot{\hat{c}}_i \\ =& \sum_{i=x}^{z} s_i\{\dot{\tilde{\chi}}_i + \frac{1}{\beta_i}\frac{p_i}{q_i}\dot{\tilde{\chi}}_i^{\frac{p_i}{q_i}-1}[G_i + h_i(\nu_i + c_i f_i + d_i) - \ddot{\chi}_i^d]\} + \frac{1}{\gamma_i}\tilde{c}_i\dot{\hat{c}}_i\end{aligned} \tag{4.30}$$

Substituting the outer control law (4.27) and the adaptive law (4.28) into Eq. (4.30), the following condition can be derived:

$$\begin{aligned}\dot{V}_P =&\sum_{i=x}^{z} s_i\{\dot{\tilde{\chi}}_i + \frac{1}{\beta_i}\frac{p_i}{q_i}\dot{\tilde{\chi}}_i^{\frac{p_i}{q_i}-1}[G_i + h_i(-\frac{1}{h_i}(\beta_i\frac{q_i}{p_i}\dot{\tilde{\chi}}_i^{2-\frac{p_i}{q_i}} + G_i - \ddot{\chi}_i^d) - \hat{c}_i f_i \\ &- \eta_i \text{sign}(s_i) + c_i f_i + d_i) - \ddot{\chi}_i^d]\} + \frac{1}{\gamma_i}\tilde{c}_i\dot{\hat{c}}_i \\ =&\sum_{i=x}^{z} s_i\frac{1}{\beta_i}\frac{p_i}{q_i}\dot{\tilde{\chi}}_i^{\frac{p_i}{q_i}-1}[-h_i\hat{c}_i f_i + h_i c_i f_i + h_i d_i - h_i\eta_i\text{sign}(s_i)] + \frac{1}{\gamma_i}\tilde{c}_i\dot{\hat{c}}_i \\ =&\sum_{i=x}^{z} \tilde{c}_i(\frac{1}{\gamma_i}\dot{\hat{c}}_i - s_i\frac{1}{\beta_i}\frac{p_i}{q_i}\dot{\tilde{\chi}}_i^{\frac{p_i}{q_i}-1}h_i f_i) + \frac{1}{\beta_i}\frac{p_i}{q_i}\dot{\tilde{\chi}}_i^{\frac{p_i}{q_i}-1}h_i(-\eta_i s_i \text{sign}(s_i) + d_i s_i) \\ \leq&\sum_{i=x}^{z} -\eta_i'|s_i|\end{aligned} \tag{4.31}$$

where $\eta_i' = \frac{1}{\beta_i}\frac{p_i}{q_i}\dot{\tilde{\chi}}_i^{\frac{p_i}{q_i}-1}h_i(\eta_i - D_i) \geq 0$.

Therefore, the system satisfies the standard η-reachability condition to guarantee the trajectory tracking performance of the designed outer controller in the presence of unknown winds and model uncertainty.

To compensate for wind effects in the controller design, it is important to estimate time-varying wind vectors for a quadrotor UAV. As elaborated in the previous chapter, the wind estimation can be produced by the proposed two-stage particle filter. Based on the estimated wind vectors, the wind drags can be compensated with the proposed control strategy to guarantee the performance and reliability of a quadrotor UAV in the presence of unknown winds.

Based on the estimated wind vectors $\hat{\xi}_i$ for $i \in \{x,\, y,\, z\}$, the terms associated with the drag forces can be obtained as

$$\begin{aligned}\hat{f}_x &= (\hat{\xi}_x - \dot{x})\sqrt{(\hat{\xi}_x - \dot{x})^2 + (\hat{\xi}_y - \dot{y})^2} \\ \hat{f}_y &= (\hat{\xi}_y - \dot{y})\sqrt{(\hat{\xi}_x - \dot{x})^2 + (\hat{\xi}_y - \dot{y})^2} \\ \hat{f}_z &= (\hat{\xi}_z - \dot{z})\end{aligned} \tag{4.32}$$

Considering the errors of wind estimation produced by the two-stage particle filter, the error associated with the drag forces is denoted as $\tilde{f}_i^{-1} = f_i^{-1} - \hat{f}_i^{-1}$. Then, the dynamic model Eq. (4.10) can be reconstructed as

$$
\begin{aligned}
\dot{\chi}_{i,2} =& G_i + h_i(\nu_i + c_i f_i + d_i) \\
=& G_i + h_i[\nu_i + c_i(\hat{f}_i^{-1} + \tilde{f}_i^{-1})^{-1} + d_i] \\
=& G_i + h_i[\nu_i + (1 - f_i \tilde{f}_i^{-1}) c_i \hat{f}_i + d_i] \\
=& G_i + h_i(\nu_i + \bar{c}_i \hat{f}_i + d_i)
\end{aligned}
\tag{4.33}
$$

where $\bar{c}_i$ for $i \in \{x,\, y,\, z\}$ is defined as the drag coefficient of the reconstructed model. By employing the adaptive law to estimate the drag coefficient, the performance of the designed controller can be maintained.

Therefore, the ultimate control law can be presented as

$$
\nu_i = -\frac{1}{h_i}(\beta_i \frac{q_i}{p_i} \dot{\tilde{\chi}}_i^{2-\frac{p_i}{q_i}} + G_i - \ddot{\chi}_i^d) - \eta_i \mathrm{sign}(s_i) - \hat{\bar{c}}_i \hat{f}_i
\tag{4.34}
$$

with

$$
\dot{\hat{\bar{c}}}_i = \gamma_i s_i \frac{1}{\beta_i} \frac{p_i}{q_i} \dot{\tilde{\chi}}_i^{\frac{p_i}{q_i}-1} h_i \hat{f}_i
\tag{4.35}
$$

By using the virtual control laws ν_i for $i \in \{x,\, y,\, z\}$, one can carry out the computations of the thrust F_z, the desired roll ϕ^d and pitch θ^d angles.

From Eq. (4.9), the computation of the thrust can be expressed as

$$
F_z = \sqrt{\nu_x^2 + \nu_y^2 + \nu_z^2}
\tag{4.36}
$$

Given the desired yaw ψ^d angle, the computations of the desired roll ϕ^d and pitch θ^d

angles can be expressed as

$$
\begin{aligned}
\phi^d &= \arcsin\left(-\frac{\nu_x \sin\psi^d - \nu_y \cos\psi^d}{\sqrt{\nu_x^2 + \nu_y^2 + \nu_z^2}}\right) \\
\theta^d &= \arctan\left(\frac{\nu_x \cos\psi^d + \nu_y \sin\psi^d}{\nu_z}\right)
\end{aligned}
\tag{4.37}
$$

4.3.2 Inner-loop Control

The inner-loop control strategy is designed to track the desired roll ϕ^d, pitch θ^d and yaw ψ^d angles. Consider the rotational dynamics of a quadrotor UAV

$$
\begin{aligned}
\ddot{\phi} &= \frac{I_y - I_z}{I_x}\dot{\theta}\dot{\psi} + \frac{\tau_\phi}{I_x} + \frac{d_\phi}{I_x} \\
\ddot{\theta} &= \frac{I_z - I_x}{I_y}\dot{\phi}\dot{\psi} + \frac{\tau_\theta}{I_y} + \frac{d_\theta}{I_y} \\
\ddot{\psi} &= \frac{I_x - I_y}{I_z}\dot{\phi}\dot{\theta} + \frac{\tau_\psi}{I_z} + \frac{d_\psi}{I_z}
\end{aligned}
\tag{4.38}
$$

where d_j for $j \in \{\phi, \theta, \psi\}$ represents the unknown disturbance associated with the rotational motion, which is assumed to be unknown but bounded, i.e., $|d_j| \leq D_j$.

By recalling Eq. (4.38), the control-oriented model can be obtained as

$$
\begin{aligned}
\dot{\chi}_{j,1} &= \chi_{j,2} \\
\dot{\chi}_{j,2} &= f_j + h_j(\tau_j + d_j)
\end{aligned}
\tag{4.39}
$$

where

$$
\begin{aligned}
\chi_{\phi,1} &= \phi \\
\chi_{\theta,1} &= \theta \\
\chi_{\psi,1} &= \psi
\end{aligned}
\tag{4.40}
$$

$$\begin{aligned} \chi_{\phi,2} &= \dot{\phi} \\ \chi_{\theta,2} &= \dot{\theta} \\ \chi_{\psi,2} &= \dot{\psi} \end{aligned} \tag{4.41}$$

$$\begin{aligned} f_{\phi} &= \frac{I_y - I_z}{I_x}\dot{\theta}\dot{\psi} \\ f_{\theta} &= \frac{I_z - I_x}{I_y}\dot{\phi}\dot{\psi} \\ f_{\psi} &= \frac{I_x - I_y}{I_z}\dot{\phi}\dot{\theta} \end{aligned} \tag{4.42}$$

$$\begin{aligned} h_{\phi} &= \frac{1}{I_x} \\ h_{\theta} &= \frac{1}{I_y} \\ h_{\psi} &= \frac{1}{I_z} \end{aligned} \tag{4.43}$$

Then, the tracking error related to attitude is defined as

$$\tilde{\chi}_j = \chi_{j,1} - \chi_{j,1}^d \tag{4.44}$$

and its corresponding derivative is given by

$$\dot{\tilde{\chi}}_j = \dot{\chi}_{j,1} - \dot{\chi}_{j,1}^d = \chi_{j,2} - \dot{\chi}_j^d \tag{4.45}$$

By combining Eqs. (4.39) and (4.45), the error dynamics can be obtained as

$$\begin{aligned} \ddot{\tilde{\chi}}_j =& \dot{\chi}_{j,2} - \ddot{\chi}_j^d \\ =& f_j + h_j(\tau_j + d_j) - \ddot{\chi}_j^d \end{aligned} \tag{4.46}$$

Again, select the nonsingular terminal sliding-mode surface [91]:

$$s_j = \tilde{\chi}_j + \frac{1}{\beta_j}\dot{\tilde{\chi}}_j^{\frac{p_j}{q_j}} \tag{4.47}$$

where β_j, p_j and q_j are positive design parameters. p_j and q_j are odd numbers, which satisfy $1 < \frac{p_j}{q_j} < 2$.

By differentiating Eq. (4.47) with respect to time, the expression can be obtained as

$$\begin{aligned} \dot{s}_j =& \dot{\tilde{\chi}}_j + \frac{1}{\beta_j}\frac{p_j}{q_j}\dot{\tilde{\chi}}_j^{\frac{p_j}{q_j}-1}\ddot{\tilde{\chi}}_j \\ =& \dot{\tilde{\chi}}_j + \frac{1}{\beta_j}\frac{p_j}{q_j}\dot{\tilde{\chi}}_j^{\frac{p_j}{q_j}-1}[f_j + h_j(\tau_j + d_j) - \ddot{\chi}_j^d] \end{aligned} \tag{4.48}$$

Similar to the design of the position control law, the attitude control laws are developed as

$$\begin{aligned} \tau_j =& \tau_j^{\text{eq}} + \tau_j^{\text{dis}} \\ =& -\frac{1}{h_j}(\beta_j \frac{q_j}{p_j}\dot{\tilde{\chi}}_j^{2-\frac{p_j}{q_j}} + f_j - \ddot{\chi}_j^d) - \eta_j \text{sign}(s_j) \end{aligned} \tag{4.49}$$

where $\eta_j > D_j$ for $j \in \{\phi, \theta, \psi\}$ are positive design parameters.

Selecting the following Lyapunov candidate function:

$$V_\Theta = \frac{1}{2}\sum_{j=\phi}^{\psi} s_j^2 \tag{4.50}$$

The derivative of the Lyapunov candidate function is obtained as

$$\begin{aligned} \dot{V}_\Theta =& \sum_{j=\phi}^{\psi} s_j \dot{s}_j \\ =& \sum_{j=\phi}^{\psi} s_j \{\dot{\tilde{\chi}}_j + \frac{1}{\beta_j}\frac{p_j}{q_j}\dot{\tilde{\chi}}_j^{\frac{p_j}{q_j}-1}[f_j + h_j(\tau_j + d_j) - \ddot{\chi}_j^d]\} \end{aligned} \tag{4.51}$$

Substituting the attitude control law Eq. (4.49) into Eq. (4.51), the following condition can be derived as:

$$
\begin{aligned}
\dot{V}_{\Theta} =& \sum_{j=\phi}^{\psi} s_j\{\dot{\tilde{\chi}}_j + \frac{1}{\beta_j}\frac{p_j}{q_j}\dot{\tilde{\chi}}_j^{\frac{p_j}{q_j}-1}[f_j + h_j(-\frac{1}{h_j}(\beta_j\frac{q_j}{p_j}\dot{\tilde{\chi}}_j^{2-\frac{p_j}{q_j}} + f_j - \ddot{\chi}_j^d) \\
& - \eta_j \mathrm{sign}(s_j) + d_j) - \ddot{\chi}_j^d]\} \\
=& \sum_{j=\phi}^{\psi} \frac{1}{\beta_j}\frac{p_j}{q_j}\dot{\tilde{\chi}}_j^{\frac{p_j}{q_j}-1}[h_j d_j s_j - h_j \eta_j \mathrm{sign}(s_j) s_j] \\
\leq& \sum_{j=\phi}^{\psi} -\eta_j' |s_j|
\end{aligned}
\tag{4.52}
$$

where $\eta_j' = \frac{1}{\beta_j}\frac{p_j}{q_j}\dot{\tilde{\chi}}_j^{\frac{p_j}{q_j}-1} h_j(\eta_j - D_j) > 0$.

Therefore, the system satisfies the standard η-reachability condition to guarantee the performance of the inner controller to track the desired attitudes.

In order to produce the control thrust F_z and torques $[\tau_\phi,\ \tau_\theta,\ \tau_\psi]^T$, based on Eq. (2.9), the computations of the thrusts are given by

$$
\begin{bmatrix} T_1 \\ T_2 \\ T_3 \\ T_4 \end{bmatrix} = \begin{bmatrix} \frac{1}{4} & 0 & \frac{1}{2l} & -\frac{1}{4k_m} \\ \frac{1}{4} & -\frac{1}{2l} & 0 & \frac{1}{4k_m} \\ \frac{1}{4} & 0 & -\frac{1}{2l} & -\frac{1}{4k_m} \\ \frac{1}{4} & \frac{1}{2l} & 0 & \frac{1}{4k_m} \end{bmatrix} \begin{bmatrix} F_z \\ \tau_\phi \\ \tau_\theta \\ \tau_\psi \end{bmatrix}
\tag{4.53}
$$

4.4 Active Wind Rejection Cooperative Control of Multiple Quadrotor UAVs

The active wind rejection cooperative control strategy is proposed to maintain the formation performance of multiple quadrotor UAVs in the presence of unknown winds. Considering the different wind effects acting on each UAV, the active wind rejection cooperative control scheme is adopted to attenuate the unexpected wind disturbances for each UAV and maintain the cooperative tracking performances of multiple quadrotor UAVs in the formation flight. More specifically, the UAV fleet should keep the formation shape and each UAV should track the desired trajectory against ambient winds.

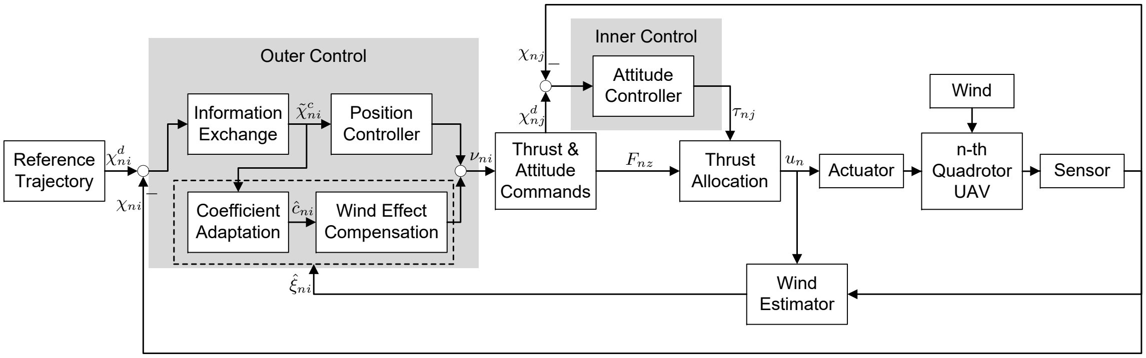

Figure 4.2: Framework of the proposed wind rejection cooperative control strategy of multiple quadrotor UAVs

Fig. 4.2 shows the framework of the proposed wind rejection cooperative control strategy. A distributed control structure is adopted for a group of UAVs so that vehicles should exchange information with each other to obtain the formation tracking errors. Then, the proposed control strategy generates control signals based on the wind estimation for each UAV. Similarly, the distributed control scheme for each vehicle is comprised of the outer control and the inner control.

4.4.1 Basic Graph Theory

The formation control strategy is developed for a group of N quadrotor UAVs. To describe the information flow in the group of quadrotor UAVs, an undirected graph is generated, which is denoted as $\mathcal{G} = \{\mathcal{V}, \mathcal{E}, \mathcal{A}\}$. $\mathcal{V} = \{v_1, v_2, \cdots, v_N\}$ represents the set of UAVs. $\mathcal{E} \subseteq \{(v_n, v_m)|v_n, v_m \in \mathcal{V}\}$ represents the set of communication links with unordered pairs of UAVs (v_n, v_m). $\mathcal{A} \in \mathbb{R}^{N\times N}$ denotes the adjacency matrix and α_{nm} is the nonnegative entry of $\mathcal{A}$. $\alpha_{nm} = 1$ if there is information exchange between the m-th and n-th quadrotor UAVs, otherwise it is zero. If the graph has the property that $(v_n,\, v_m) \in \mathcal{E} \iff (v_m,\, v_n) \in \mathcal{E}$, for any $v_n,\, v_m \in \mathcal{V}$, it is said to be undirected,. The graph is named as a connected graph, if there exists a path between any two UAVs. The set of neighbors of the m-th UAV is denoted as $S_n = \{v_m | (v_n,\, v_m) \in \mathcal{E}\}$. Let $\mathcal{B} = \mathrm{diag}(b_1,\, b_2,\, \cdots,\, b_N)$ denote the degree matrix of a graph with $b_n = \sum_{m=1}^{N} \alpha_{nm}$ for $n \in \{1,\, \cdots,\, N\}$. The Laplacian matrix $\mathcal{L}$ is defined as $\mathcal{L} = \mathcal{B} - \mathcal{A}$.

Assumption 4.1 *The graph containing all quadrotor UAVs is undirected and connected.*

Lemma 4.1 *If a graph is undirected and connected, and Λ is a diagonal matrix with non-negative entries, then the matrix $\mathcal{H} = \mathcal{L} + \Lambda$ is positive definite [94, 95, 96].*

4.4.2 Cooperative Controller Design

To maintain the formation shape, the trajectory tracking error of each quadrotor UAV should satisfy the following condition

$$\tilde{\chi}_{ni} = \tilde{\chi}_{mi} \tag{4.54}$$

where $\tilde{\chi}_{ni}$ and $\tilde{\chi}_{mi}$ are the trajectory tracking errors of the n-th and m-th UAVs.

Considering the information exchange among the group of quadrotor UAVs, the cooperative tracking error of the n-th quadrotor UAV is defined as

$$\begin{aligned} \tilde{\chi}_{ni}^{c} =& \lambda_{i,1}\tilde{\chi}_{ni} + \lambda_{i,2} \sum_{m \in S_n} \alpha_{nm}(\tilde{\chi}_{ni} - \tilde{\chi}_{mi}) \\ =& (\lambda_{i,1} + \lambda_{i,2} \sum_{m \in S_n} \alpha_{nm})\tilde{\chi}_{ni} - \lambda_{i,2} \sum_{m \in S_n} \alpha_{nm}\tilde{\chi}_{mi} \end{aligned} \tag{4.55}$$

where $n \in \{1,\, \cdots,\, N\}$ and $i \in \{x,\, y,\, z\}$. $\lambda_{i,1}$ and $\lambda_{i,2}$ are positive parameters that regulate the individual trajectory tracking error and the formation error, respectively.

Then, based on the basic graph theory, the cooperative tracking error of all quadrotor

UAVs can be written as

$$\tilde{\boldsymbol{\chi}}_i^c = (\lambda_{i,1}\mathrm{I}_N + \lambda_{i,2}\mathcal{L})\tilde{\boldsymbol{\chi}}_i \tag{4.56}$$

where $\tilde{\boldsymbol{\chi}}_i^c = [\tilde{\chi}_{1i}^c,\ \tilde{\chi}_{2i}^c,\ \cdots,\ \tilde{\chi}_{Ni}^c]^T$ and $\tilde{\boldsymbol{\chi}}_i = [\tilde{\chi}_{1i},\ \tilde{\chi}_{2i},\ \cdots,\ \tilde{\chi}_{Ni}]^T$ for $i \in \{x,\ y,\ z\}$. By referring to Assumption 4.1 and Lemma 4.1, the matrix $(\lambda_{i,1}\mathrm{I}_N + \lambda_{i,2}\mathcal{L})$ is symmetric positive definite. According to the property of a positive definite matrix, the $\tilde{\boldsymbol{\chi}}_i$ converges to zero once the $\tilde{\boldsymbol{\chi}}_i^c$ converges to zero, therefore $\tilde{\chi}_{ni}^c$ and $\tilde{\chi}_{ni}$ converge to zero for $n \in \{1,\ \cdots,\ N\}$. To carry on, the cooperative control strategy will be designed for an individual quadrotor UAV, i.e., based on $\tilde{\chi}_{ni}$ for $i \in \{x,\ y,\ z\}$.

The derivative of cooperative tracking error of the n-th quadrotor UAV is given by

$$\begin{aligned}\dot{\tilde{\chi}}_{ni}^c =& (\lambda_{i,1} + \lambda_{i,2}\sum_{m\in S_n}\alpha_{nm})\dot{\tilde{\chi}}_{ni} - \lambda_{i,2}\sum_{m\in S_n}\alpha_{nm}\dot{\tilde{\chi}}_{mi} \\ =& \Psi_{ni}\dot{\tilde{\chi}}_{ni} - \lambda_{i,2}\sum_{m\in S_n}\alpha_{nm}\dot{\tilde{\chi}}_{mi}\end{aligned} \tag{4.57}$$

where $\Psi_{ni} = \lambda_{i,1} + \lambda_{i,2}\sum_{m\in S_n}\alpha_{nm} > 0$.

The cooperative error dynamics can be obtained as

$$\ddot{\tilde{\chi}}_{ni}^c = \Psi_{ni}\ddot{\tilde{\chi}}_{ni} - \lambda_{i,2}\sum_{m\in S_n}\alpha_{nm}\ddot{\tilde{\chi}}_{mi} \tag{4.58}$$

By substituting Eq. (4.10) into Eq. (4.58), the following expression can be obtained as

$$\ddot{\tilde{\chi}}_{ni}^c = \Psi_{ni}[G_{ni} + h_{ni}(\nu_{ni} + c_{ni}f_{ni} + d_{ni}) - \ddot{\chi}_{ni}^d] - \lambda_{i,2}\sum_{m\in S_n}\alpha_{nm}\ddot{\tilde{\chi}}_{mi} \tag{4.59}$$

where d_{ni} represents the unknown disturbance, which is bounded as $|d_{ni}| \leq D_{ni}$.

Similarly, select the nonsingular terminal sliding-mode surface:

$$s_{ni} = \tilde{\chi}_{ni}^c + \frac{1}{\beta_{ni}}\dot{\tilde{\chi}}_{ni}^{c\,\frac{p_{ni}}{q_{ni}}} \tag{4.60}$$

where β_{ni}, p_{ni} and q_{ni} are positive design parameters. p_{ni} and q_{ni} are positive odd numbers, which satisfy $1 < \frac{p_{ni}}{q_{ni}} < 2$.

By differentiating Eq. (4.60) with respect to time, the expression can be obtained as

$$\begin{aligned}\dot{s}_{ni} =& \dot{\tilde{\chi}}^c_{ni} + \frac{1}{\beta_{ni}}\frac{p_{ni}}{q_{ni}}\dot{\tilde{\chi}}^c_{ni}{}^{\frac{p_{ni}}{q_{ni}}-1}\ddot{\tilde{\chi}}^c_{ni} \\ =& \dot{\tilde{\chi}}^c_{ni} + \frac{1}{\beta_{ni}}\frac{p_{ni}}{q_{ni}}\dot{\tilde{\chi}}^c_{ni}{}^{\frac{p_{ni}}{q_{ni}}-1}\{\Psi_{ni}[G_{ni} + h_{ni}(\nu_{ni} + c_{ni}f_{ni} + d_{ni}) - \ddot{\chi}^d_{ni}] \\ & - \lambda_{i,2}\sum_{m\in S_n}\alpha_{nm}\ddot{\tilde{\chi}}_{mi}\}\end{aligned} \tag{4.61}$$

With the consideration of active wind rejection, the distributed cooperative tracking law is designed as

$$\begin{aligned}\nu_{ni} =& -\frac{1}{h_{ni}\Psi_{ni}}\beta_{ni}\frac{q_{ni}}{p_{ni}}\dot{\tilde{\chi}}^c_{ni}{}^{2-\frac{p_{ni}}{q_{ni}}} + \frac{1}{h_{ni}\Psi_{ni}}\lambda_{i,2}\sum_{m\in S_n}\alpha_{nm}\ddot{\tilde{\chi}}_{mi} \\ & - \frac{G_{ni}}{h_{ni}} + \frac{\ddot{\chi}^d_{ni}}{h_{ni}} - \eta_{ni}\text{sign}(s_{ni}) - \hat{\bar{c}}_{ni}\hat{f}_{ni}\end{aligned} \tag{4.62}$$

with

$$\dot{\hat{\bar{c}}}_{ni} = \gamma_{ni}s_{ni}\frac{1}{\beta_{ni}}\frac{p_{ni}}{q_{ni}}\dot{\tilde{\chi}}^c_{ni}{}^{\frac{p_{ni}}{q_{ni}}-1}\Psi_{ni}h_{ni}\hat{f}_{ni} \tag{4.63}$$

where $\eta_{ni} > D_{ni}$ and γ_{ni} are positive parameters.

Selecting the following Lyapunov candidate function:

$$V_{np} = \frac{1}{2}\sum_{i=x}^{z} s^2_{ni} + \frac{1}{\gamma_{ni}}\tilde{\bar{c}}^2_{ni} \tag{4.64}$$

where $\tilde{\bar{c}}_{ni} = \hat{\bar{c}}_{ni} - \bar{c}_{ni}$ represents the estimation error of the reconstructed drag coefficient.

The derivative of the Lyapunov candidate function with respect to time is obtained as

$$\dot{V}_{np} = \sum_{i=x}^{z} s_{ni}\dot{s}_{ni} + \frac{1}{\gamma_{ni}}\tilde{\bar{c}}_{ni}\dot{\hat{\bar{c}}}_{ni} \tag{4.65}$$

Substituting Eqs. (4.61)-(4.63) into Eq. (4.65), the following expression yields

$$
\begin{aligned}
\dot{V}_{np} =& \sum_{i=x}^{z} s_{ni}\frac{1}{\beta_{ni}}\frac{p_{ni}}{q_{ni}}{\dot{\tilde{\chi}}^{c}_{ni}}{}^{\frac{p_{ni}}{q_{ni}}-1}\Psi_{ni}h_{ni}[c_{ni}f_{ni} - \hat{\bar{c}}_{ni}\hat{f}_{ni} + d_{ni} \\
& - \eta_{ni}\text{sign}(s_{ni})] + \frac{1}{\gamma_{ni}}\tilde{\bar{c}}_{ni}\dot{\hat{\bar{c}}}_{ni} \\
\dot{V}_{np} =& \sum_{i=x}^{z} s_{ni}\frac{1}{\beta_{ni}}\frac{p_{ni}}{q_{ni}}{\dot{\tilde{\chi}}^{c}_{ni}}{}^{\frac{p_{ni}}{q_{ni}}-1}\Psi_{ni}h_{ni}[\bar{c}_{ni}\hat{f}_{ni} - \hat{\bar{c}}_{ni}\hat{f}_{ni} + d_{ni} \\
& - \eta_{ni}\text{sign}(s_{ni})] + \frac{1}{\gamma_{ni}}\tilde{\bar{c}}_{ni}\dot{\hat{\bar{c}}}_{ni} \qquad (4.66) \\
=& \sum_{i=x}^{z} \tilde{\bar{c}}_{ni}(\frac{1}{\gamma_{ni}}\dot{\hat{\bar{c}}}_{ni} - s_{ni}\frac{1}{\beta_{ni}}\frac{p_{ni}}{q_{ni}}\Psi_{ni}{\dot{\tilde{\chi}}^{c}_{ni}}{}^{\frac{p_{ni}}{q_{ni}}-1}h_{ni}\hat{f}_{ni}) \\
& + \frac{1}{\beta_{ni}}\frac{p_{ni}}{q_{ni}}{\dot{\tilde{\chi}}^{c}_{ni}}{}^{\frac{p_{ni}}{q_{ni}}-1}\Psi_{ni}h_{ni}(d_{ni}s_{ni} - \eta_{ni}\text{sign}(s_{ni})s_{ni}) \\
\leq& \sum_{i=x}^{z} -\eta'_{ni}|s_{ni}|
\end{aligned}
$$

where $\eta'_{ni} = \frac{1}{\beta_{ni}}\frac{p_{ni}}{q_{ni}}{\dot{\tilde{\chi}}^{c}_{ni}}{}^{\frac{p_{ni}}{q_{ni}}-1}\Psi_{ni}h_{ni}(\eta_{ni} - D_{ni})$.

Therefore, the system satisfies the standard η-reachability condition to guarantee the cooperative trajectory tracking performance of the formation position controller in the presence of wind effect and model uncertainty.

It is noted that the formation position control strategy is developed to maintain the entire formation shape of multiple UAVs in the flight. To stabilize the attitude, the attitude control law Eq. (4.49) is applied for each UAV.

4.5 Simulation Results

In this section, simulations are conducted to demonstrate the effectiveness of the proposed control strategies for the control of a single quadrotor UAV and the formation control of multiple quadrotor UAVs in the presence of wind. The quadrotor dynamic model Eq.

(2.11) is used in the simulations. The model parameters are given in Table 2.1. The two-stage particle filter is also adopted to produce estimates of states and wind vectors for the quadrotor UAV in order to implement the active wind rejection control strategy. The process and measurement noises of the system are considered, variances of which are given in Tables 2.2 and 2.3.

4.5.1 Control of a Single Quadrotor UAV in the Presence of Wind

The initial states of the quadrotor UAV are set as $x(0) = 0\,\mathrm{m}$, $y(0) = 0\,\mathrm{m}$, $z(0) = 0\,\mathrm{m}$, $\phi(0) = 0\,\mathrm{rad}$, $\theta(0) = 0\,\mathrm{rad}$, and $\psi(0) = 0\,\mathrm{rad}$. The parameters of the proposed control algorithm are given in Table 4.1. Considering the wind estimation errors, the parameters of the adaptive law Eq. (4.28) are set as $\gamma_x = 1$, $\gamma_y = 1$ and $\gamma_z = 10$. To deal with the chattering problem, the sign functions are replaced by saturation functions, but the robust performance is compromised. The saturation function is defined as

$$\mathrm{sat}(s) = \begin{cases} 1 & s > \Phi \\ s/\Phi & |s| \leq \Phi \\ -1 & s < -\Phi \end{cases} \tag{4.67}$$

where Φ represents the boundary layer thickness, which are set as $\Phi_x = 0.2$, $\Phi_y = 0.2$, $\Phi_z = 0.2$, $\Phi_\phi = 0.1$, $\Phi_\theta = 0.1$, and $\Phi_\psi = 0.1$.

Table 4.1: Parameters of the active wind rejection controller

Parameter	β_x, β_y, β_z	p_x, p_y, p_z	q_x, q_y, q_z	η_x, η_y, η_z
Value	2	13	11	10
Parameter	β_ϕ, β_θ, β_ψ	p_ϕ, p_θ, p_ψ	q_ϕ, q_θ, q_ψ	η_ϕ, η_θ, η_ψ
Value	10	13	11	2

To demonstrate the performance of the proposed control scheme against wind effects, the designed control scheme is compared with a pure nonsingular terminal sliding mode control (NTSMC). The pure NTSMC-based controller is designed without considering the explicit wind effects acting on the quadrotor dynamics. The performances of the proposed active wind rejection control scheme are evaluated in the following cases:

(1) Hovering performance under continuous wind

(2) Hovering performance under wind gust

(3) Trajectory tracking performance under continuous wind

Hovering Performance under Continuous Wind

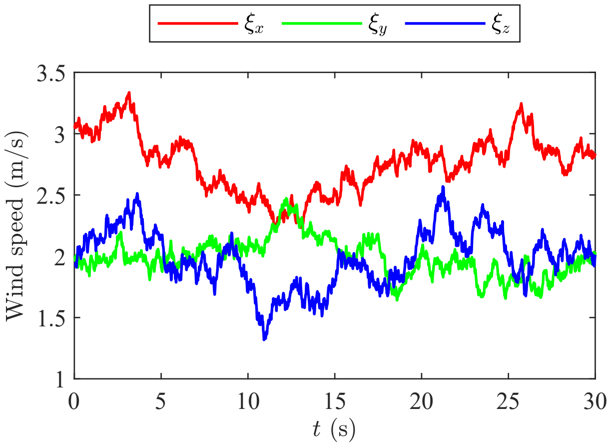

Figure 4.3: Generated continuous wind

The rendered continuous wind is composed of a $[3,\ 2,\ 2]^T$ $\mathrm{m/s}$ constant wind and a Dryden turbulence, as shown in Fig. 4.3. The quadrotor UAV is controlled to hover at the initial position $[0,\ 0,\ 0]^T$ in the presence of this wind condition.

Figs. 4.4 and 4.5 demonstrate the hovering performances of a quadrotor UAV and control thrusts of four rotors under the continuous wind. In the case of continuous wind condition, both controllers can stabilize the quadrotor UAV under the continuous winds, whereas the proposed control scheme achieves a better hovering performance. Fig. 4.6 shows the

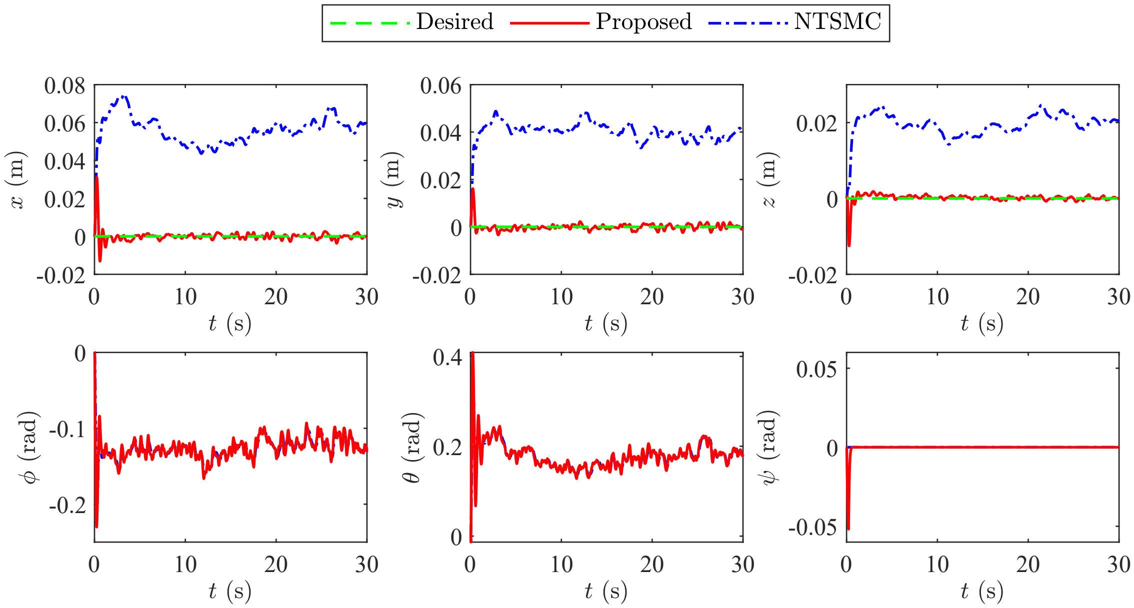

Figure 4.4: Hovering performances of a quadrotor UAV under the continuous wind

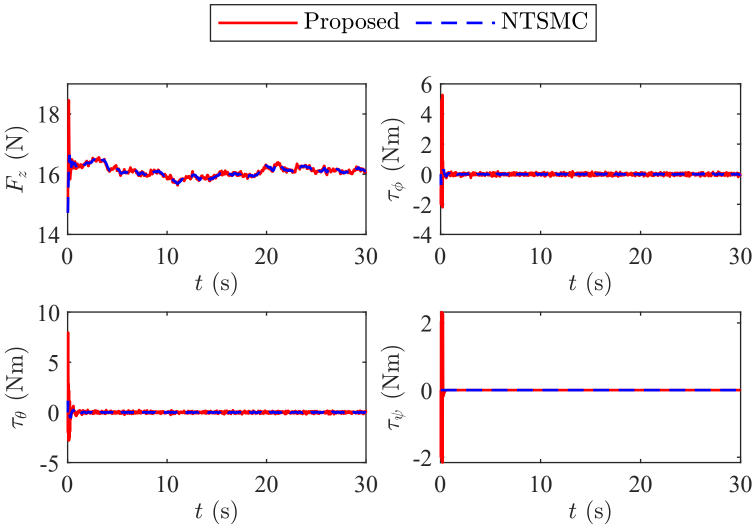

Figure 4.5: Thrusts of a quadrotor UAV for hovering under the continuous wind

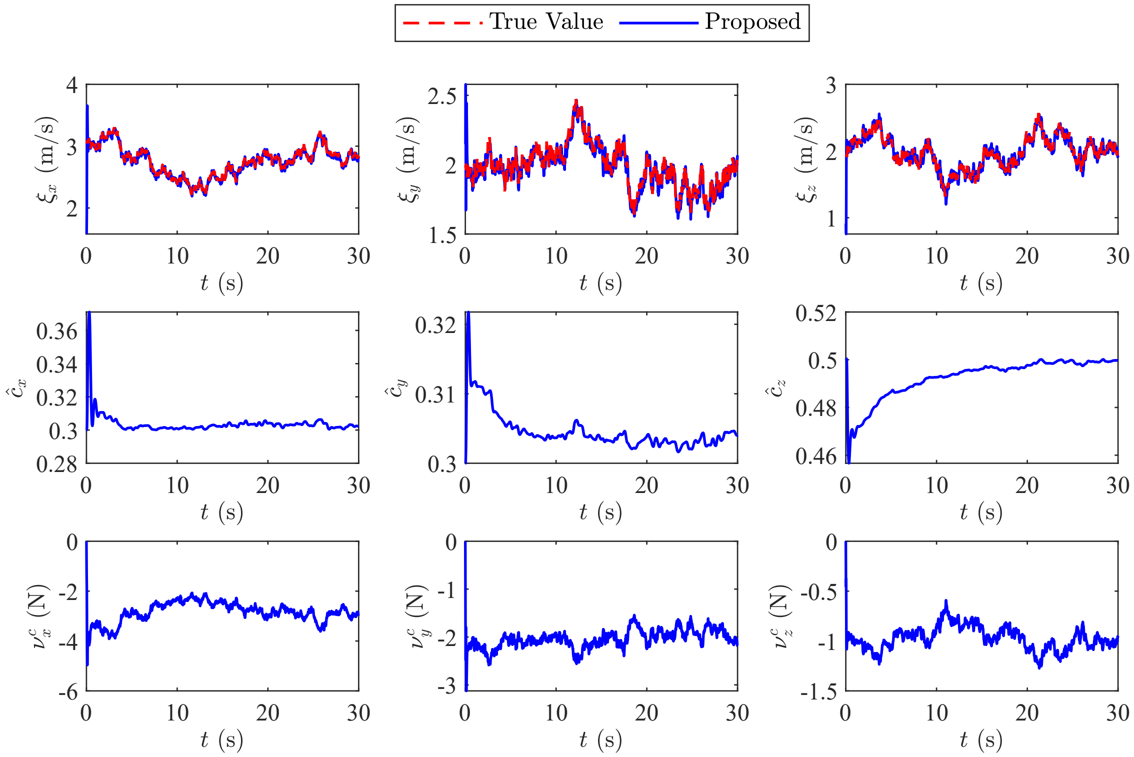

Figure 4.6: Wind and drag coefficient estimation of a quadrotor UAV for hovering under the continuous wind

estimation of continuous winds and drag coefficients. With the two-stage particle filter, the accurate wind estimation of the continuous wind are provided. Moreover, the adopted drag coefficient adaptation method can adjust the drag coefficients to stabilize the original system in the presence of model uncertainty and estimation error. Based on the estimated wind vectors and the adaptive drag coefficients, the proposed wind rejection control scheme can actively compensate for the wind effects acting on the quadrotor UAV and maintain the original system tracking performance and stability, in contrast to the pure NTSMC.

Hovering Performance under Wind Gust

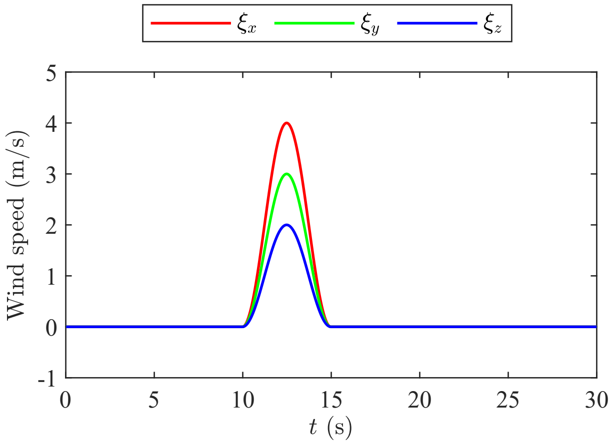

Figure 4.7: Generated wind gust

Fig. 4.7 shows the gust wind that is rendered based on the discrete 1-cosine wind gust model Eq. (2.21). The gust wind starts at $t = 10\,\mathrm{s}$ and lasts for $5\,\mathrm{s}$, the peak value of which is set as $[4,\ 3,\ 2]^T\ \mathrm{m/s}$.The quadrotor UAV is controlled to hover at the position $[0,\ 0,\ 0]^T$ under the wind gust.

Figs. 4.8 and 4.9 demonstrate the hovering performances of a quadrotor UAV and thrusts of four rotors under the gust wind. Before the wind gust, the proposed control scheme has a comparable hovering performance to the pure NTSMC. When the wind gust occurs, the sudden changes of the wind conditions in three direction can be instantaneously

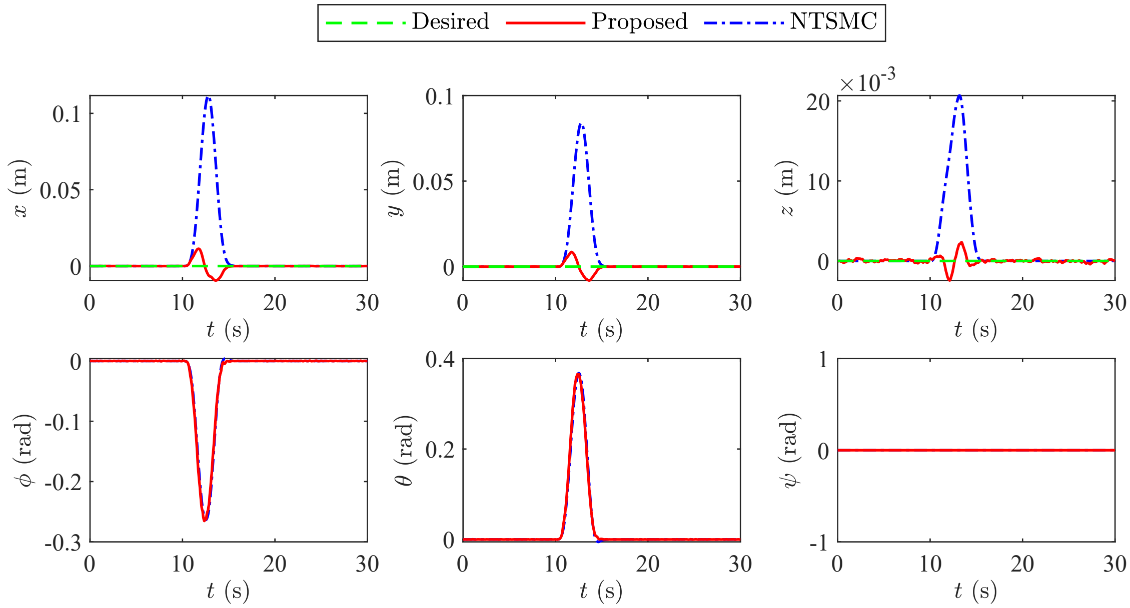

Figure 4.8: Hovering performances of a quadrotor UAV under the gust wind

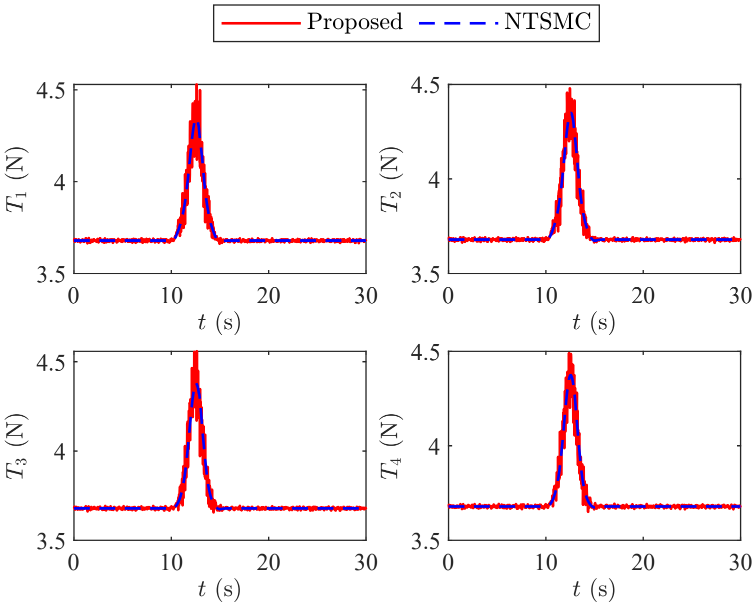

Figure 4.9: Thrusts of a quadrotor UAV for hovering under the gust wind

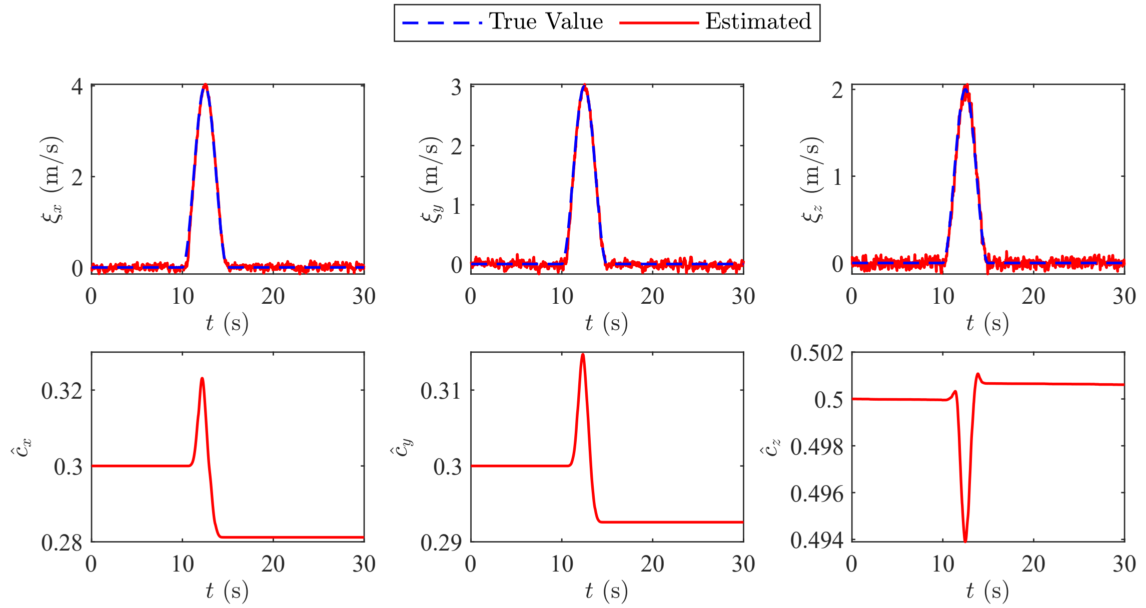

Figure 4.10: Wind and drag coefficient estimation of a quadrotor UAV for hovering under the gust wind

and accurately estimated by the wind estimation scheme. Due to the quick evolution of the wind gust in a short time window, it has a larger adverse effect on the quadrotor dynamics. Fig. 4.10 shows the estimation of wind gust and drag coefficients under the gust wind. The proposed wind rejection control scheme can promptly capture and attenuate the fast-varying wind effects caused by the wind gust so as to maintain the original system hovering performance and stability. Because of the advantages of the proposed wind rejection control scheme, the proposed scheme has smaller position errors than the pure NTSMC when hovering in the presence of wind gusts. Fig. 4.11 shows the performances of the proposed adaptive drag coefficient control under the gust wind. Compared with the same wind rejection control without adaptive drag coefficients, the proposed control scheme can increase the robustness of the quadrotor UAV, although it can not ensure the drag coefficients converge to the true values.

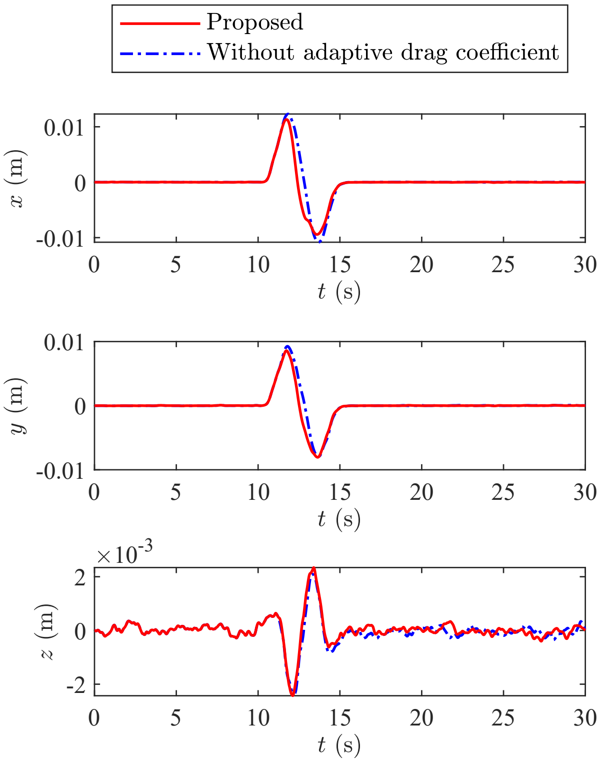

Figure 4.11: Performance of the proposed adaptive drag coefficient control under the gust wind

Trajectory Tracking Performance under Continuous Wind

In this case, the quadrotor UAV is controlled to track a predesigned trajectory given by

$$\begin{aligned} x^d &= 5\cos(\frac{\pi}{15}t) - 5 \\ y^d &= 5\sin(\frac{\pi}{15}t) \\ z^d &= -\sin(\frac{2\pi}{15}t) \end{aligned} \tag{4.68}$$

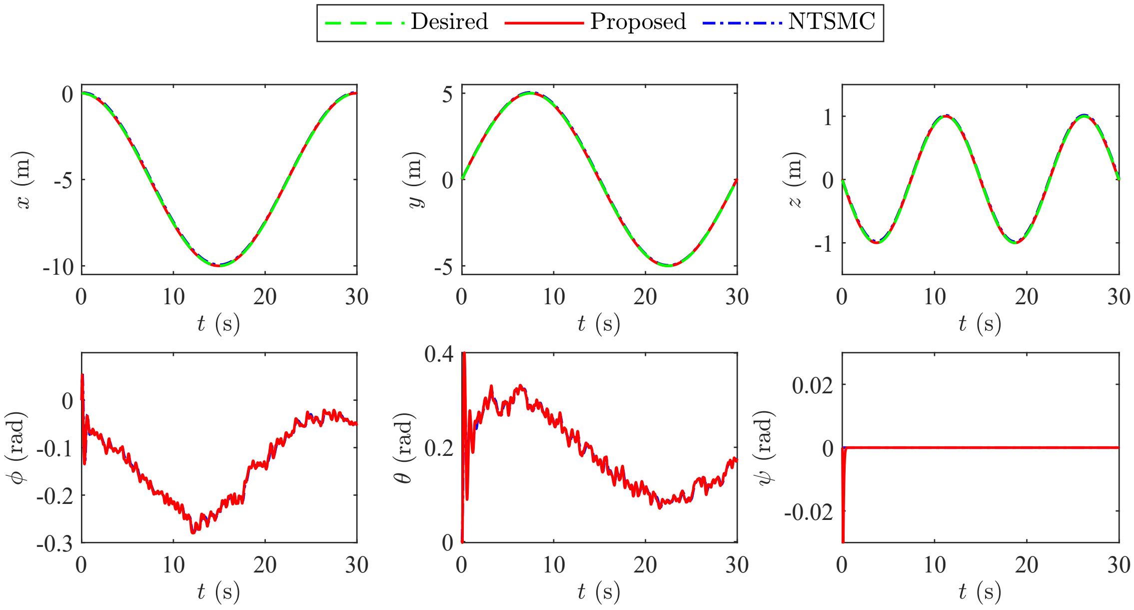

Figure 4.12: Trajectory tracking performances of a quadrotor UAV under the continuous wind

Figs. 4.12, 4.13 and 4.14 demonstrate the trajectory tracking performances of a quadrotor UAV under the continuous wind. During trajectory tracking, the proposed wind rejection control scheme can still accurately estimate the continuous wind and actively compensate for the unexpected wind effects acting on the quadrotor dynamics. The trajectory tracking errors are shown in Fig. 4.15. The proposed wind rejection control scheme shows a better trajectory tracking performance compared with the pure NTSMC in the

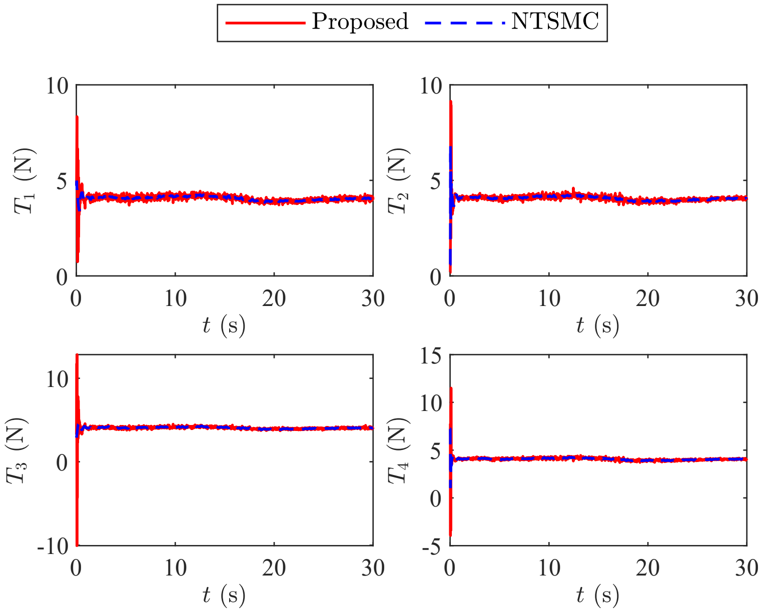

Figure 4.13: Thrusts of a quadrotor UAV for trajectory tracking under the continuous wind

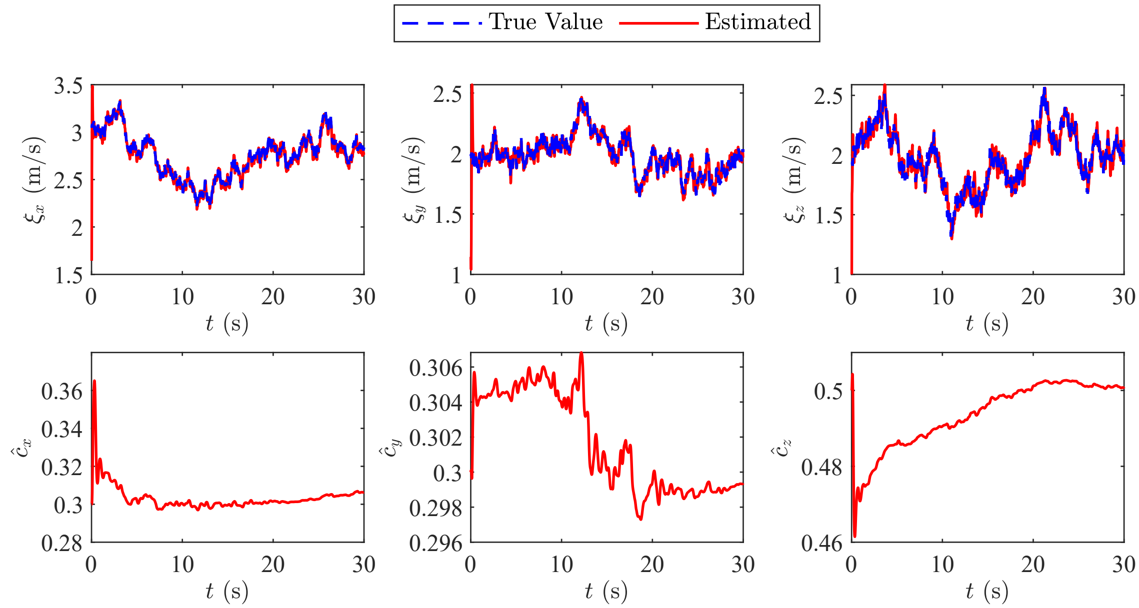

Figure 4.14: Wind and drag coefficient estimation of a quadrotor UAV for trajectory tracking under the continuous wind

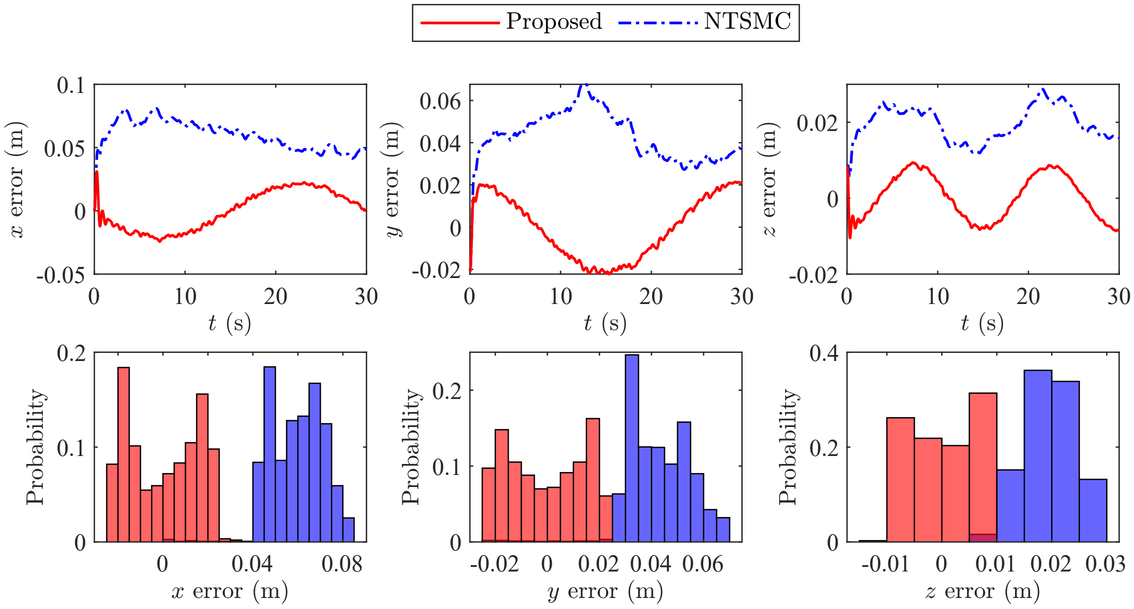

Figure 4.15: Trajectory tracking errors of a quadrotor UAV under the continuous wind

presence of continuous wind. The mean trajectory tracking error of the proposed control scheme is nearly zero, while the mean tracking error of the pure NTSMC is about $[0.06,\ 0.04,\ 0.02]^T\mathrm{m}$. This result indicates the advantage of the proposed active wind rejection control scheme.

4.5.2 Formation Control of Multiple Quadrotor UAVs in the Presence of Wind

A group of four quadrotor UAVs are simulated to cooperative monitor the central fire by hovering at the designed locations around the fire in presence of wind. Fig. 4.16 shows the communication network of the group of quadrotor UAVs. In the communication network, UAV#1 can directly exchange information with UAV#2 and UAV#4, UAV#2 can directly exchange information with UAV#1 and UAV#3, UAV#3 can directly exchange information with UAV#2 and UAV#4, and UAV#4 can directly exchange information with UAV#1 and

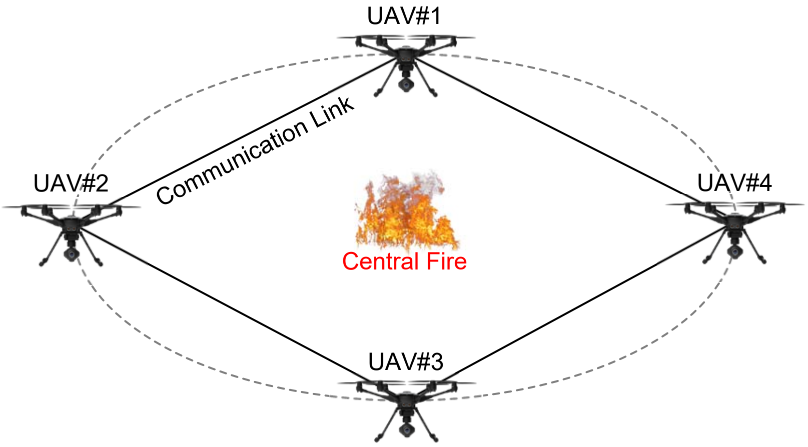

Figure 4.16: Communication network of quadrotor UAVs

UAV#3. Based on the communication network, the adjacency matrix is given by

$$\mathcal{A} = \begin{bmatrix} 0 & 1 & 0 & 1 \\ 1 & 0 & 1 & 0 \\ 0 & 1 & 0 & 1 \\ 1 & 0 & 1 & 0 \end{bmatrix} \tag{4.69}$$

The locations for fire monitoring are set as $[5,\ 0,\ 10]^T\,\mathrm{m}$ for UAV#1, $[0,\ 5,\ 10]^T\,\mathrm{m}$ for UAV#2, $[-5,\ 0,\ 10]^T\,\mathrm{m}$ for UAV#3, and $[0,\ -5,\ 10]^T\,\mathrm{m}$ for UAV#4. The parameters to yield cooperative tracking errors are set as $\lambda_{i,1} = 0.8$ and $\lambda_{i,2} = 0.2$. To evaluate the tracking performance of the proposed active wind rejection formation control of multiple quadrotor UAVs, the proposed scheme is compared with the pure NTSMC-based formation control, which is developed without active wind rejection. Simulations are conducted in the following cases:

(1) Formation hovering under wind gusts

(2) Formation Hovering under continuous winds

Formation Hovering under Wind Gusts

In this simulation, three wind gusts are rendered to act on UAV#1, UAV#2, and UAV#3, respectively, while UAV#4 encounters no wind gust. The generated wind gusts are shown in Fig. 4.17. For UAV#1, the wind gust starts at $t = 5\,\mathrm{s}$ and lasts for $3\,\mathrm{s}$, the peak value of which is $[-3,\ 3,\ 2]^T\ \mathrm{m/s}$. For UAV#2, the wind gust starts at $t = 12\,\mathrm{s}$ and lasts for $5\,\mathrm{s}$, the peak value of which is $[4,\ 3,\ 1]^T\ \mathrm{m/s}$. For UAV#3, the wind gust starts at $t = 20\,\mathrm{s}$ and lasts for $4\,\mathrm{s}$, the peak value of which is $[1,\ -3,\ 3]^T\ \mathrm{m/s}$.

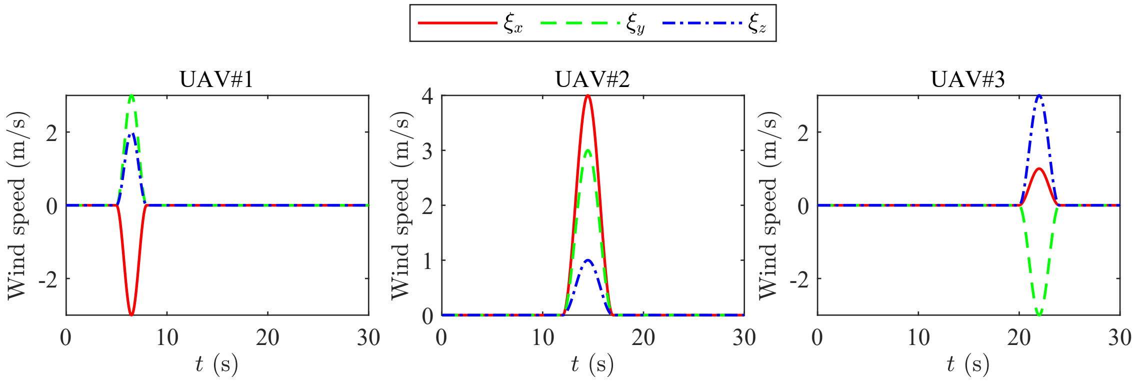

Figure 4.17: Generated wind gusts acting on multiple quadrotor UAVs

Figs. 4.18, 4.19 and 4.20 show the cooperative tracking performance of multiple quadrotor UAVs in the presence of wind gusts. Compared with the pure NTSMC-based formation control, the proposed scheme can achieve more accurate cooperative tracking performances of multiple quadrotor UAVs when encountering unknown wind gusts.

Wind effect compensation inputs and thrusts of the active wind rejection cooperative control under the wind gusts are shown in Figs. 4.21 and 4.22. It can be seen that the wind effect compensations are activated when the wind gusts are captured. Correspondingly, the quadrotor UAVs can promptly take actions to attenuate disturbances caused by the wind gusts and maintain the formation performances by using the proposed control scheme.

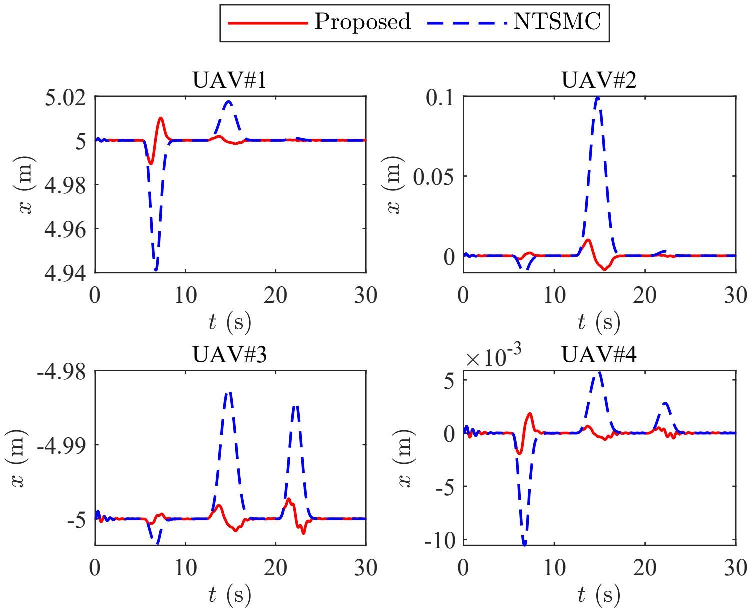

Figure 4.18: x positions of multiple quadrotor UAVs under the wind gusts

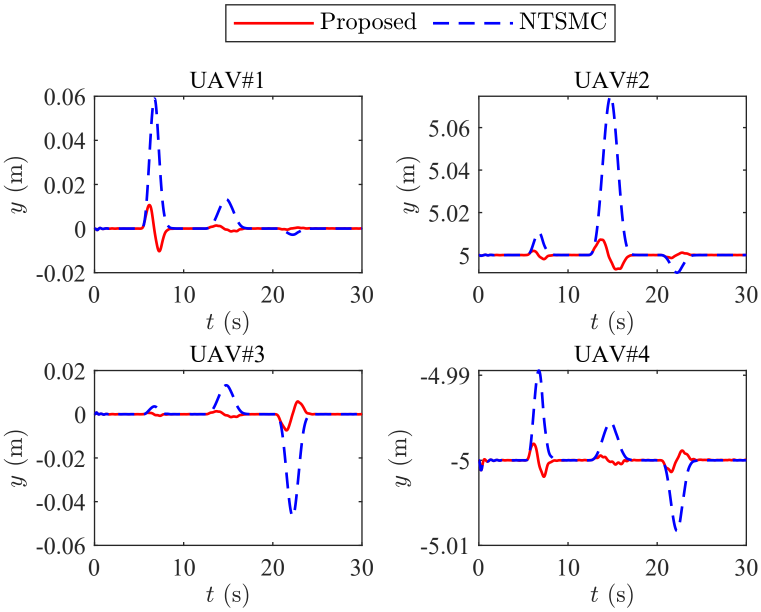

Figure 4.19: y positions of multiple quadrotor UAVs under the wind gusts

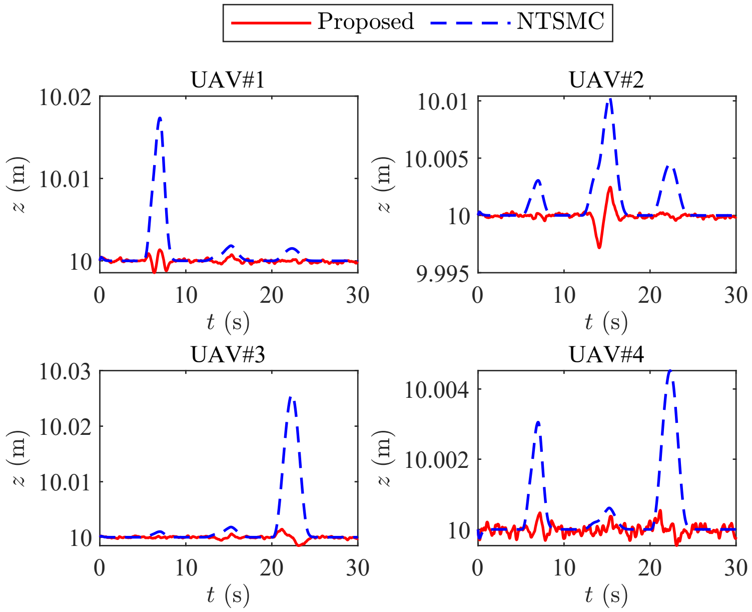

Figure 4.20: z positions of multiple quadrotor UAVs under the wind gusts

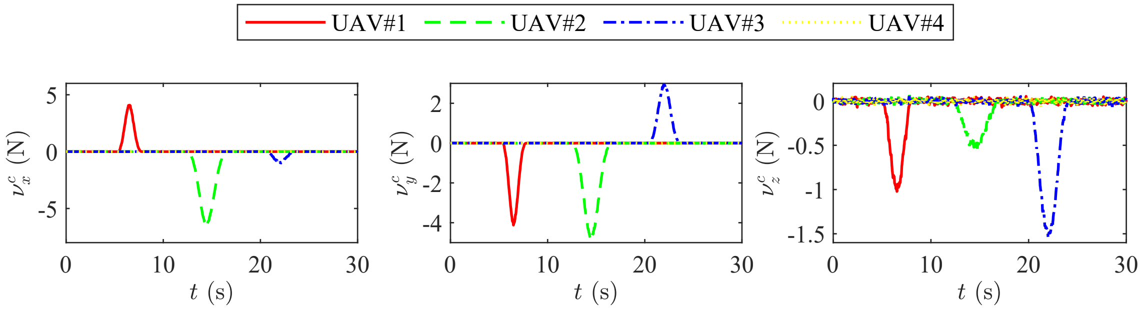

Figure 4.21: Adaptive wind effect compensation inputs under the wind gusts

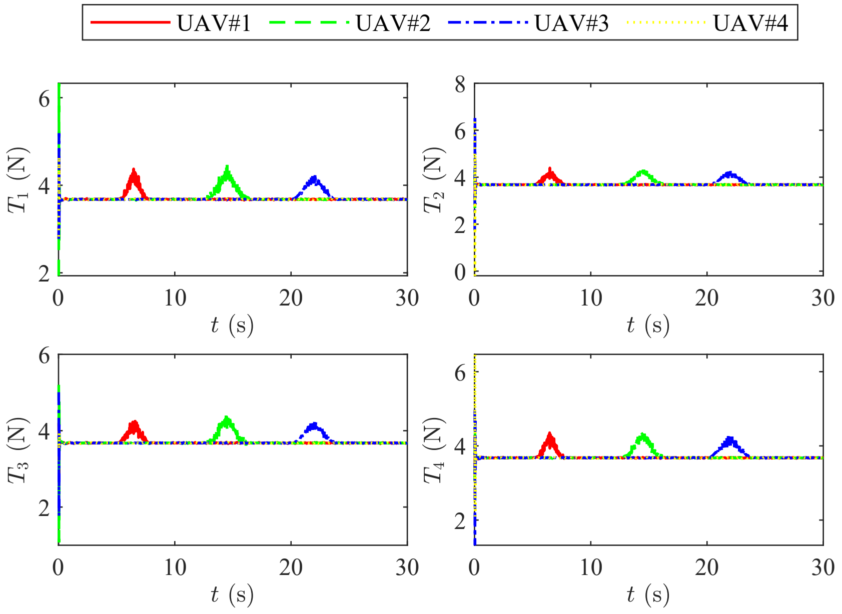

Figure 4.22: Thrusts of the active wind rejection formation control under the wind gusts

Formation Hovering under Continuous Winds

In this simulation, multiple quadrotor UAVs are commanded to hover and maintain the formation under continuous winds. Different continuous winds are encountered by the quadrotor UAVs, each of which is composed of a $[3,\ 2,\ 2]^T\ \mathrm{m/s}$ constant wind and a Dryden turbulence. The rendered continuous winds are shown in Fig. 4.23.

Figs. 4.24, 4.25 and 4.26 show the cooperative tracking performances of multiple quadrotor UAVs in the presence of continuous winds. It can be seen that the proposed control scheme can continuously attenuate the wind effects acting on multiple quadrotor UAVs to maintain the tracking performances in the presence of continuous winds in contrast to the pure NTSMC-based formation control, which results in larger tracking errors.

The adaptive wind effect compensation inputs and thrusts of the active wind rejection formation control under the continuous winds are shown in Figs. 4.27 and 4.28. These results indicate that the proposed scheme can accurately yield wind effect compensation inputs with adaptive drag coefficients to maintain the cooperative tracking performances of

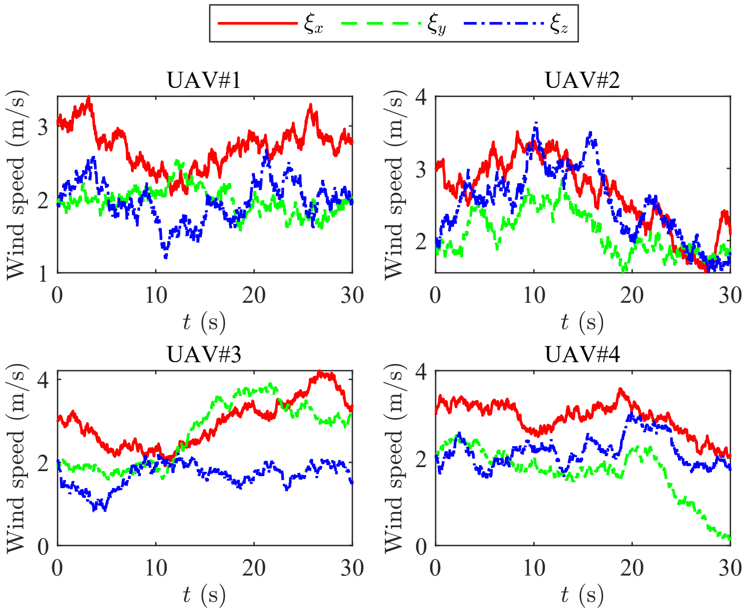

Figure 4.23: Generated continuous winds acting on multiple quadrotor UAVs

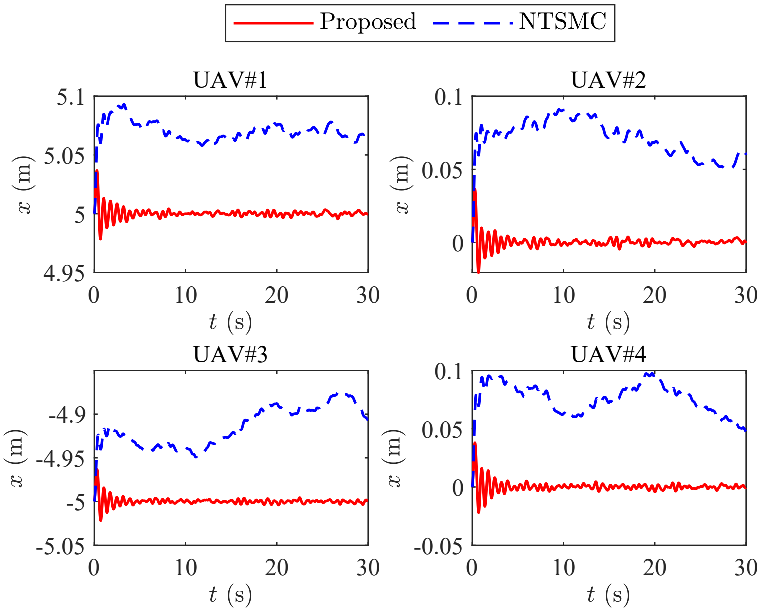

Figure 4.24: x positions of multiple quadrotor UAVs under the continuous winds

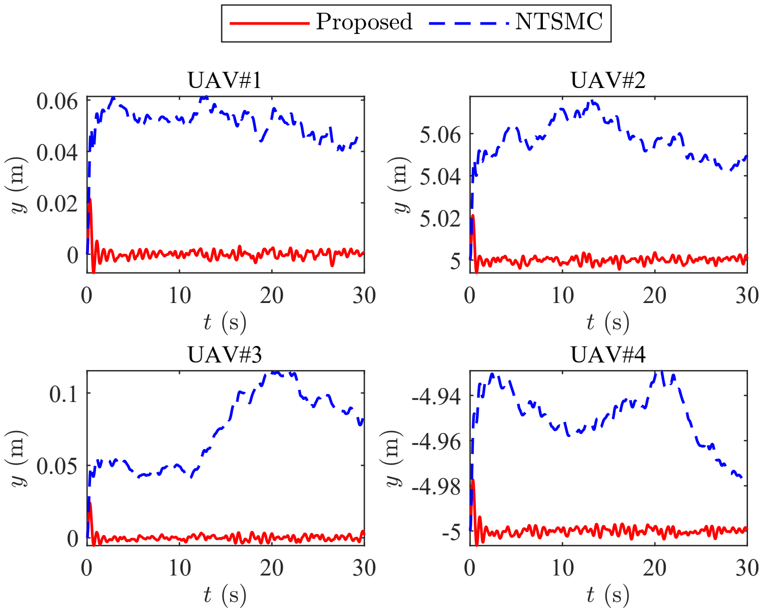

Figure 4.25: y positions of multiple quadrotor UAVs under the continuous winds

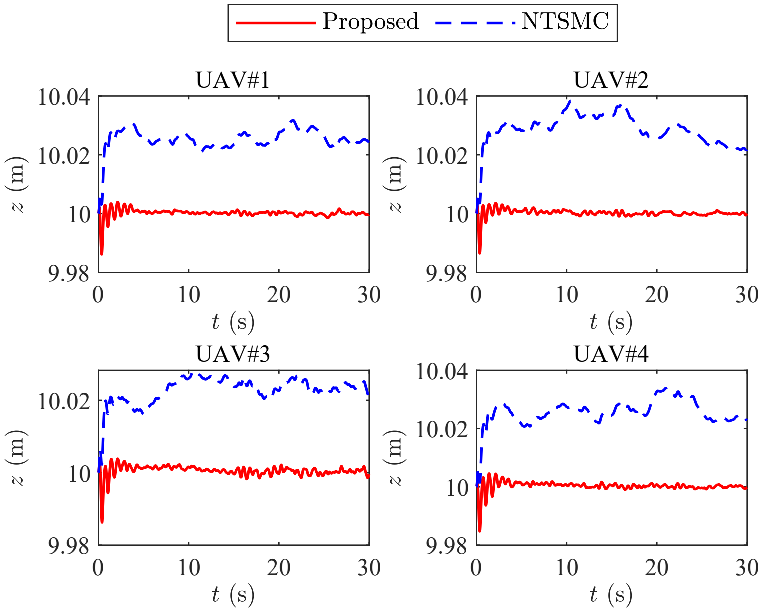

Figure 4.26: z positions of multiple quadrotor UAVs under the continuous winds

multiple quadrotor UAVs in the presence of continuous winds.

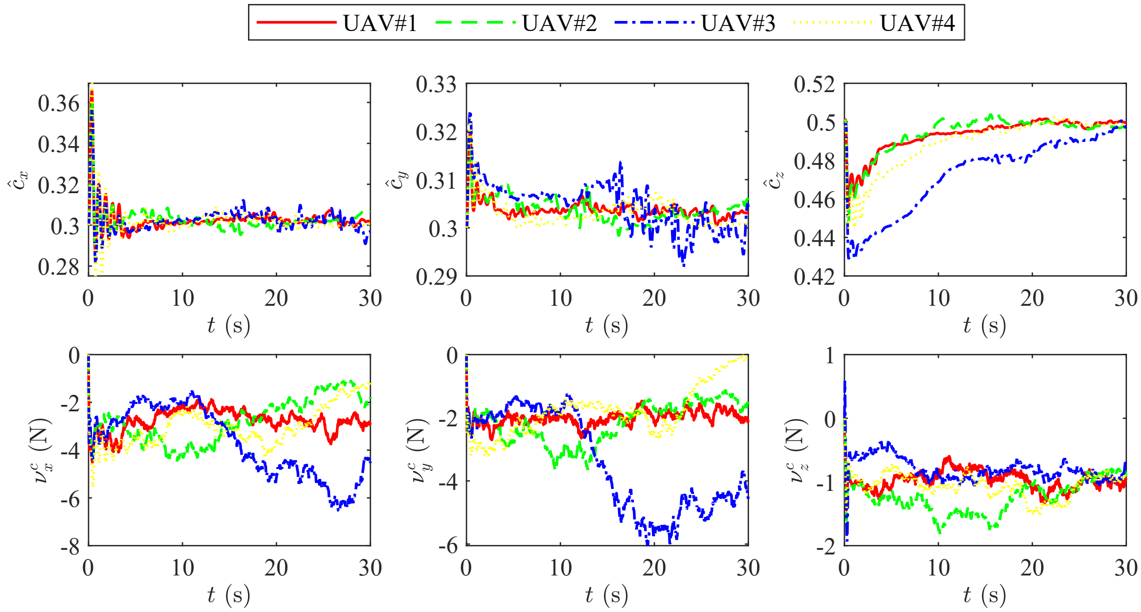

Figure 4.27: Adaptive wind effect compensation inputs under the continuous winds

4.6 Summary

In this chapter, an active wind rejection control strategy is developed for quadrotor UAVs to improve their robustness in the presence of unknown wind disturbances. Considering the wind effects acting on the dynamic model of a quadrotor UAV, an adaptive wind effect compensation method is proposed. The control system of each quadrotor UAV mainly includes the outer-loop control and the inner-loop control. The proposed outer-loop control is developed based on the nonsingular terminal sliding mode control and adaptive wind effect compensation to guarantee the finite-time convergence to the desired position in the presence of winds and generate the desired attitude signals for the inner control, while the NTSMC-based inner-loop control is designed to ensure the attitude converge to the desired attitude in the finite time. Furthermore, the proposed active wind rejection cooperative control scheme is developed to maintain the cooperative tracking performances

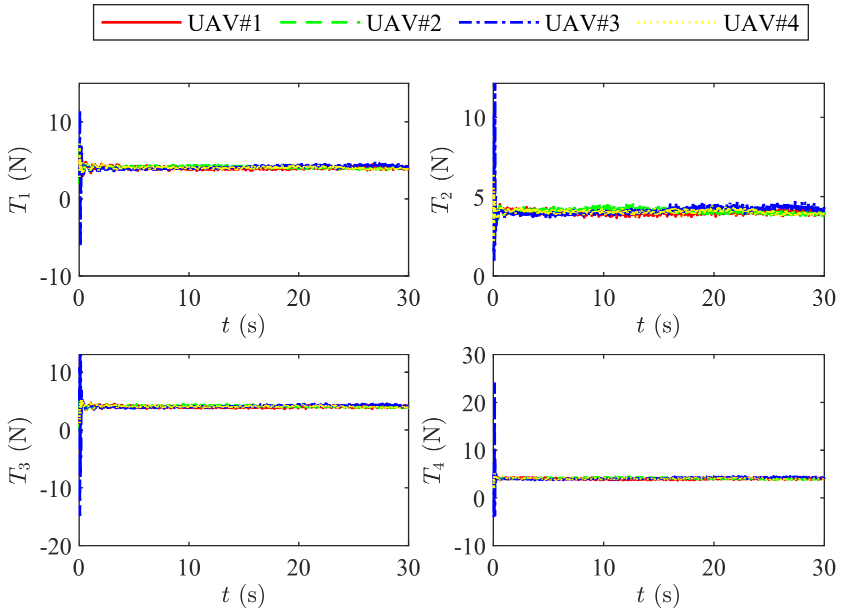

Figure 4.28: Thrusts of the active wind rejection formation control under the continuous winds

of multiple quadrotor UAVs in the presence of winds. The simulation results demonstrate the effectiveness of the proposed active wind rejection control scheme.

Chapter 5

Forest Fire Monitoring with a System of UAVs under Effect of Wind

5.1 Problem Formulation

To obtain an accurate assessment of the wind-affected forest fires, a natural thought is to estimate the forest fire propagation based on those widely used fire spread models [79, 72]. The known inputs of these models, in particular for the wind field over the forest fire region, are necessary for the accurate prediction of the forest fire burning situations. However, it is usually challenging to obtain the on-site surveys of the model inputs before the forest fire estimation. The production of the fast forest fire estimation depends on the correct field research and experimentation.

In addition, the state and parameter estimation approaches are often used to simultaneously estimate the forest fire propagation and unknown wind parameters via the observations [79, 72]. Considering the high-dimensional nonlinear and non-Gaussian forest fire model, most of the recent researches adopt the ensemble Kalman filter (EnKF) method to approximate the current states and parameters of forest fires. However, the state and parameters are implicitly assumed to follow a linear Gaussian model. Moreover, a large number of ensembles must be taken in order to retrieve accurate error statistics of the parameters and to overcome the equifinality problem.

This chapter presents an EnKF-based strategy to provide forest fire surveillance with wind measurements and fire front observations obtained with a system of UAVs. The Gaussian process regression (GPR) method is adopted to reconstruct the local wind field from wind measurements collected by UAVs. Subsequently, the wind speeds can be predicted to propagate the ensemble of fire states. Then, the proposed EnKF-based strategy can effectively estimate the forest fire situations with the observations collected by UAVs.

5.2 Wind-affected Forest Fire Monitoring Strategy Design

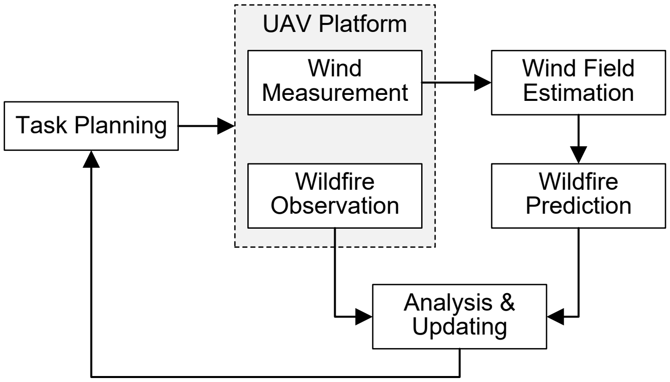

Figure 5.1: Framework of the proposed forest fire monitoring strategy

In this chapter, the forest fire monitoring strategy is proposed with a group of UAVs to provide an accurate assessment of forest fires in the unknown wind environments. The framework of the proposed strategy is demonstrated in Fig. 5.1. To achieve the purpose, the GPR method is firstly adopted to reconstruct the local wind field. Then, the optimal wind sensing locations are determined based on the maximum mutual information criterion. Subsequently, with the wind measurements collected by UAVs at these locations, the wind field estimation is updated and is used for the forest fire prediction. Finally, an EnKF-based approach is designed to evaluate the forest fire conditions via the observations. Note that since the autonomous control of UAVs is not the main concern of this paper, it is assumed that UAVs can decide their maneuvers toward the designed positions for wind measurements and fire observations.

5.2.1 Local Wind Field Reconstruction

The Gaussian process regression is adopted to reconstruct the wind field within the region of interest [97, 98]. It is assumed that the underlying function of the wind field is continuous, which can be describe as

$$\begin{aligned} \xi_x &= f_x(\boldsymbol{p}) \\ \xi_y &= f_y(\boldsymbol{p}) \end{aligned} \tag{5.1}$$

where $\boldsymbol{p} = [x,\, y]^T$ denote the coordinates of any position in the wind field, and $f_x(\cdot)$ and $f_y(\cdot)$ represent the underlying function of wind components in the x and y direction, respectively. Two separate Gaussian processes (GPs) are used to describe the distribution of wind components. The framework of the GPR-based wind field reconstruction approach is shown in Fig. 5.2. To reduce the computational complexity, the two GPs share the same hyperparameters, which means that the output space is assumed to be isotropic. For simplicity of expression, the subscript is omitted in the rest of this thesis.

In general, a GPR-based wind field model is specified by a mean function $\mu(\cdot)$ and a covariance function $k(\cdot)$, which is denoted as

$$\xi \sim \mathcal{GP}(\mu(\boldsymbol{p}),\, k(\boldsymbol{p},\, \boldsymbol{p}')) \tag{5.2}$$

where $\mu(\boldsymbol{p})$ denotes the mean function of wind speed at position $\boldsymbol{p}$, and $k(\boldsymbol{p},\, \boldsymbol{p}')$ denotes the covariance function of wind speed between positions $\boldsymbol{p}$ and $\boldsymbol{p}'$.

It is assumed that UAVs can provide point wind measurements with the proposed wind

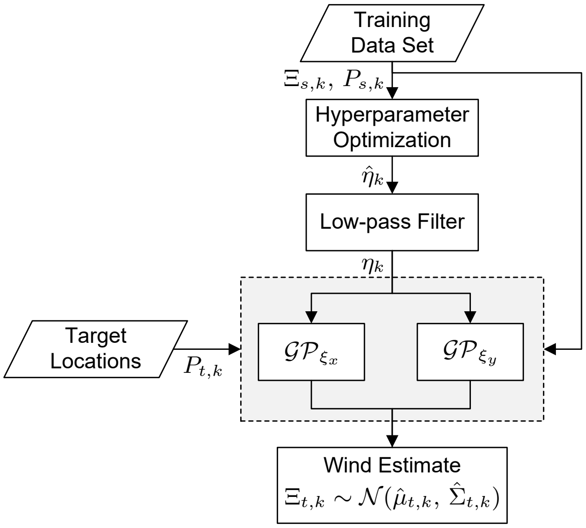

Figure 5.2: Framework of the GPR-based wind field reconstruction approach

estimation approach, and the wind sensing locations can be provided by the onboard GPS module. The noisy measurement of the wind speed for each UAV is assumed to be Gaussian

$$\bar{\xi} = f(\boldsymbol{p}_s) + \epsilon_s \tag{5.3}$$

where $\bar{\xi}$ denotes the wind measurement provided by a UAV, $\boldsymbol{p}_s$ denotes the wind sensing location, and ϵ_s is a zero-mean Gaussian noise with a variance of σ_s^2.

Therefore, the GPR-based wind field model can be trained from a finite set of wind measurements Ξ_s are taken by UAVs and the corresponding wind sensing locations P_s. It yields that the collection of wind measurements follow a multivariate Gaussian distribution

$$\Xi_s \sim \mathcal{N}(\mu_s,\ \Sigma_{ss} + \sigma_s^2 \mathrm{I}_{N_s}) \tag{5.4}$$

where μ_s denotes the mean wind speed vector, Σ_{ss} denotes the GP covariance matrix that represents the similarity of wind speeds between the wind sensing locations, and N_s denotes the number of measurements.

To estimate wind speeds Ξ_t at the target locations P_t, the joint distribution of the wind measurements Ξ_s and the wind speeds Ξ_t is given by

$$\begin{bmatrix} \Xi_s \\ \Xi_t \end{bmatrix} \sim \mathcal{N}\left(\begin{bmatrix} \mu_s \\ \mu_t \end{bmatrix}, \begin{bmatrix} \Sigma_{ss} + \sigma_s^2 \mathrm{I}_{N_s} & \Sigma_{ts}^T \\ \Sigma_{ts} & \Sigma_{tt} \end{bmatrix}\right) \tag{5.5}$$

where μ_t denotes the mean wind speed at the target positions, Σ_{tt} denotes the GP covariance matrix that represents the similarity of wind speeds between the target locations, and Σ_{ts} denotes the GP covariance matrix that represents the similarity of wind speeds between the target locations and the wind sensing locations.

Subsequently, the wind estimates at the target locations follow a multivariate Gaussian distribution $\Xi_t | P_t,\, \Xi_s,\, P_s \sim \mathcal{N}(\hat{\mu}_t,\, \hat{\Sigma}_t)$, the estimated mean and covariance of which are given by

$$\begin{cases} \hat{\mu}_t = \mu_t + \Sigma_{ts}^T [\Sigma_{ss} + \sigma_s^2 \mathrm{I}_{N_s}]^{-1} (\Xi_s - \mu_s) \\ \hat{\Sigma}_t = \Sigma_{tt} - \Sigma_{ts}^T [\Sigma_{ss} + \sigma_s^2 \mathrm{I}_{N_s}]^{-1} \Sigma_{ts} \end{cases} \tag{5.6}$$

where $\hat{\mu}_t$ and $\hat{\Sigma}_t$ are the mean and covariance of estimated wind speeds at the target locations.

In the GPR-based wind field model, the mean function is often assumed to be zero because offsets and simple trends can be subtracted out by preprocessing. With the assumption that the input dimensions are isotropic, a classic squared exponential covariance function is introduced as

$$k(\boldsymbol{p},\, \boldsymbol{p}') = \sigma_f^2 \exp(-\frac{1}{2l^2} \|\boldsymbol{p} - \boldsymbol{p}'\|^2) \tag{5.7}$$

where σ_f^2 is the signal variance and l is the length scale. Let $\eta = [\sigma_f,\, l]^T$ denote the hyperparameter set. It can be observed that the estimated mean and covariance are specified by the hyperparameters. Considering the hyperparameters, the negative log marginal likelihood of the wind measurements is given by

$$\begin{aligned}\mathcal{L} =& -\log p(\Xi_s|\eta) \\ =& \frac{1}{2}\Xi_s^T \Sigma_\eta^{-1} \Xi_s + \frac{1}{2}\log\det(\Sigma_\eta) + \frac{N_s}{2}\log 2\pi\end{aligned} \tag{5.8}$$

where $\Sigma_\eta = \Sigma_{ss} + \sigma_s^2 \mathrm{I}_{N_s}$. By using the maximum marginal likelihood approach, the selection of these hyperparameters can be optimized via the training data set.

With the wind measurements provided by a group of UAVs at each time step, the hyperparameters for the GPR-based wind field model should be updated from the newly obtained wind measurements. In the case of the high-frequency noise existing in the wind measurements, a low-pass filter is designed to smooth the transition of the hyperparameters

$$\begin{cases} \sigma_{f,k} =& \lambda_{\sigma_f}\sigma_{f,k-1} + (1-\lambda_{\sigma_f})\hat{\sigma}_{f,k} \\ l_k =& \lambda_l l_{k-1} + (1-\lambda_l)\hat{l}_k \end{cases} \tag{5.9}$$

where $(\sigma_{f,k},\ l_k)$ are the smoothed hyperparameters at time instant t_k, $(\hat{\sigma}_{f,t},\ \hat{l}_t)$ are the estimated hyperparameters at time instant t_k, and $(\lambda_{\sigma_f},\ \lambda_l)$ are the smoothing coefficients in the range of $(0,\ 1)$.

5.2.2 Optimal Wind Sensing Locations

The Gaussian process method has been widely used to model unknown environmental fields [99] and cope with the optimal sampling point selection problem [100]. As an advantage of the GPR-based wind field estimation, the estimated covariance of wind speeds at the target locations can be provided, which represents the uncertainty of wind prediction. To obtain the maximum amount of wind information at these target locations, the optimal wind sensing locations should be determined for the UAVs.

To quantify the amount of uncertainty, the differential information entropy is introduced as

$$H(x) = -\int p(x)\log p(x)\mathrm{d}x \tag{5.10}$$

Since the prior distribution of wind speeds at the target locations follow a multivariate Gaussian distribution $\Xi_t \sim \mathcal{N}(0,\, \Sigma_{tt})$, the information entropy of wind speeds at the target locations can be calculated as

$$H(\Xi_t) = \frac{1}{2}\log\det(\Sigma_{tt}) + \frac{N_t}{2}(\log 2\pi + 1) \tag{5.11}$$

where N_t denotes the number of target locations.

If the wind measurements and the wind sensing locations are given, to quantify the reduction of uncertainty of Ξ_t conditioning on Ξ_s, the mutual information can be calculated as

$$\begin{aligned} I(\Xi_t;\, \Xi_s) =& H(\Xi_t) - H(\Xi_t|\Xi_s) \\ =& H(\Xi_t) + H(\Xi_s) - H(\Xi_t,\, \Xi_s) \\ =& \frac{1}{2}\log\frac{\det(\Sigma_1)\det(\Sigma_2)}{\det(\Sigma_3)} \end{aligned} \tag{5.12}$$

where

$$\begin{cases} \Sigma_1 =& \Sigma_{tt} \\ \Sigma_2 =& \Sigma_{ss} + \sigma_s^2 \mathrm{I}_{N_s} \\ \Sigma_3 =& \begin{bmatrix} \Sigma_{ss} + \sigma_s^2\mathrm{I}_{N_s} & \Sigma_{ts}^T \\ \Sigma_{ts} & \Sigma_{tt} \end{bmatrix} \end{cases} \tag{5.13}$$

Therefore, the optimal wind sensing locations can be determined by maximizing the mutual information. It is worth noting that the determination of the optimal wind sensing locations is dependent on the selection of target locations, the number of wind sensing locations, and the prior knowledge about the GPR-based wind field model, i.e., the prior knowledge on the hyperparameters. On the other hand, once the wind measurements are provided at these optimal wind sensing locations, the GPR-based wind field model can be updated for the wind prediction.

5.2.3 Forest Fire Monitoring Scheme Based on Ensemble Kalman Filter

In order to facilitate the design of EnKF for forest fire monitoring, the fire state vector, which is composed of the two-dimensional coordinates of N_f fire points at time instant t_k, is defined as

$$\boldsymbol{x}_k^f = [(q_{x,1},\, q_{y,1}),\, (q_{x,2},\, q_{y,2}),\, \cdots,\, (q_{x,N_f},\, q_{y,N_f})]^T \tag{5.14}$$

Correspondingly, the wind vector that induces the propagation of these fire points is defined as

$$\boldsymbol{\xi}_k^f = [(\xi_{x,1},\, \xi_{y,1}),\, (\xi_{x,2},\, \xi_{y,2}),\, \cdots,\, (\xi_{x,N_f},\, \xi_{y,N_f})]^T \tag{5.15}$$

With the fire observations collected by UAVs, the observation vector of these fire points is defined as

$$\boldsymbol{z}_k^f = [(q_{x,1}^o,\, q_{y,1}^o),\, (q_{x,2}^o,\, q_{y,2}^o),\, \cdots,\, (q_{x,N_f}^o,\, q_{y,N_f}^o)]^T \tag{5.16}$$

Considering the insuperable uncertainties in both forest fire predictions and the observations, the ensemble Kalman filter is designed to evaluate the status of forest fire via observations. The EnKF algorithm is a sampling-based approach, which is advantageous for solving extremely high-dimensional, possibly nonlinear, and non-Gaussian state estimation problems.

In the EnKF process, an ensemble of N_e state vectors are propagated through the fire spread model. To predict the forest fire spread, the current estimates of wind speeds are required. Given the current coordinate estimates of the fire points, the wind estimates can be sampled via the GPR-based wind field model

$$\boldsymbol{\xi}_{k|k-1}^{f(j)} \sim p(\boldsymbol{\xi}_{k|k-1}^f | \boldsymbol{x}_{k-1|k-1}^{f(j)}) \tag{5.17}$$

where $j = 1,\ 2,\ \cdots,\ N_e$.

Then, based on the fire spread model, the ensembles of forest fire states can be propagated as

$$\boldsymbol{x}^{f(j)}_{k|k-1} = f(\boldsymbol{x}^{f(j)}_{k-1|k-1},\ \boldsymbol{\xi}^{f(j)}_{k|k-1}) + \boldsymbol{\omega}^{f(j)}_{k-1} \tag{5.18}$$

where $\boldsymbol{\omega}^{f(j)}_{k} \sim \mathcal{N}(0,\ Q_f)$ denotes the process noise vector in the forest fire propagation.

Based on the state ensemble prediction, the predicted observations can be obtained as

$$\boldsymbol{z}^{f(j)}_{k|k-1} = h(\boldsymbol{x}^{f(j)}_{k|k-1}) + \boldsymbol{v}^{f(j)}_{k} \tag{5.19}$$

where $\boldsymbol{v}^{f(j)}_{k} \sim \mathcal{N}(0,\ R_f)$ denotes the observation noise vector.

To update the ensemble of predicted state vectors with the fire observations collected by UAVs, the computation of the EnKF gain is required. The optimal gain is approximated from the prediction ensembles Eqs. (5.18) and (5.19).

The mean of the propagated state ensemble and the predicted observation ensemble can be obtained as

$$\begin{cases} \boldsymbol{x}^{f}_{k|k-1} &= \dfrac{1}{N_e} \displaystyle\sum_{j=1}^{N_e} \boldsymbol{x}^{f(j)}_{k|k-1} \\ \boldsymbol{z}^{f}_{k|k-1} &= \dfrac{1}{N_e} \displaystyle\sum_{j=1}^{N_e} \boldsymbol{z}^{f(j)}_{k|k-1} \end{cases} \tag{5.20}$$

Then, the cross-covariance between the propagated states and predicted observations and the covariance of predicted observation can be computed as

$$\begin{cases} C^{xz}_{k} &= \dfrac{1}{N_e - 1} \displaystyle\sum_{j=1}^{N_e} (\boldsymbol{x}^{f}_{k|k-1} - \boldsymbol{x}^{f(j)}_{k|k-1})(\boldsymbol{z}_{k|k-1} - \boldsymbol{z}^{f(j)}_{k|k-1}) \\ C^{zz}_{k} &= \dfrac{1}{N_e - 1} \displaystyle\sum_{j=1}^{N_e} (\boldsymbol{z}^{f}_{k|k-1} - \boldsymbol{z}^{f(j)}_{k|k-1})(\boldsymbol{z}^{f}_{k|k-1} - \boldsymbol{z}^{f(j)}_{k|k-1}) \end{cases} \tag{5.21}$$

Thus, the EnKF gain can be computed as

$$K_k = C_k^{xz}(C_k^{zz} + R_f)^{-1} \tag{5.22}$$

Algorithm 2: The proposed EnKF-based forest fire monitoring approach

```
Input: Observation of forest fire $\boldsymbol{z}_k$ and the GPR-based wind field model $p(\boldsymbol{\xi}_k^f|\boldsymbol{x}_k^f)$
Output: Estimates of fire states $\hat{\boldsymbol{x}}_k^f$
Initialize the ensemble of forest fire states $\{\boldsymbol{x}_0^{f(j)}\}_{j=1}^{N_e}$;
for $k \leftarrow 1$ to Number of time steps do
    Prediction:
    Sample $\boldsymbol{\xi}_{k|k-1}^{f(j)} \sim p(\boldsymbol{\xi}_{k|k-1}^f|\boldsymbol{x}_{k-1|k-1}^{f(j)})$;
    Propagate $\boldsymbol{x}_{k|k-1}^{f(j)} \leftarrow f(\boldsymbol{x}_{k-1|k-1}^{f(j)}, \boldsymbol{\xi}_{k|k-1}^{f(j)}) + \boldsymbol{\omega}_k^{f(j)}$;
    Predict $\boldsymbol{z}_{k|k-1}^{f(j)} \leftarrow h(\boldsymbol{x}_{k|k-1}^{f(j)}) + \boldsymbol{\upsilon}_k^{f(j)}$;
    Update:
    $\boldsymbol{x}_{k|k-1}^f \leftarrow \frac{1}{N_e}\sum_{j=1}^{N_e} \boldsymbol{x}_{k|k-1}^{f(j)}$;
    $\boldsymbol{z}_{k|k-1}^f \leftarrow \frac{1}{N_e}\sum_{j=1}^{N_e} \boldsymbol{z}_{k|k-1}^{f(j)}$;
    $C_k^{xz} \leftarrow \frac{1}{N_e-1}\sum_{j=1}^{N_e}(\boldsymbol{x}_{k|k-1}^f - \boldsymbol{x}_{k|k-1}^{f(j)})(\boldsymbol{z}_{k|k-1}^f - \boldsymbol{z}_{k|k-1}^{f(j)})^T$;
    $C_k^{zz} \leftarrow \frac{1}{N_e-1}\sum_{j=1}^{N_e}(\boldsymbol{z}_{k|k-1}^f - \boldsymbol{z}_{k|k-1}^{f(j)})(\boldsymbol{z}_{k|k-1}^f - \boldsymbol{z}_{k|k-1}^{f(j)})^T$;
    Compute gain $K_k \leftarrow C_k^{xz}(C_k^{zz} + R_f)^{-1}$;
    Update $\boldsymbol{x}_{k|k}^{f(j)} \leftarrow \boldsymbol{x}_{k|k-1}^{f(j)} + K_k(\boldsymbol{z}_k^f - \boldsymbol{z}_{k|k-1}^{f(j)})$;
    Estimate $\hat{\boldsymbol{x}}_k^f \approx \frac{1}{N_e}\sum_{j=1}^{N_e} \boldsymbol{x}_{k|k}^{f(j)}$
end
```

With this gain, the ensemble of propagated states can be updated as

$$\boldsymbol{x}_{k|k}^{f(j)} = \boldsymbol{x}_{k|k-1}^{f(j)} + K_k(\boldsymbol{z}_k^f - \boldsymbol{z}_{k|k-1}^{f(j)}) \tag{5.23}$$

Finally, the estimate of forest fire state can be approximated as

$$\hat{\boldsymbol{x}}_k^f \approx \frac{1}{N_e}\sum_{j=1}^{N_e} \boldsymbol{x}_{k|k}^{f(j)} \tag{5.24}$$

To better understand the proposed EnKF-based forest fire monitoring approach, the pseudo code is given in Algorithm 2.

5.3 Simulation Results

In this section, simulations are conducted to demonstrate the effectiveness of the proposed forest fire monitoring strategy in the presence of unknown wind environments.

To generate wind environments for simulations, a horizontal wind field at the altitude of $h_r = 50\,\mathrm{m}$ above the vegetation is defined as

$$\begin{bmatrix} \xi_x \\ \xi_y \end{bmatrix} = \begin{bmatrix} a\sin^2(\frac{x}{50}) + b\cos^2(\frac{y}{50}) + \epsilon \\ a\cos(\frac{x}{50}) + b\sin(\frac{y}{50}) + \epsilon \end{bmatrix} \tag{5.25}$$

where $a = 4$ and $b = 3$. ϵ is a zero-mean Gaussian noise with a variance of $\sigma_\epsilon^2 = 0.01\,(\mathrm{m/s})^2$ that represents the uncertainty of wind speeds.

The propagation of fire front is simulated based on the fire spread model Eq. (2.19). The parameters of the model are set as $h_f = 1.5\,\mathrm{m}$, $R_0 = 1\,\mathrm{m/s}$, $\beta = 0.002$, and $\sigma = 4000\,\mathrm{m}^{-1}$. The initial fire front has an arbitrary shaped boundary, which is described as

$$\begin{cases} q_{x,0} = r \cdot \cos\alpha \\ q_{x,0} = r \cdot \sin\alpha \end{cases} \tag{5.26}$$

where $\alpha \in [0,\ 2\pi]$ and $r = r_0 + k_s(\sin 6\alpha + \sin 3\alpha)$. In the simulations, parameters for the initial fire front are set as $r_0 = 100\,\mathrm{m}$ and $k_s = 5\,\mathrm{m}$. By evenly sampling α, the continuous fire front is discreted by $N_f = 40$ fire points. Fig. 5.3 shows the forest fire spread in the self-defined wind field.

UAVs are commanded to provide wind measurements and forest fire observation at the altitude of $50\,\mathrm{m}$. The variances of wind measurement noise and forest fire observation noise are set as $\sigma_s^2 = 0.01\,(\mathrm{m/s})^2$ and $\sigma_v^2 = 1\,\mathrm{m}^2$. To determine the optimal wind sensing

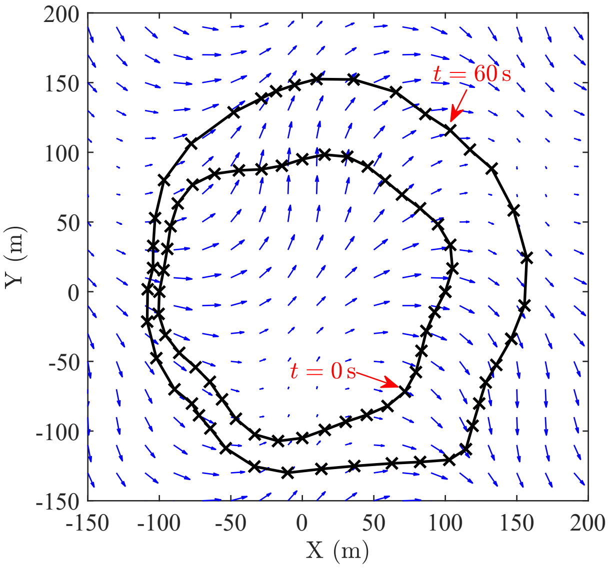

Figure 5.3: Illustration of forest fire spread in the self-defined wind field

locations, the prior knowledge of the hyperparameters are set as $\sigma_f = 5\,\mathrm{m/s}$ and $l = 100\,\mathrm{m}$. When arriving at the desired positions, UAVs are set to collect wind measurements and forest fire observations at a frequency of $1\,\mathrm{Hz}$. The smoothing coefficients for the hyperparameters are set as $\lambda_{\sigma_f} = 0.1$ and $\lambda_l = 0.1$.

5.3.1 Forest Fire Monitoring with Regional Wind Field Estimation

In this simulation, the performance of the proposed strategy is evaluated with the regional wind field estimation. The region of interest is defined as a scalar field $\{(x, y)| - 150\,\mathrm{m} \leq x \leq 200\,\mathrm{m}, -150\,\mathrm{m} \leq y \leq 200\,\mathrm{m}\}$ with a resolution of $50\,\mathrm{m}$ in each direction. The actual wind field with target locations is shown in Fig. 5.4.

In order to demonstrate the effectiveness of the GPR-based wind field estimation, the estimation results of 10, 20, and 40 wind sensing locations are compared. Given the number of wind sensing locations, the optimal wind sensing locations can be obtained by using the maximum mutual information criterion. The predicted mean wind fields are shown in Fig. 5.5. It can be observed that the more available wind measurements collected by UAVs

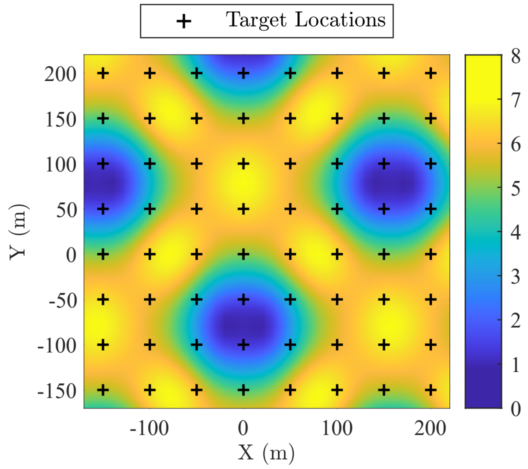

Figure 5.4: Actual wind field with target locations

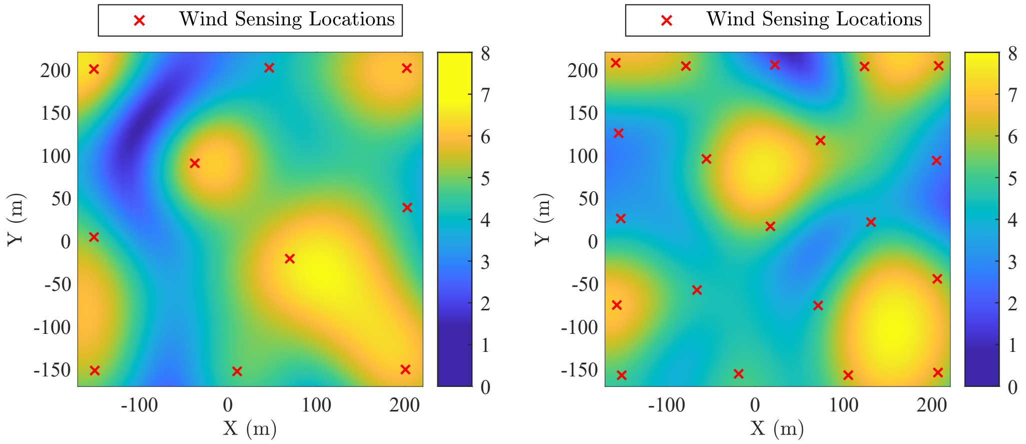

(a) $N_s = 10$ (b) $N_s = 20$

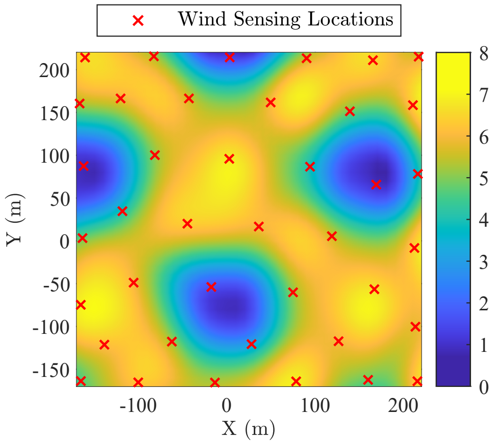

(c) $N_s = 40$

Figure 5.5: Predicted mean wind field with different numbers of wind measurements

results in the better wind field estimation. However, in the case of insufficient measurements, it will cause an underfitting problem for the regional wind field estimation. With the estimated wind fields, the forest fire spread can be predicted. Fig. 5.6 shows the prediction of forest fire spread at $t = 60\,\mathrm{s}$. The results of forest fire prediction suggest that the regional wind field estimation can provide valuable information for the forest fire prediction, but the performance of the forest fire prediction still depends on the accuracy of the wind field estimation within the region of interest.

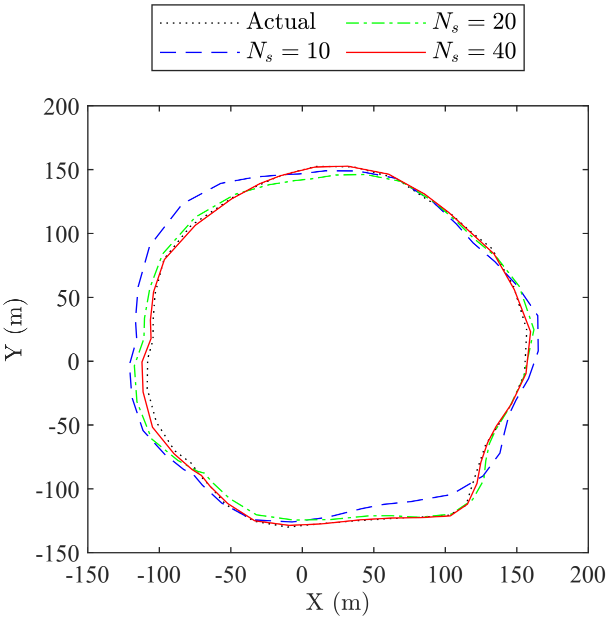

Figure 5.6: Prediction of forest fire spread at $t = 60\,\mathrm{s}$

With the EnKF, the prediction of forest fire spread can be updated via the fire observations collected by UAVs. Fig. 5.7 shows the estimation of fire front with EnKF at $t = 60\,\mathrm{s}$. A comparison of forest fire spread prediction and estimation are demonstrated in Fig. 5.8. The mean distances and the root mean squared (RMS) distances of the fire front estimation to the actual fire front decrease, compared with those of the forest fire prediction without observation update. This is due to the fact that with the fire observations collected by UAVs, the prediction errors that are caused by the wind field estimation errors and uncertainties of the forest fire spread model can be reduced by the EnKF.

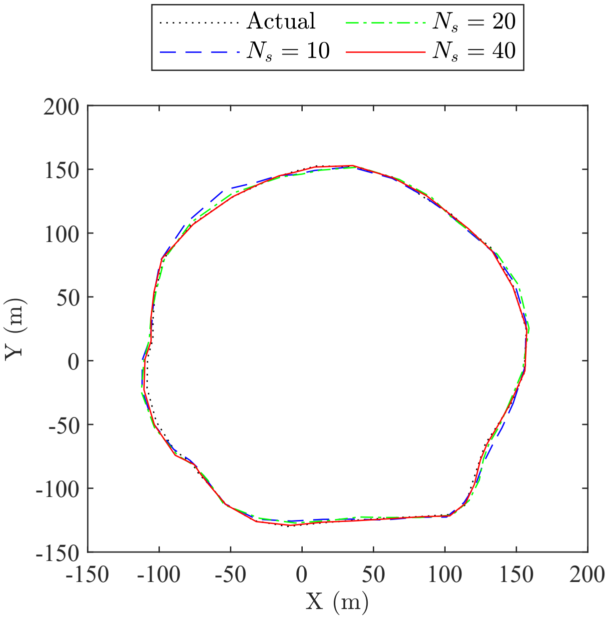

Figure 5.7: Estimation of forest fire spread with EnKF at $t = 60\,\mathrm{s}$

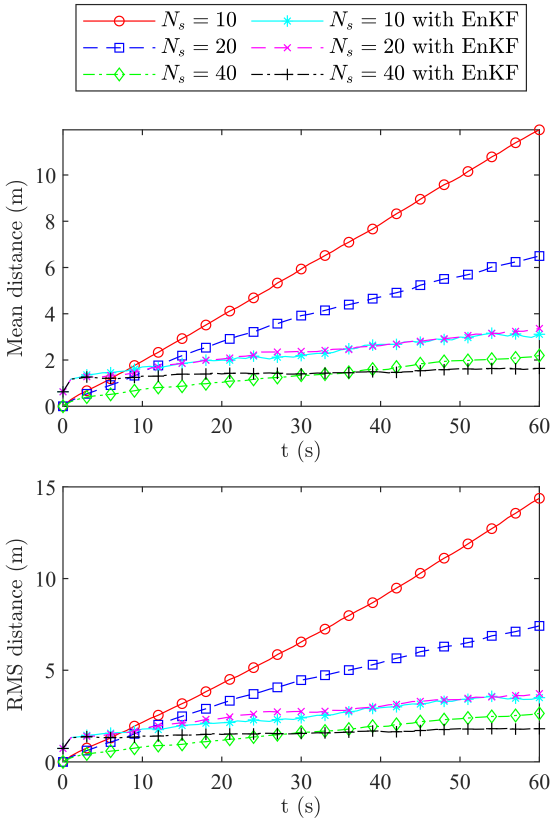

Figure 5.8: Comparison of forest fire spread prediction and estimation

5.3.2 Forest Fire Monitoring with Specific Focus on the Fire Front

In this simulation, the wind field is estimated with specific focus on the fire front, i.e., the discrete fire points on the fire front are set as the target locations for the wind field estimation. To avoid the underfitting problem caused by insufficient wind measurements, the number of the wind sensing locations is set as $N_s = 20$.

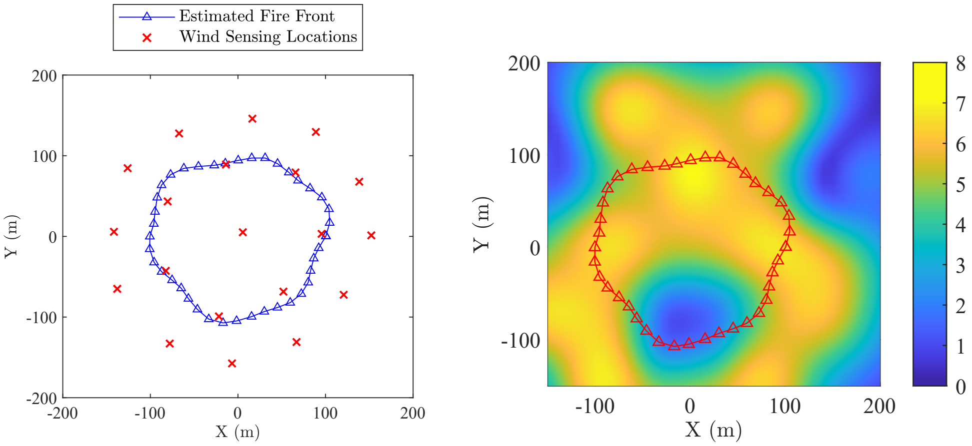

Figure 5.9: Wind field and forest fire estimation with specific focus on the fire front at $t = 0\,\mathrm{s}$

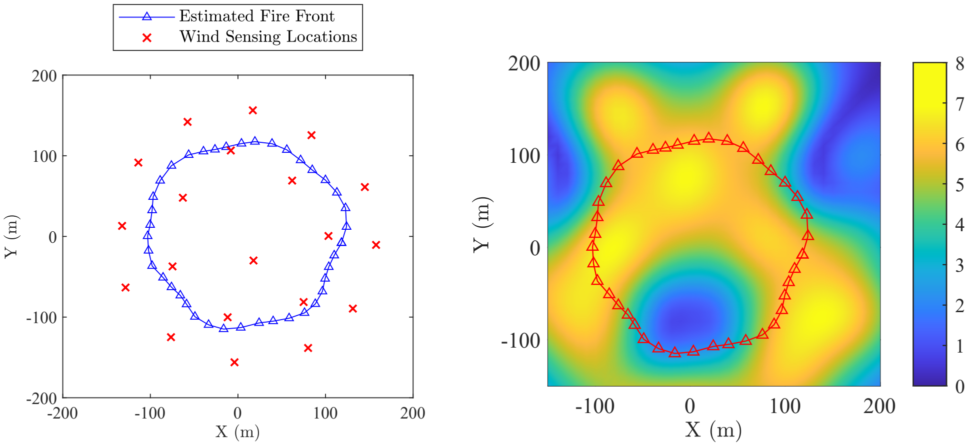

Figure 5.10: Wind field and forest fire estimation with specific focus on the fire front at $t = 20\,\mathrm{s}$

Figs. 5.9-5.12 show the simulations of wind field and forest fire estimation with specific focus on the fire front. The optimal wind sensing locations are updated according to

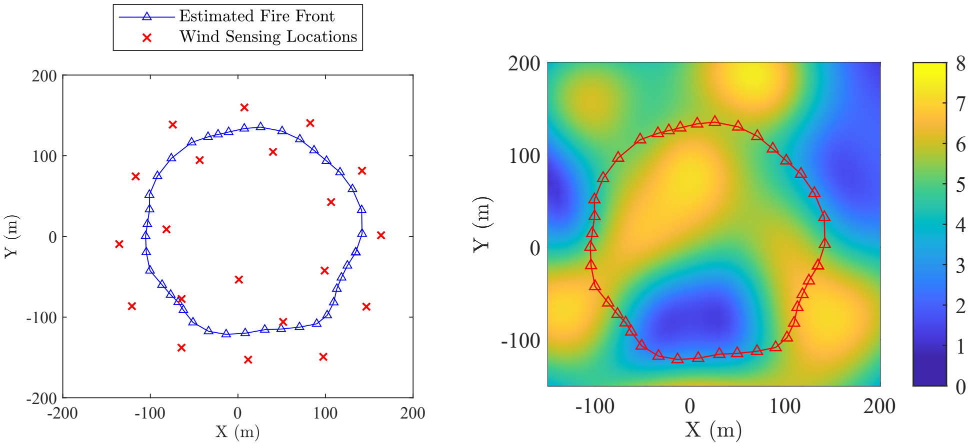

Figure 5.11: Wind field and forest fire estimation with specific focus on the fire front at $t = 40\,\mathrm{s}$

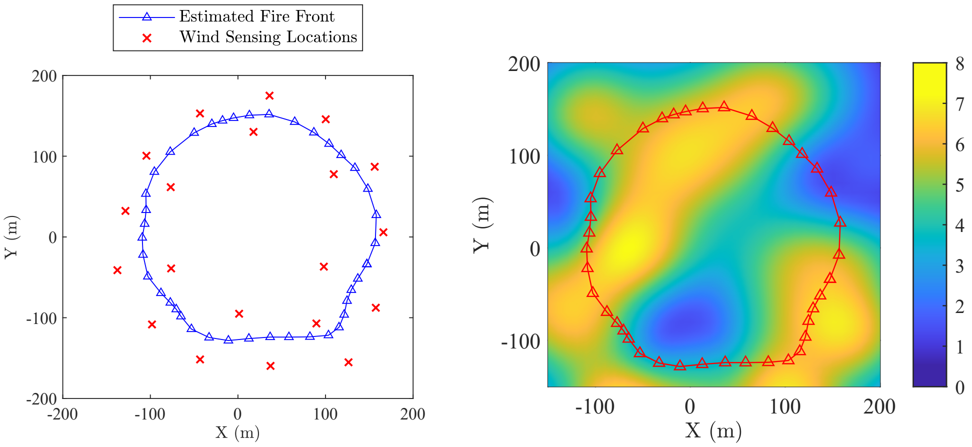

Figure 5.12: Wind field and forest fire estimation with specific focus on the fire front at $t = 60\,\mathrm{s}$

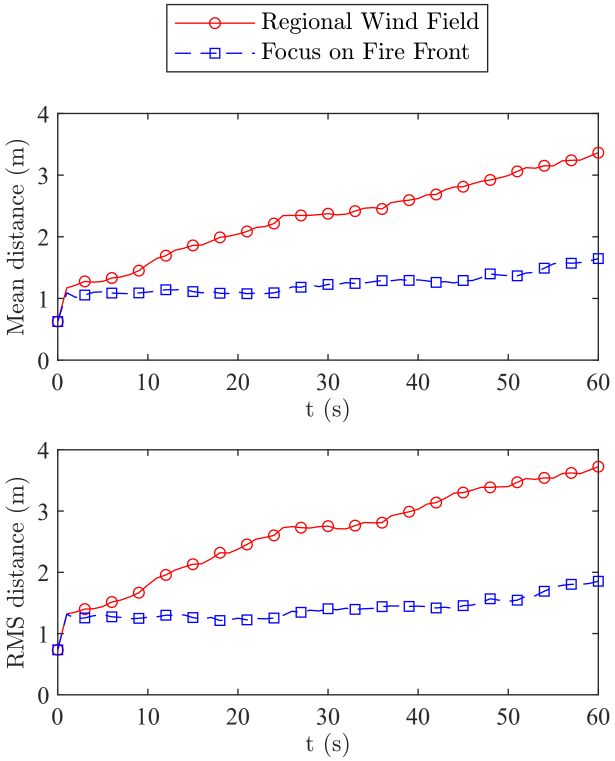

Figure 5.13: Comparison of forest fire estimation with regional wind field and specific focus on the fire front

the spreading fire points. It can be seen that with specific focus on the fire front, the wind sensing locations are spread out with the propagation of the forest fire to satisfy the objectives. Correspondingly, the wind field near the fire front can be estimated with a higher accuracy. Fig. 5.13 shows that with specific focus on the fire front, the mean distance and RMS distance to the actual fire front both decrease. This result indicates the method can improve the estimation accuracy of the border region of the forest fire as it keep expanding.

5.4 Summary

This chapter presents an EnKF-based strategy to estimate the forest fires with wind measurements and fire observations collected by multiple UAVs. Using the Gaussian process regression method, the local wind field model is reconstructed based on the wind measurements to provide predictions of wind components for the fire prediction. Then, to improve the wind field estimation for the forest fire monitoring, the locations of wind sensing are optimized with the maximum mutual information method. Based on the Rothermel's fire spread model, the propagation of the forest fire front is estimated in the ensemble Kalman filter framework. The simulation results demonstrate the effectiveness of the proposed forest fire monitoring strategy.

Chapter 6

Conclusions and Future Works

6.1 Conclusions

In this thesis, the wind estimation from quadrotor motion, the active wind rejection control of quadrotor UAVs and the forest fire monitoring approach with a group of UAVs are investigated. To summarize, several major conclusions are drawn as follows:

(1) The proposed two-stage particle filter-based wind estimation approach can extract wind vectors from quadrotor motion without additional wind sensors. By adopting the cascaded structure, the accuracy and the computational efficiency of the particle filter procedure can be improved.

(2) Compared with the wind triangle wind estimation algorithm, the proposed approach can effectively estimate wind vectors based on the nonlinear dynamic model of a quadrotor UAV and reduce the adverse impact of measurement noise and produce more accurate estimation results.

(3) The proposed wind rejection control can actively compensate for the external wind disturbances acting on the UAV dynamics based on the explicit wind estimation obtained from the two-stage particle filter. By using an adaptive nonsingular terminal

sliding mode control, one can attenuate the lumped disturbances, including wind estimation errors and model uncertainties. Moreover, the proposed active wind rejection cooperative control can improve the formation flight performances of multiple quadrotor UAVs in the presence of unknown winds.

(4) Compared with the pure adaptive NTSMC, the designed controller with active wind rejection mechanism can promptly get a response to the time-varying winds so as to guarantee the tracking performance and stability of quadrotor UAVs against the unexpected wind disturbances.

(5) The proposed wind field reconstruction approach based on the Gaussian process regression method can retrieve the wind field over the forest fire region with the wind data collected by UAVs. The optimal wind sensing locations can be determined via the designed algorithm for a group of UAVs to collect wind data, where the maximum amount of wind information can be obtained.

(6) The proposed ensemble Kalman filter-based forest fire monitoring approach with the wind field reconstruction can accurately assess the status of wind-affected forest fires. The proposed method can sample wind data from a multivariate Gaussian distribution related to the fire front locations to overcome the challenge of obtaining wind input data for forest fire estimation.

6.2 Future Works

This thesis mainly focuses on the wind estimation and control of UAVs with application to forest fire surveillance. In the future, more effort should be devoted to the studies in the related fields. Based on the current research in this thesis, several future directions are outlined as follows:

(1) The proposed wind estimation approach and wind rejection control strategy are dependent on the quadrotor aerodynamic model considering wind effects. However, the current challenge is how to obtain the accurate aerodynamic representation of the aircraft. Therefore, the accurate model of a quadrotor UAV is worth further investigation.

(2) The wind estimation approach and wind rejection control are investigated without considering more complicated and challenging issues, such as sensor faults, actuator faults, and computation and communication limitations, which are expected to be studied in the future work.

(3) The proposed forest fire monitoring approach relies on the forest fire spread model and the interaction between winds and fires. As a result, the fire spread model should be further investigated in the future to improve the accuracy of estimation.

(4) The observations of forest fire states are assumed to be perfectly obtained in this thesis, while more work should be done for the identification and localization of fire front locations with UAVs.

(5) Although the proposed approaches are validated in simulations, their effectiveness should be further validated by real flight experiments.

Bibliography

[1] Z. Liu, Y. Zhang, X. Yu, and C. Yuan, "Unmanned surface vehicles: An overview of developments and challenges," *Annual Reviews in Control*, vol. 41, pp. 71–93, 2016.

[2] "Fire information in Canada," https://www.ciffc.ca/.

[3] A. Tyukavina, P. Potapov, M. C. Hansen, A. H. Pickens, S. V. Stehman, S. Turubanova, D. Parker, V. Zalles, A. Lima, I. Kommareddy *et al.*, "Global trends of forest loss due to fire from 2001 to 2019," *Frontiers in Remote Sensing*, vol. 3, 2022, Art. no. 825190.

[4] W. M. Jolly, M. A. Cochrane, P. H. Freeborn, Z. A. Holden, T. J. Brown, G. J. Williamson, and D. M. Bowman, "Climate-induced variations in global wildfire danger from 1979 to 2013," *Nature Communications*, vol. 6, no. 1, pp. 1–11, 2015.

[5] "Facts about wildland fires in Canada," https://www.nrcan.gc.ca/our-natural-resources/forests/wildland-fires-insects-disturbances/forest-fires/13143.

[6] B. M. Witte, R. F. Singler, and S. C. Bailey, "Development of an unmanned aerial vehicle for the measurement of turbulence in the atmospheric boundary layer," *Atmosphere*, vol. 8, no. 10, 2017, Art. no. 195.

[7] J. Reuder, M. O. Jonassen, and H. Ólafsson, “The small unmanned meteorological observer SUMO: Recent developments and applications of a micro-UAS for atmospheric boundary layer research,” *Acta Geophysica*, vol. 60, no. 5, pp. 1454–1473, 2012.

[8] S. Martin, J. Bange, and F. Beyrich, “Meteorological profiling of the lower troposphere using the research UAV “M^{2}AV Carolo”,” *Atmospheric Measurement Techniques*, vol. 4, no. 4, pp. 705–716, 2011.

[9] A. Rautenberg, M. S. Graf, N. Wildmann, A. Platis, and J. Bange, “Reviewing wind measurement approaches for fixed-wing unmanned aircraft,” *Atmosphere*, vol. 9, no. 11, 2018, Art. no. 422.

[10] M. Mondek and M. Hromčík, “On-line on-board wind estimation system for small UAVs,” in *20th International Conference on Process Control*, Strbske Pleso, Slovakia, Jun. 2015.

[11] F. C. Fuertes, L. Wilhelm, and F. Porté-Agel, “Multirotor UAV-based platform for the measurement of atmospheric turbulence: Validation and signature detection of tip vortices of wind turbine blades,” *Journal of Atmospheric and Oceanic Technology*, vol. 36, no. 6, pp. 941–955, 2019.

[12] S. Prudden, A. Fisher, M. Marino, A. Mohamed, S. Watkins, and G. Wild, “Measuring wind with small unmanned aircraft systems,” *Journal of Wind Engineering and Industrial Aerodynamics*, vol. 176, pp. 197–210, 2018.

[13] T. Niedzielski, C. Skjøth, M. Werner, W. Spallek, M. Witek, T. Sawiński, A. Drzeniecka-Osiadacz, M. Korzystka-Muskała, P. Muskała, P. Modzel *et al.*, “Are estimates of wind characteristics based on measurements with pitot tubes and gnss

receivers mounted on consumer-grade unmanned aerial vehicles applicable in meteorological studies?" *Environmental Monitoring and Assessment*, vol. 189, no. 9, 2017, Art. no. 431.

[14] J.-W. Kampoon, W. Okolo, S. A. Erturk, O. Daskiran, and A. Dogan, "Wind field estimation and its utilization in trajectory prediction," in *AIAA Atmospheric Flight Mechanics Conference*, Kissimmee, United States, Jan. 2015.

[15] J. D. Barton, "Fundamentals of small unmanned aircraft flight," *Johns Hopkins APL Technical Digest*, vol. 31, no. 2, pp. 132–149, 2012.

[16] B. Arain and F. Kendoul, "Real-time wind speed estimation and compensation for improved flight," *IEEE Transactions on Aerospace and Electronic Systems*, vol. 50, no. 2, pp. 1599–1606, 2014.

[17] R. J. Barthelmie, P. Crippa, H. Wang, C. M. Smith, R. Krishnamurthy, A. Choukulkar, R. Calhoun, D. Valyou, P. Marzocca, D. Matthiesen, G. Brown, and S. C. Pryor, "3D wind and turbulence characteristics of the atmospheric boundary layer," *Bulletin of the American Meteorological Society*, vol. 95, no. 5, pp. 743–756, 2014.

[18] D. Hollenbeck, G. Nunez, L. E. Christensen, and Y. Chen, "Wind measurement and estimation with small unmanned aerial systems (sUAS) using on-board mini ultrasonic anemometers," in *International Conference on Unmanned Aircraft Systems*, Dallas, United States, Jun. 2018.

[19] T. Shimura, M. Inoue, H. Tsujimoto, K. Sasaki, and M. Iguchi, "Estimation of wind vector profile using a hexarotor unmanned aerial vehicle and its application to meteorological observation up to 1000 m above surface," *Journal of Atmospheric and Oceanic Technology*, vol. 35, no. 8, pp. 1621–1631, 2018.

[20] G. W. Donnell, J. A. Feight, N. Lannan, and J. D. Jacob, "Wind characterization using onboard IMU of sUAS," in *Atmospheric Flight Mechanics Conference*, Atlanta, United States, Jun. 2018.

[21] R. T. Palomaki, N. T. Rose, M. van den Bossche, T. J. Sherman, and S. F. De Wekker, "Wind estimation in the lower atmosphere using multirotor aircraft," *Journal of Atmospheric and Oceanic Technology*, vol. 34, no. 5, pp. 1183–1191, 2017.

[22] C. A. Wolf, R. P. Hardis, S. D. Woodrum, R. S. Galan, H. S. Wichelt, M. C. Metzger, N. Bezzo, G. C. Lewin, and S. F. de Wekker, "Wind data collection techniques on a multi-rotor platform," in *Systems and Information Engineering Design Symposium*, Charlottesville, United States, Jun. 2017.

[23] J. González-Rocha, C. A. Woolsey, C. Sultan, and S. F. De Wekker, "Sensing wind from quadrotor motion," *Journal of Guidance, Control, and Dynamics*, vol. 42, no. 4, pp. 836–852, 2019.

[24] P. M. A. De Jong, J. J. v. d. Laan, A. C. i. Veld, M. M. Van Paassen, and M. Mulder, "Wind-profile estimation using airborne sensors," *Journal of Aircraft*, vol. 51, no. 6, pp. 1852–1863, 2014.

[25] G. Balmer, T. Muskardin, S. Wlach, and K. Kondak, "Enhancing model-free wind estimation for fixed-wing UAV," in *International Conference on Unmanned Aircraft Systems*, Dallas, USA, Jun. 2018.

[26] M. B. Rhudy, M. L. Fravolini, M. Porcacchia, and M. R. Napolitano, "Comparison of wind speed models within a pitot-free airspeed estimation algorithm using light aviation data," *Aerospace Science and Technology*, vol. 86, pp. 21–29, 2019.

[27] C. Grillo and F. Montano, "Wind component estimation for UAS flying in turbulent air," *Aerospace Science and Technology*, vol. 93, 2019, Art. no. 105317.

[28] M. B. Rhudy, Y. Gu, J. N. Gross, and H. Chao, “Onboard wind velocity estimation comparison for unmanned aircraft systems,” *IEEE Transactions on Aerospace and Electronic Systems*, vol. 53, no. 1, pp. 55–66, 2017.

[29] G. Perozzi, D. Efimov, J.-M. Biannic, and L. Planckaert, “Using a quadrotor as wind sensor: Time-varying parameter estimation algorithms,” *International Journal of Control*, vol. 95, no. 1, pp. 126–137, 2020.

[30] J. Velasco-Carrau, S. García-Nieto, J. Salcedo, and R. H. Bishop, “Multi-objective optimization for wind estimation and aircraft model identification,” *Journal of Guidance, Control, and Dynamics*, vol. 39, no. 2, pp. 372–389, 2016.

[31] M. Marino, A. Fisher, R. Clothier, S. Watkins, S. Prudden, and C. S. Leung, “An evaluation of multi-rotor unmanned aircraft as flying wind sensors,” *International Journal of Micro Air Vehicles*, vol. 7, no. 3, pp. 285–299, 2015.

[32] P. P. Neumann and M. Bartholmai, “Real-time wind estimation on a micro unmanned aerial vehicle using its inertial measurement unit,” *Sensors and Actuators A: Physical*, vol. 235, pp. 300–310, 2015.

[33] Y. Song, Q.-H. Meng, B. Luo, M. Zeng, S.-G. Ma, and P.-F. Qi, “A wind estimation method for quadrotors using inertial measurement units,” in *IEEE International Conference on Robotics and Biomimetics*, Qingdao, China, Dec. 2016.

[34] S. Allison, H. Bai, and B. Jayaraman, “Wind estimation using quadcopter motion: A machine learning approach,” *Aerospace Science and Technology*, vol. 98, 2020, Art. no. 105699.

[35] G. Perozzi, D. Efimov, J.-M. Biannic, and L. Planckaert, “Trajectory tracking for a quadrotor under wind perturbations: Sliding mode control with state-dependent gains,” *Journal of the Franklin Institute*, vol. 355, no. 12, pp. 4809–4838, 2018.

[36] K. Alexis, G. Nikolakopoulos, and A. Tzes, "Switching model predictive attitude control for a quadrotor helicopter subject to atmospheric disturbances," *Control Engineering Practice*, vol. 19, no. 10, pp. 1195–1207, 2011.

[37] Z. Zuo and S. Mallikarjunan, "$\mathcal{L}_1$ adaptive backstepping for robust trajectory tracking of UAVs," *IEEE Transactions on Industrial Electronics*, vol. 64, no. 4, pp. 2944–2954, 2016.

[38] O. A. Jasim and S. M. Veres, "A robust controller for multi rotor UAVs," *Aerospace Science and Technology*, vol. 105, 2020, Art. no. 106010.

[39] J. Xu, P. Shi, C.-C. Lim, C. Cai, and Y. Zou, "Reliable tracking control for underactuated quadrotors with wind disturbances," *IEEE Transactions on Systems, Man, and Cybernetics: Systems*, vol. 49, no. 10, pp. 2059–2070, 2018.

[40] B. Dai, Y. He, G. Zhang, F. Gu, L. Yang, and W. Xu, "Wind disturbance rejection for unmanned aerial vehicles using acceleration feedback enhanced H_∞ method," *Autonomous Robots*, vol. 44, no. 7, pp. 1271–1285, 2020.

[41] L. Guo and S. Cao, "Anti-disturbance control theory for systems with multiple disturbances: A survey," *ISA Transactions*, vol. 53, no. 4, pp. 846–849, 2014.

[42] W.-H. Chen, J. Yang, L. Guo, and S. Li, "Disturbance-observer-based control and related methods—an overview," *IEEE Transactions on Industrial Electronics*, vol. 63, no. 2, pp. 1083–1095, 2015.

[43] A. E. Rodríguez-Mata, I. González-Hernández, J. G. Rangel-Peraza, S. Salazar, and R. L. Leal, "Wind-gust compensation algorithm based on high-gain residual observer to control a quadrotor aircraft: Real-time verification task at fixed point," *International Journal of Control, Automation and Systems*, vol. 16, no. 2, pp. 856–866, 2018.

[44] K. Guo, J. Jia, X. Yu, L. Guo, and L. Xie, "Multiple observers based anti-disturbance control for a quadrotor UAV against payload and wind disturbances," *Control Engineering Practice*, vol. 102, 2020, Art. no. 104560.

[45] M. A. Lotufo, L. Colangelo, C. Perez-Montenegro, E. Canuto, and C. Novara, "UAV quadrotor attitude control: An ADRC-EMC combined approach," *Control Engineering Practice*, vol. 84, pp. 13–22, 2019.

[46] S. Wang, J. Chen, and X. He, "An adaptive composite disturbance rejection for attitude control of the agricultural quadrotor UAV," *ISA Transactions*, 2022, doi: 10.1016/j.isatra.2022.01.012.

[47] M. O'Connell, G. Shi, X. Shi, K. Azizzadenesheli, A. Anandkumar, Y. Yue, and S.-J. Chung, "Neural-fly enables rapid learning for agile flight in strong winds," *Science Robotics*, vol. 7, no. 66, 2022, Art. no. eabm6597.

[48] P. Tang, F. Zhang, J. Ye, and D. Lin, "An integral TSMC-based adaptive fault-tolerant control for quadrotor with external disturbances and parametric uncertainties," *Aerospace Science and Technology*, vol. 109, 2021, Art. no. 106415.

[49] L. Cui, R. Zhang, H. Yang, and Z. Zuo, "Adaptive super-twisting trajectory tracking control for an unmanned aerial vehicle under gust winds," *Aerospace Science and Technology*, vol. 115, 2021, Art. no. 106833.

[50] O. Mofid, S. Mobayen, and W.-K. Wong, "Adaptive terminal sliding mode control for attitude and position tracking control of quadrotor UAVs in the existence of external disturbance," *IEEE Access*, vol. 9, pp. 3428–3440, 2020.

[51] M. Zare, F. Pazooki, and S. Etemadi Haghighi, "Quadrotor UAV position and altitude tracking using an optimized fuzzy-sliding mode control," *IETE Journal of Research*, pp. 1–15, 2020.

[52] Z. Hou, P. Lu, and Z. Tu, "Nonsingular terminal sliding mode control for a quadrotor UAV with a total rotor failure," *Aerospace Science and Technology*, vol. 98, 2020, Art. no. 105716.

[53] H. Hassani, A. Mansouri, and A. Ahaitouf, "Robust autonomous flight for quadrotor UAV based on adaptive nonsingular fast terminal sliding mode control," *International Journal of Dynamics and Control*, vol. 9, no. 2, pp. 619–635, 2021.

[54] R. C. Rothermel, "A mathematical model for predicting fire spread in wildland fuels," U.S. Department of Agriculture, Intermountain Forest and Range Experiment Station, Ogden, UT, Research Paper INT-115, 1972.

[55] K. G. Hirsch, *Canadian forest fire behavior prediction (FBP) system: User's guide*, 1996, vol. 7.

[56] A. L. Sullivan, "Wildland surface fire spread modelling, 1990–2007. 1: Physical and quasi-physical models," *International Journal of Wildland Fire*, vol. 18, no. 4, pp. 349–368, 2009.

[57] ——, "Wildland surface fire spread modelling, 1990–2007. 2: Empirical and quasi-empirical models," *International Journal of Wildland Fire*, vol. 18, no. 4, pp. 369–386, 2009.

[58] ——, "Wildland surface fire spread modelling, 1990–2007. 3: Simulation and mathematical analogue models," *International Journal of Wildland Fire*, vol. 18, no. 4, pp. 387–403, 2009.

[59] T. Beer, "The interaction of wind and fire," *Boundary-Layer Meteorology*, vol. 54, no. 3, pp. 287–308, 1991.

[60] A. Kochanski, M. A. Jenkins, R. Sun, S. Krueger, S. Abedi, and J. Charney, "The importance of low-level environmental vertical wind shear to wildfire propagation:

Proof of concept," *Journal of Geophysical Research: Atmospheres*, vol. 118, no. 15, pp. 8238–8252, 2013.

[61] O. Rios, W. Jahn, and G. Rein, "Forecasting wind-driven wildfires using an inverse modelling approach," *Natural Hazards and Earth System Sciences*, vol. 14, no. 6, pp. 1491–1503, 2014.

[62] X. Li, H. Gao, M. Zhang, S. Zhang, Z. Gao, J. Liu, S. Sun, T. Hu, and L. Sun, "Prediction of forest fire spread rate using UAV images and an LSTM model considering the interaction between fire and wind," *Remote Sensing*, vol. 13, no. 21, 2021, Art. no. 4325.

[63] Y. K. Tan and S. K. Panda, "Self-autonomous wireless sensor nodes with wind energy harvesting for remote sensing of wind-driven wildfire spread," *IEEE Transactions on Instrumentation and Measurement*, vol. 60, no. 4, pp. 1367–1377, 2011.

[64] C. Yuan, Z. X. Liu, and Y. M. Zhang, "Aerial images-based forest fire detection for firefighting using optical remote sensing techniques and unmanned aerial vehicles," *Journal of Intelligent & Robotic Systems*, vol. 88, no. 2, pp. 635–654, 2017.

[65] Z. T. Jiao, Y. M. Zhang, J. Xin, L. X. Mu, Y. M. Yi, H. Liu, and D. Liu, "A deep learning based forest fire detection approach using UAV and YOLOv3," in *International Conference on Industrial Artificial Intelligence*, Shenyang, China, Jul. 2019.

[66] S. Sudhakar, V. Vijayakumar, C. S. Kumar, V. Priya, L. Ravi, and V. Subramaniyaswamy, "Unmanned aerial vehicle (UAV) based forest fire detection and monitoring for reducing false alarms in forest-fires," *Computer Communications*, vol. 149, pp. 1–16, 2020.

[67] M. Sarkar, X. Yan, B. A. Erol, I. Raptis, and A. Homaifar, "A novel search and survey technique for unmanned aerial systems in detecting and estimating the area for wildfires," *Robotics and Autonomous Systems*, vol. 145, 2021, Art. no. 103848.

[68] Z. Lin, H. H. Liu, and M. Wotton, "Kalman filter-based large-scale wildfire monitoring with a system of UAVs," *IEEE Transactions on Industrial Electronics*, vol. 66, no. 1, pp. 606–615, 2018.

[69] M. Vejmelka, A. K. Kochanski, and J. Mandel, "Data assimilation of dead fuel moisture observations from remote automated weather stations," *International Journal of Wildland Fire*, vol. 25, no. 5, pp. 558–568, 2016.

[70] T. Zhou, L. Ding, J. Ji, L. Li, and W. Huang, "Ensemble transform Kalman filter (ETKF) for large-scale wildland fire spread simulation using FARSITE tool and state estimation method," *Fire Safety Journal*, vol. 105, pp. 95–106, 2019.

[71] C. Zhang, M. Rochoux, W. Tang, M. Gollner, J.-B. Filippi, and A. Trouvé, "Evaluation of a data-driven wildland fire spread forecast model with spatially-distributed parameter estimation in simulations of the FireFlux I field-scale experiment," *Fire Safety Journal*, vol. 91, pp. 758–767, 2017.

[72] M. C. Rochoux, C. Emery, S. Ricci, B. Cuenot, and A. Trouvé, "Towards predictive data-driven simulations of wildfire spread–Part II: Ensemble Kalman filter for the state estimation of a front-tracking simulator of wildfire spread," *Natural Hazards and Earth System Sciences*, vol. 15, no. 8, pp. 1721–1739, 2015.

[73] Y. Long and X. Hu, "Spatial partition-based particle filtering for data assimilation in wildfire spread simulation," *ACM Transactions on Spatial Algorithms and Systems*, vol. 3, no. 2, pp. 1–33, 2017.

[74] F. Gu, "Localized recursive spatial-temporal state quantification method for data assimilation of wildfire spread simulation," *Simulation*, vol. 93, no. 4, pp. 343–360, 2017.

[75] L. Amezquita-Brooks, E. Liceaga-Castro, M. Gonzalez-Sanchez, O. Garcia-Salazar, and D. Martinez-Vazquez, "Towards a standard design model for quad-rotors: A review of current models, their accuracy and a novel simplified model," *Progress in Aerospace Sciences*, vol. 95, pp. 1–23, 2017.

[76] W. Khan and M. Nahon, "A propeller model for general forward flight conditions," *International Journal of Intelligent Unmanned Systems*, vol. 3, no. 2, pp. 72–92, 2015.

[77] P. L. Andrews, "The Rothermel surface fire spread model and associated developments: A comprehensive explanation," U.S. Department of Agriculture, Forest Service, Rocky Mountain Research Station, Fort Collins, CO, General Technical Report RMRS-GTR-371, 2018.

[78] M. A. Finney, "FARSITE: Fire area simulator-model development and evaluation," U.S. Department of Agriculture, Forest Service, Rocky Mountain Research Station, Ogden, UT, Research Paper RMRS-RP-4, Revised 2004, 1998.

[79] M. C. Rochoux, S. Ricci, D. Lucor, B. Cuenot, and A. Trouvé, "Towards predictive data-driven simulations of wildfire spread–part I: Reduced-cost ensemble Kalman filter based on a polynomial chaos surrogate model for parameter estimation," *Natural Hazards and Earth System Sciences*, vol. 14, no. 11, pp. 2951–2973, 2014.

[80] O. Rios, E. Pastor, M. M. Valero, and E. Planas, "Short-term fire front spread prediction using inverse modelling and airborne infrared images," *International Journal of Wildland Fire*, vol. 25, no. 10, pp. 1033–1047, 2016.

[81] P. L. Andrews, “Modeling wind adjustment factor and midflame wind speed for Rothermel’s surface fire spread model,” U.S. Department of Agriculture, Forest Service, Rocky Mountain Research Station, Fort Collins, CO, General Technical Report RMRS-GTR-266, 2012.

[82] G. D. Richards, “An elliptical growth model of forest fire fronts and its numerical solution,” *International Journal for Numerical Methods in Engineering*, vol. 30, no. 6, pp. 1163–1179, 1990.

[83] ——, “The properties of elliptical wildfire growth for time dependent fuel and meteorological conditions,” *Combustion Science and Technology*, vol. 95, no. 1-6, pp. 357–383, 1993.

[84] K. Yan, M. Chen, Q. Wu, and B. Jiang, “Extended state observer-based sliding mode fault-tolerant control for unmanned autonomous helicopter with wind gusts,” *IET Control Theory & Applications*, vol. 13, no. 10, pp. 1500–1513, 2019.

[85] S. He, S. Guo, Y. Liu, and W. Luo, “Passive gust alleviation of a flying-wing aircraft by analysis and wind-tunnel test of a scaled model in dynamic similarity,” *Aerospace Science and Technology*, vol. 113, 2021, Art. no. 106689.

[86] K. Eliker, S. Grouni, M. Tadjine, and W. Zhang, “Practical finite time adaptive robust flight control system for quad-copter UAVs,” *Aerospace Science and Technology*, vol. 98, 2020, Art. no. 105708.

[87] Y. M. Yi and Y. M. Zhang, “Fault diagnosis of an unmanned quadrotor helicopter based on particle filter,” in *International Conference on Unmanned Aircraft Systems*, Miami, FL, USA, Jun. 2017.

[88] M. H. Amoozgar, A. Chamseddine, and Y. M. Zhang, “Experimental test of a two-stage Kalman filter for actuator fault detection and diagnosis of an unmanned

quadrotor helicopter," *Journal of Intelligent & Robotic Systems*, vol. 70, no. 1, pp. 107–117, 2013.

[89] Y. J. Zhong, W. Zhang, Y. M. Zhang, J. Y. Zuo, and H. Zhan, "Sensor fault detection and diagnosis for an unmanned quadrotor helicopter," *Journal of Intelligent & Robotic Systems*, vol. 96, no. 3, pp. 555–572, 2019.

[90] W. Li, Z. Wang, Y. Yuan, and L. Guo, "Two-stage particle filtering for non-Gaussian state estimation with fading measurements," *Automatica*, vol. 115, 2020, Art. no. 108882.

[91] Y. Feng, X. Yu, and F. Han, "On nonsingular terminal sliding-mode control of nonlinear systems," *Automatica*, vol. 49, no. 6, pp. 1715–1722, 2013.

[92] L. Wu, P. Shi, and X. Su, *Sliding Mode Control of Uncertain Parameter-Switching Hybrid Systems*. John Wiley & Sons, 2014.

[93] J.-J. E. Slotine and W. Li, *Applied Nonlinear Control*. Englewood Cliffs: Prentice Hall, 1991.

[94] J. Wang, C. Wang, M. Xin, Z. Ding, and J. Shan, *Cooperative Control of Multi-Agent Systems: An Optimal and Robust Perspective*. Academic Press, 2020.

[95] X. Xiang, C. Liu, H. Su, and Q. Zhang, "On decentralized adaptive full-order sliding mode control of multiple UAVs," *ISA Transactions*, vol. 71, pp. 196–205, 2017.

[96] Z. Yu, Y. Zhang, B. Jiang, and X. Yu, "Fault-tolerant time-varying elliptical formation control of multiple fixed-wing UAVs for cooperative forest fire monitoring," *Journal of Intelligent & Robotic Systems*, vol. 101, no. 3, pp. 1–15, 2021.

[97] N. R. Lawrance and S. Sukkarieh, “Autonomous exploration of a wind field with a gliding aircraft,” *Journal of Guidance, Control, and Dynamics*, vol. 34, no. 3, pp. 719–733, 2011.

[98] S. Yang and S. Jeon, “Recursive path planning and wind field estimation for precision airdrop,” *Journal of Guidance, Control, and Dynamics*, vol. 42, no. 6, pp. 1429–1437, 2019.

[99] P. Zhang, I. Nevat, G. W. Peters, F. Septier, and M. A. Osborne, “Spatial field reconstruction and sensor selection in heterogeneous sensor networks with stochastic energy harvesting,” *IEEE Transactions on Signal Processing*, vol. 66, no. 9, pp. 2245–2257, 2018.

[100] D. Gu and H. Hu, “Spatial Gaussian process regression with mobile sensor networks,” *IEEE Transactions on Neural Networks and Learning Systems*, vol. 23, no. 8, pp. 1279–1290, 2012.